EXPERIMENTAL STUDIES OF TIME-RESOLVED LIGHT PROPAGATION IN TURBID MEDIA

By

Steen J. Madsen, B.Sc, M.Sc.

A Thesis

Submitted to the School of Graduate Studies

in Partial Fulfillment of the Requirements

for the Degree

Doctor of Philosophy

McMaster University

EXPERIMENTAL STUDIES OF LIGHT PROPAGATION IN TURBID MEDIA

DOCTOR OF PHILOSOPHY (1993)
(Physics)

McMASTER UNIVERSITY
Hamilton, Ontario

TITLE: Experimental Studies of Time-Resolved Light Propagation in Turbid Media

AUTHOR: Steen J. Madsen, B.Sc. (University of Toronto)
M.Sc. (McMaster University)

SUPERVISOR: Dr. Michael S. Patterson

NUMBER OF PAGES: xiv, 131

ABSTRACT

The purpose of the work presented here is to determine whether time-resolved remittance spectroscopy can be used to determine noninvasively the optical properties of turbid media such as biological tissue. Knowledge of these properties is important in both therapeutic and diagnostic applications of light in medicine. In all experiments, the propagation of light was modelled as a diffusive process.

The thesis consists of three interrelated sections. In the first section, the optical properties of tissue-simulating liquid phantoms were determined using established techniques based on steady-state diffusion theory and Monte Carlo simulations. In the second section, time-resolved experiments were performed in homogeneous liquid phantoms of varying geometries, and the ability of a simple time-dependent diffusion model to predict the remitted (transmitted or reflected) pulse shape and hence the optical properties of the phantoms was determined. In the final section, time-resolved studies were conducted in a homogeneous brain-simulating phantom containing discrete absorbing or scattering objects. Picosecond laser pulses were incident on the inhomogeneous phantom and the remitted pulses were compared to model pulses derived from a finite difference representation of the time-dependent diffusion equation.

ACKNOWLEDGEMENTS

This thesis represents four years of moderately hard labour during which I experieced incredible highs and abyssmal lows. Perhaps no one will ever read this work. It matters not, afterall, life is but a series of unconnected events in a cold, dark, lonely universe devoid of any meaning.

First and foremost, I would like to thank my supervisor, Dr. Michael Patterson, who pulled me out of the abyss on numerous occasions. His generosity, willingness to help, good natured ribbing and graceful base running will always be remembered. I also wish to express my gratitude to the peripatetic Dr. Brian Wilson. His insights and willingness to help were much appreciated. His uncanny ability to provide first rate research facilities allowed me to perform research at the "cutting edge". I would like to thank Dr. Young Park for teaching me the intricacies of picosecond laser spectroscopy and Drs. Satish Jaywant and Andreas Othonos for their experimental help. Thanks to John Blenkey, Alan Hazelhurst and Scott Phillips in the machine shop - I'm sure I made their life a living hell! Thanks also goes to David Moulton whose numerical calculations are legendary at the Hamilton Regional Cancer Centre; James Stang for showing me how to program (and how not to program), and Dr. Tom Farrell, Dr. Lothar Lilge, Joshua Woolsey and Rob Hemmerich for their computing assistance. I would like to thank Donna Laking and Ruth "shoeless" Alexander for their help, and Frank Sheridan and my friends

in Toronto (especially Peter Naperstkow) for many interesting adventures. Thanks to the gang at coffee break for conversations ranging from the sublime to the perverse.

I would like to thank Mars Canada Inc. for making M & M's the addictive candy that it is, and Air Canada and Knud Simonsen Industries for providing air and ground transportation. Finally, I would like to thank my parents for their support and for letting me choose my own path in life.

TABLE OF CONTENTS

EXPERIMENTAL STUDIES OF TIME-RESOLVED LIGHT PROPAGATION IN TURBID MEDIA

LIST OF ILLUSTRATIONS AND TABLES

CHAPTER 1

INTRODUCTION

1.1 Optical spectroscopy and imaging in turbid media.

The study of light propagation in tissue is important in many medical and biological applications of lasers and other light sources. Absorption and scattering of light determine its spatial distribution within the irradiated tissue and the subsequent biological effects in therapeutic uses such as laser surgery (Jacques and Prahl 1987) and photodynamic therapy (Wilson and Patterson 1986). In diagnostic applications, the light that is remitted, i.e., diffusely reflected from or transmitted through the tissue, can be measured to probe the metabolic, physiologic or perhaps the structural status of the tissue. Much of the interest in noninvasive in vivo tissue spectroscopy lies in quantifying the concentration and/or physiologic state of endogenous (e.g. hemoglobin, cytochrome aa_3, myoglobin, bilirubin and melanin) and exogenous (e.g. photodynamic sensitizers) chromophores. For example, oxygen metabolism and respiration can be studied by monitoring the oxygenation state of hemoglobin and cytochrome aa_3, respectively, while the uptake of photosensitizers in solid tumors can also be monitored spectroscopically.

The first studies of highly scattering biological materials by optical means were made by Millikan (1937) who developed techniques to detect absorbance changes of hemoglobin and myoglobin in cat muscle. He may have been the first to use near infrared

wavelengths to study biological materials. At around the same time, Keilin and Hartree (1939) observed that the cytochrome absorption bands from various microorganisms, which had been frozen in water or glycerol, were greatly enhanced by microcrystallization due to increased scattering.

The use of optical methods to study metabolism and oxidative processes became popular in the early 1950s when a time-sharing dual-wavelength system was developed for the quantitation of small changes in absorption in a highly scattering medium, such as cell suspensions or muscle tissues, in the visible and near infrared regions (Chance 1951). This work was extended by Butler and Norris (1960) who pioncered the use of near infrared spectroscopy in plants, animals and humans.

In the mid 1970s, Jobsis (1977) pioneered the use of near infrared transillumination spectroscopy. Since natural chromophores, such as hemoglobin in the red blood cell and cytochrome a, b and c in the cell mitochondrial membrane, absorb weakly in the near infrared, it became possible to monitor changes in cerebral oxygenation and metabolism in the intact head of a cat.

The cerebral oxygenation state has been measured in many animals (Piantadosi et al. 1986 and Hazeki et al. 1987) by measuring absorption changes at several wavelengths. By operating in reflection mode, such measurements have also been made on the human adult (Fox et al. 1985 and Ferrari et al. 1986a) and newborn infant (Brazy et al. 1985 and Ferrari et al. 1986b). Improvements in instrumentation have made it possible to measure absorption changes through approximately 8-9 cm of brain tissue (Cope and Delpy 1988). It is thus possible to transilluminate the head of most preterm infants.

The spectroscopic studies described above are somewhat limited in that they are only capable of measuring absorption *changes*. Absolute quantitation of chromophore concentrations requires knowledge of the optical pathlength in the tissue. Determination of the optical pathlength is complicated by the highly scattering nature of tissue, however, it can be obtained using time-resolved techniques in which the photon time-of-flight is measured. Since the time-of-flight is proportional to the propagation pathlength, it is possible to discriminate against longer pathlength, multiply-scattered photons. This is important in imaging applications where multiply-scattered photons result in images of reduced contrast and resolution. Time-resolved studies only became possible in the mid 1980s with the introduction of reliable picosecond light sources, such as mode-locked lasers or diode lasers, and fast photodetectors, such as microchannel plate photomultiplier tubes.

In time-resolved spectroscopy and imaging studies, the goal is to obtain the tissue optical properties from knowledge of the irradiation and detector geometries and measurements of the remitted light. Solutions of such problems usually require iterative solutions to the "forward" problem in which the optical properties are known and a model of light propagation is used to predict the detected signal (Wilson et al. 1992). In practice, a short (a few picoseconds) pulse is incident on the medium and the optical interaction coefficients are deduced from the temporal spreading of the remitted pulse following application of an appropriate model of light propagation.

The propagation of short pulses in random media has been of interest in many areas of applied science. For example, in atmospheric research the optical thickness of

clouds has been found from the time dependence of transmitted pulses (Weinman and Shipley 1972). Theoretical studies of light pulse propagation in multiple scattering media based on diffusion theory have been published by Ishimaru (1978a) and Furutsu (1980). Shimizu et al. (1979) measured the time-resolved reflectance of a plane wave from suspensions of microspheres and suggested that this technique could be used to determine the optical properties of random media such as tissue.

The first time-resolved studies in living tissue were performed by Chance et al. (1988a and 1988b) and Delpy et al. (1988). Chance and coworkers studied blood oxygenation and tissue metabolism in human brain and muscle, while Delpy's group measured the optical pathlength in the rat brain. In order to extract the optical properties from the remitted signal, a time-dependent diffusion model was developed by Patterson et al. (1989). Although the model is very simple (it assumes a semi-infinite homogeneous medium), the predicted pulse shapes were in good agreement with those obtained experimentally (Patterson et al. 1989).

The extension of time-resolved measurements to inhomogeneous media for imaging purposes has only been attempted very recently. With such measurements optical computed tomography (CT) imaging in biological tissue may be possible (Singer et al. 1990). The principle is relatively straightforward. Since time-resolved remittance spectra, detected at different locations around a particular organ, are affected differently by the presence of the internal structure, it should be possible to reconstruct the internal structure from these external measurements. However, since multiple scattering is the dominant interaction between light and tissue, there is no simple relationship (such as found in X-

ray CT) between the measured light signal and the optical interaction coefficients in a defined region of the tissue. As a result, reconstructive algorithms would likely be based on iterative applications of a forward model of light propagation. The irradiation conditions and an initial estimate of the spatial distribution of the optical properties would be the input to the algorithm. The forward model could then be used to predict the signals that would be observed under these conditions (Wilson 1992). It is important to note that the signals need not be restricted to amplitudes; other characteristics, such as the mean time-of-flight can be included in a time-dependent model (Arridge et al. 1991). To be clinically useful, such a model must be extremely fast, i.e., reconstructions should take no longer than a few minutes. The development of such fast accurate models requires knowledge of the interaction of light with biological tissue.

1.2 Interaction of light with biological tissue

The propagation of light (UV, visible and near-infrared) can, in principle, be described by multiple scattering electromagnetic theory (Ishimaru 1978b). In such a formalism, the tissue is considered a random medium whose permittivity, $\epsilon(\underline{r})$, fluctuates with position ($\underline{r}$) about some mean value ϵ_1, such that

$$\epsilon(\underline{r}) = \epsilon_1 + \epsilon_2(\underline{r}) \qquad (1)$$

where $\epsilon_2(\underline{r})$ is a random process whose variance and correlation length are known. Maxwell's equations can then be used to describe the statistical behaviour of the electric

field. Due to its complexity, the lack of available solutions (except in very restricted cases) and the lack of information about $\varepsilon_2(\underline{r})$, this formalism has yet to find application in tissue optics (Patterson et al. 1991a).

The usual approach is to consider the particulate nature of light and to describe the propagation of photons using radiative transfer theory. In this formalism the relevant optical properties are the absorption and elastic scattering coefficients and the differential scattering coefficient (phase function). Both scattering and absorption can be related directly to the tissue dielectric properties; specifically, the scattering can be associated with microscopic fluctuations in the refractive index. The average tissue refractive index, n, accounts for specular reflection at tissue boundaries and for the speed of light in tissue. At low fluence rates (power per unit area), these interaction coefficients for a given tissue depend only on the wavelength of the incident light. Clearly, in diagnostic applications such as spectroscopy and imaging, the fluence rate should be sufficiently low such that the tissue volume probed is not damaged. In all experiments described in this thesis, the fluence rate was low enough such that the tissue probed was undamaged and all absorption processes were assumed to be linear.

1.2.1 Wavelength dependence

The linear absorption coefficient, μ_a, is the probability per unit infinitesimal pathlength that a photon will be absorbed by the tissue. The optical absorption of tissue is the sum of absorptions due to specific chromophores (molecules absorbing light at

specific wavelengths), either occurring naturally (endogenous) or added to the tissue (exogenous). At low fluence rates, the local rate of energy absorption, $P(x,\lambda)$, is (Wilson 1991)

$$P(x,\lambda) = \sum_i \xi_i(\lambda)\ c_i(x)\ \phi(x,\lambda) = \mu_a(\lambda)\ \phi(x,\lambda) \qquad (2)$$

where c_i is the local concentration of the ith chromophore of extinction coefficient ξ_i (probability of photon absorption by the ith chromophore) and ϕ is the fluence rate.

Endogenous chromophores have distinctive absorption spectra and, as illustrated in Figure 1.1, different chromophores are dominant in different spectral regions. In the ultraviolet part of the spectrum μ_a is very large due to high UV absorption characteristic of biomolecules such as proteins and nucleic acids (e.g. tryptophan and urocanic acid). With increasing wavelength, this absorption falls off and absorption due to specific chromophores such as hemoglobin, myoglobin, bilirubin and melanin dominates. From Figure 1.1 it can be seen that the absorption spectrum of hemoglobin is very sensitive to its oxygenation state. Thus spectroscopic techniques can, in principle, be used to determine hemoglobin oxygenation. As the wavelength increases beyond 1000 nm, infrared absorption by water dominates and the absorption coefficient of most tissues is thus very water-like. As illustrated in Figure 1.1, differences in the absorption spectra of reduced and oxidized cytochrome aa_3 in the near infrared may be used to probe tissue oxygenation states spectroscopically. In the visible/near infrared, μ_a typically ranges from 0.01 to 0.5 mm^{-1} for soft tissues (Cheong et al. 1990).

The scatter coefficient, μ_s, is the probability per unit infinitesimal path length that

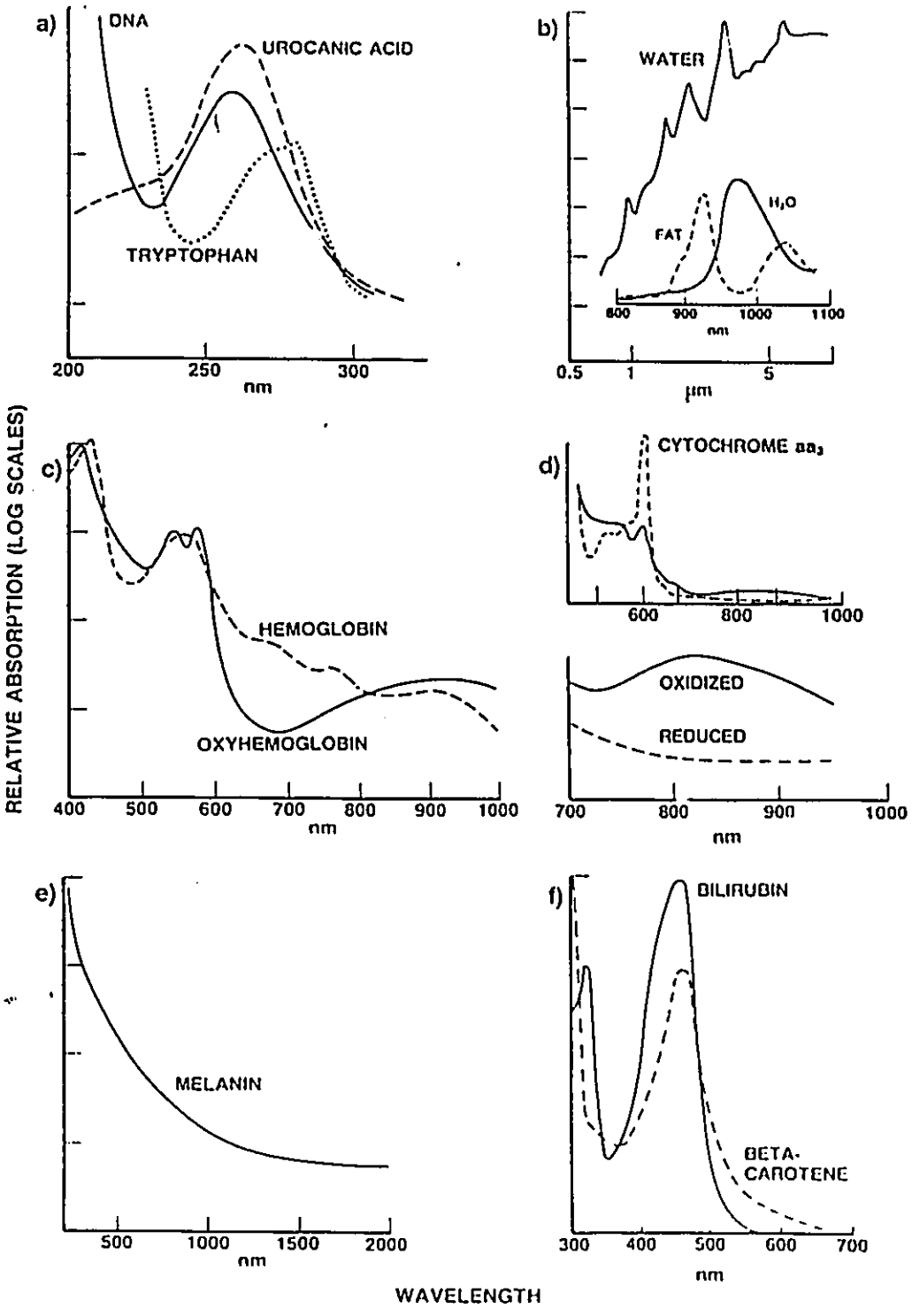

Figure 1.1 Absorption spectra of various tissue chromophores (Wilson 1991).

a photon will be scattered by the tissue. A complete description of scatter includes the angular dependence through the differential scattering cross section $d\mu_s(\underline{r},\hat{\Omega}' \rightarrow \hat{\Omega})$ which is the probability that a photon moving initially in a direction $\hat{\Omega}'$ is scattered to a new direction $\hat{\Omega}$ (Patterson et al. 1991). It is usually assumed that the differential scattering coefficient is independent of the incident photon direction, thus

$$d\mu_s(\hat{\Omega}' \rightarrow \hat{\Omega}) = d\mu_s(\hat{\Omega}' \cdot \hat{\Omega}). \tag{3}$$

The total scattering coefficient is then given by the integral over final solid angle

$$\mu_s = \int_{4\pi} d\mu_s(\hat{\Omega}' \rightarrow \hat{\Omega}) d\hat{\Omega}. \tag{4}$$

A normalized version of the differential scattering coefficient, the phase function, is commonly used in radiative transfer theory. This probability density function is given by

$$f(\hat{\Omega}' \cdot \hat{\Omega}) = \frac{1}{\mu_s} d\mu_s(\hat{\Omega}' \cdot \hat{\Omega}). \tag{5}$$

The mean cosine of the scattering angle, termed the anisotropy factor, is the average value of $(\hat{\Omega}' \cdot \hat{\Omega})$ and is denoted by g. For isotropic scattering g = 0; as the scattering becomes more forwardly peaked $g \rightarrow 1$. In cases where the light has undergone a large number of scattering events, it is common to combine the scattering coefficient and the anisotropy into a single transport scattering coefficient, $\mu_s' = \mu_s(1\text{-}g)$.

The spectral behaviour of the scattering coefficient is difficult to predict. Although light scattering by isolated dielectric particles has been studied extensively (Bohren and Huffman 1983 and van de Hulst 1981), it is unclear whether these results can be extended

to complex biological environments. As previously discussed, it is more appropriate to think of tissue as a medium with random dielectric fluctuations than as a distribution of scattering particles in a homogeneous medium. However, this second simpler model may provide some clues as to the effective size of the scattering inhomogeneities in tissue. Rayleigh scattering (Rayleigh 1871) dominates when the particles are much smaller than the wavelength of the incident light. In this regime the phase function is proportional to $(1+\cos^2\theta)$ and the scattering coefficient is proportional to λ^{-4}. Scattering by particles of size comparable to, or larger than the wavelength of incident light is commonly referred to as Mie scattering (Mie 1908). In this regime the wavelength dependence of the phase function is usually very complex with many minima and maxima. In general, both the scattering coefficient and the anisotropy factor will increase with particle size (Patterson et al. 1991b).

In the visible and near infrared, scattering in tissue appears to be Mie-like. The scattering coefficients of soft tissue typically range from 10 to 100 mm^{-1} while the scattering anisotropy ranges between 0.7 to 0.95 (Wilson 1991). The wavelength dependence of the scattering coefficient and the anisotropy for a sample of normal human glandular breast tissue is illustrated in Figure 1.2 (Peters et al. 1990). The results shown in Figure 1.2 are typical for tissue in that the scattering coefficient decreases slowly with wavelength while the scattering anisotropy remains relatively constant. The detailed wavelength dependence of the anisotropy is not straightforward and has not been throroughly investigated. If the phase functions can be attributed to independent spherical particles, then the effective size of the scattering particle in tissue is of the order of

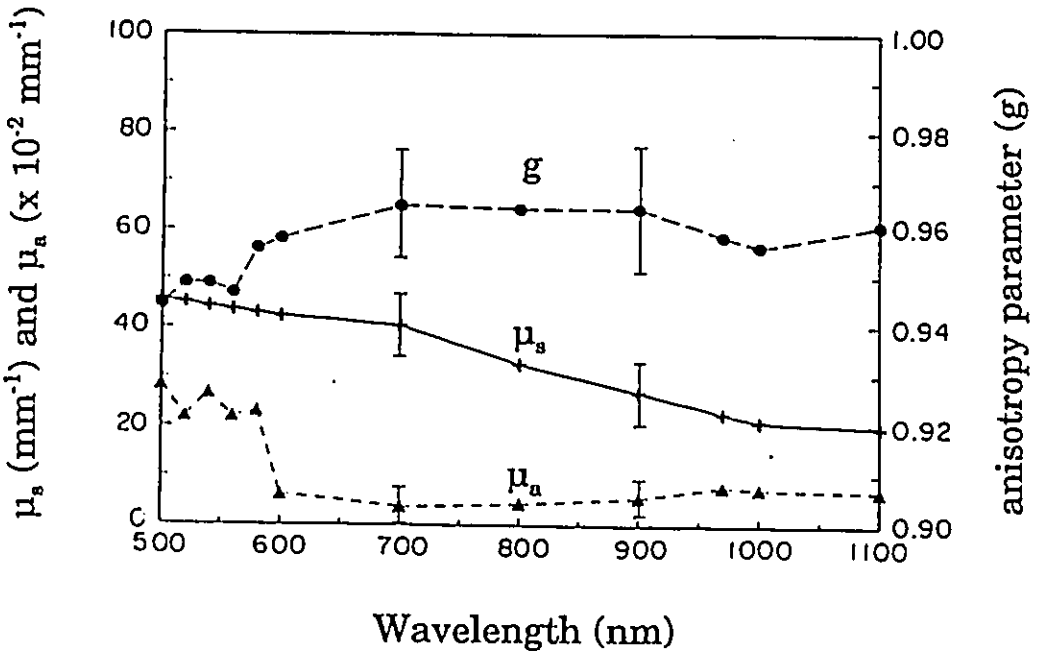

Figure 1.2 The absorption coefficient, scattering coefficient and anisotropy parameter for a sample of normal human glandular breast tissue (Peters et al. 1990).

microns, which suggests that the scattering is due to cells and major organelles. However, the validity of this interpretation is unclear since tissue is not a simple suspension of cells.

Since scattering can be attributed to microscopic fluctuations in the refractive index, a complete description of the light field must include knowledge of the average refractive index. The refractive index exerts its presence in two ways. Firstly, the speed of light in tissue is given by

$$c = \frac{c_o}{n} \tag{6}$$

where c_o is the speed in vacuo. For soft tissues in the 600 -1300 nm region, n ranges from 1.3 - 1.5 (Bolin et al. 1989), thus c ranges from 0.20 - 0.23 mm ps^{-1}. Secondly, the refractive index accounts for specular reflection (internal and external) at mismatched boundaries such as air - tissue interfaces. Quantitation of this reflectance can be obtained using Fresnel's equations if it is valid to assume a smooth plane boundary.

1.3 Determination of tissue optical properties

The optical properties of tissue can be divided into two classes: fundamental and derived. Fundamental optical properties include the absorption and scattering coefficients, the scattering phase function, the mean cosine of scatter, the transport scattering coefficient, the total attenuation coefficient, μ_t (sum of absorption and scattering coefficients) and its inverse, the mean free path (mfp), and the albedo, a (the ratio of the scattering coefficient to the total attenuation coefficent). The derived optical properties

can be considered as descriptors of different aspects of the spatial distribution of light in bulk tissue, and may be expressed in terms of the fundamental coefficients using various propagation models. They include the local and total diffuse reflectance and transmittance, the effective attenuation coefficient, μ_{eff} and its inverse, the effective penetration depth.

Experiments for measuring the fundamental optical properties fall into two categories: indirect and direct (Wilson et al. 1987). Indirect techniques are based on in vitro or in vivo measurements of derived parameters in bulk tissue. The fundamental coefficients can then be deduced by applying one or more light propagation models. Direct methods involve the use of tissue samples which are sufficiently thin such that multiple photon scattering is negligible. The fundamental optical properties can then be determined directly from measurements of the fractional light absorbance in the sample or of the light flux scattered by the sample. In terms of modelling, the only assumption made in this case is that light propagation can be described by radiative transfer theory.

1.3.1 Direct Methods

These methods require tissue samples which are thin enough such that single scattering dominates. In soft tissues at 630 nm, if $\mu_s = 40$ mm^{-1} (Figure 1.2), this implies that the sample should be less than 25 μm thick. Typically, the samples are mounted in a cuvette or supported between microscope slide covers. Different light irradiation and detection geometries are then used depending on the particular fundamental property to be measured. For example, measurement of the total attenuation coefficient can be

accomplished using a setup of the type illustrated in Figure 1.3(a). A well collimated beam (e.g. a laser beam) is incident on the tissue sample, and directly transmitted (i.e. unscattered) light is measured by a detection method which is insensitive to scattered radiation. For a sample of thickness x, if the incident and detected fluence rates (ψ_o and ψ respectively) are known, then the total attenuation coefficient is given by

$$\mu_t = \frac{1}{x}\ln\frac{\psi_o}{\psi} \tag{7}$$

Figure 1.3(b) illustrates the method used by Flock et al. (1987) to measure the scattering phase function. The sample is held between glass slides and immersed in a cylindrical water tank to minimize distortions in the measured phase function caused by refraction at the tissue boundaries. The detector is rotated around the sample and the signal is measured as a function of angle.

Measurement of the scattering coefficient using an integrating sphere technique is illustrated in Figure 1.3(c). The detector signal is measured with the sample present, (S_s), and without the sample, (S_o) (Wilson et al. 1987). For an optically thin sample of thickness x, the scattering coefficient is given by

$$\mu_s = \frac{1}{x}\frac{S_s}{S_o}. \tag{8}$$

The absorption coefficient can also be measured with an integrating sphere (Figure 1.3(d)). Measurements are made of the signal with the sample, (S_s), and without the sample, (S_o), but in this case S_s includes both the scattered and directly transmitted radiation. The difference between S_s and S_o is due only to absorption, thus the absorption

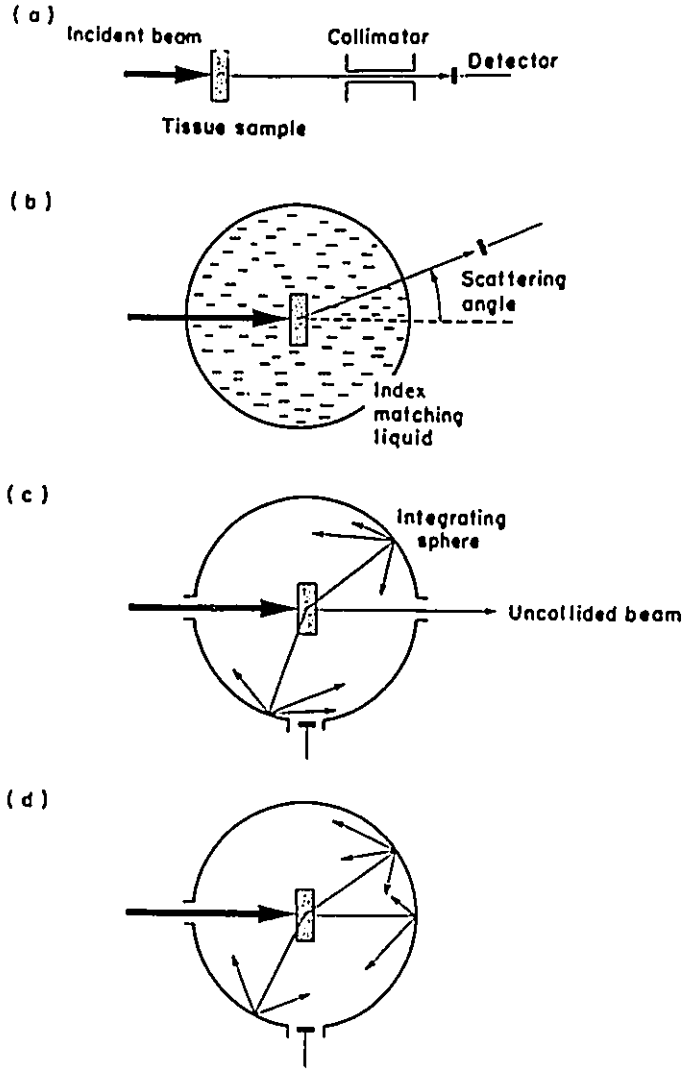

Figure 1.3 Methods for the direct measurement of fundamental optical properties in tissue. (a) Measurement of the total attenuation coefficient. (b) Measurement of the scattering phase function. (c) Measurement of the scattering coefficient. (d) Measurement of the absorption coefficient (Patterson et al. 1991b).

coefficient is given by (Patterson et al. 1991b)

$$\mu_a = \frac{1}{x}\frac{S_o - S_a}{S_o}. \qquad (9)$$

A comprehensive review of direct measurement techniques have been given by Wilson et al. (1987) and by Patterson et al. (1991b).

Although direct methods are model independent, they are problematic due to complications associated with obtaining sufficiently thin samples. Procedures such as freezing and mechanical grinding of tissue are commonly used to obtain thin samples, however, such procedures may result in measurement bias compared with the true values in intact tissues. It is unlikely that direct measurement techniques will be used clinically since they require tissue biopsy.

1.3.2 Indirect methods

Due to the problems associated with the direct methods, most investigators have pursued indirect methods to derive the optical properties of tissue. Sample preparation is relatively simple since optically thin samples are not required, and there is the possibility of performing noninvasive in vivo measurements.

Indirect measurements may be divided into three categories (Wilson et al. 1987): (i) external, in which detectors are located outside the tissue volume, (ii) internal, in which detector probes are located within the tissue, and (iii) pertubative methods, in which external or internal measurements are made after the addition to the tissue of some

substance with known optical properties. Clearly, in a clinical situation, external methods are preferred since they are noninvasive.

There are two main classes of external techniques: photothermal and radiometric. Photothermal methods involve the use of an external transducer to indirectly measure the effects of optical energy absorption within the tissue. Such techniques include pulsed photothermal radiometry (PPTR) (Long et al. 1987 and Prahl et al. 1992) and photoacoustic spectroscopy (PAS) (Cross et al. 1987). In PPTR an infrared detector is used to measure the blackbody infrared emission at the tissue surface following an incident light pulse. In PAS the mechanical deformation of the tissue or of an attached gas cell due to rapid thermal expansion caused by a light pulse is measured.

These techniques will probably be limited to dermatological studies where only superficial layers need to be probed (Wilson and Jacques 1990). The problem with both methods is that they rely on knowledge of the thermal and mechanical properties of the tissue, which are not always spatially and temporally uniform and constant.

Radiometric techniques, based on measurements of the diffuse reflectance and transmittance of light, are most sensitive and accurate in the scatter-dominated regime, i.e. in the red/near infrared spectral range. The advantages over photothermal techniques are severalfold. Firstly, the measurement is independent of the thermal or mechanical properties of the tissue. Secondly, the technique is capable of yielding the absorption, scattering (and possibly the refractive index) of the tissue. Thirdly, it may be used in a variety of clinical modes: surface, intracavitary, endoscopically and via catheters. Lastly, it may have depth profiling and localization capability (Wilson and Jacques 1990).

In general, six different types of measurement can be made (Figure 1.4): reflectance or transmittance, total or local fluence, and steady-state or time-resolved. Most studies to date have focussed on measurements of the diffuse reflectance. The measurable quantities are then R, R(t), R(ρ), and R(ρ,t) corresponding to total and local reflectance under steady-state (time-independent) and time-dependent conditions. The source-detector separation is denoted by ρ. Since both the diffuse reflectance and transmittance depend strongly on the tissue optical properties, their measurement may yield the fundamental optical properties if an appropriate model of light propagation is applied. Typically, such models have assumed optically homogeneous tissues, or very simple layered structures, and also simple tissue geometries.

Although indirect methods may be clinically appealing in that they offer the potential for noninvasive in vivo measurements, there are numerous complications. For example, the particular model used in deriving the microscopic properties can be quite complicated due to the fact that the irradiation and detection geometries must be accounted for in most cases. The validity of the model may also be suspect in some cases. Generally speaking, the simpler models are accurate only over a limited range of optical properties and geometries. The lack of analytic "inverse" solutions may also cause problems, i.e., the models usually predict the behaviour of the derived parameters given the fundamental properties, and only the simplest yield analytic expressions for the inverse task of calculating the fundamental properties from measurements of the derived parameters. It is thus necessary to iterate between the required fundamental properties and the derived data to obtain a best-fit solution.

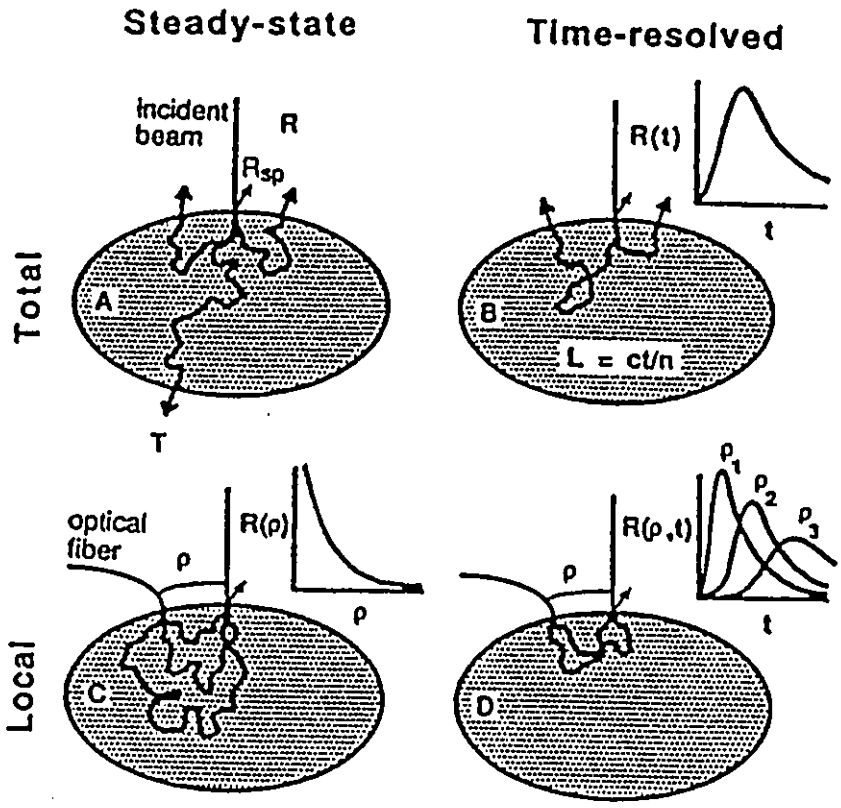

Figure 1.4 Methods for the indirect measurement of remittance. (A) Steady-state measurement of the total remittance as either reflectance R and/or transmittance T. (B) Time-resolved measurement of total remittance R(t) as a function of time. (C) Steady-state measurement of the local spatial distribution of remittance R(ρ) along the tissue surface. (D) Time-resolved measurement of the local spatial distribution of remittance R(ρ,t) along the tissue surface as a function of time (Wilson and Jacques 1990).

A potential problem with all indirect methods is that the derived data are usually restricted, i.e., it is unlikely that the fluence rate and/or reflectance will be measured at all points in or out of the irradiated tissue. Thus, it may not be possible to derive all the fundamental values from the measured data. Furthermore, van de Hulst (1980) has shown that the particular value of any derived parameter may result from different combinations of the fundamental properties. This has been termed the Similarity Principle and it may result in ambiguities in the calculated fundamental values (Wilson et al. 1987).

1.4 Light propagation models

Thus far, all models of light propagation used in tissue optics have been either numerical or approximate analytic solutions of the neutral particle transport equation, i.e., the wave properties of light are ignored and the propagation of light is described in terms of the transport of discrete photons which may be scattered conservatively (without energy loss) or absorbed. Numerical solutions to the transport equation include: (i) the doubling method to calculate diffuse reflectance and transmittance (van de Hulst 1980), (ii) the method of discrete ordinates (Duderstadt and Hamilton 1976) and, (iii) Monte Carlo computer simulations (Wilson and Adam 1983) in which individual photon "histories" are computer-simulated to calculate fundamental parameters or fluence distributions for any tissue and irradiation geometry.

Approximate analytic models include: (i) the 2-flux models (Kubelka 1948, Reichman 1973 and Mudgett and Richards 1972) which describe the diffuse reflectance

and transmittance for light incident on a tissue slab in terms of the fundamental absorption and scattering coefficients and, (ii) diffusion theory (Reynolds et al. 1976, Hemenger 1977, Takatani and Graham 1979, Doiron et al. 1983, Groenhuis et al. 1983, Svaasand and Ellingson 1983, Marijnissen and Star 1984, McKenzie 1985, Jacques and Prahl 1987 and Star et al. 1988) in which the distribution of fluence in scatter-dominated tissues can be expressed in terms of the fundamental optical properties. The diffusion equation may be solved analytically for simple geometries such as a slab illuminated by a collimated beam or a point or line source in an infinite medium. Numerical solution of the diffusion equation is required for more complex geometries or inhomogeneous media. It is important to note that the basic assumption in deriving the diffusion equation is that the angular flux is only linearly anisotropic. This will not be the case if absorption dominates scattering in the medium, or near boundaries or sources. The popularity of the diffusion equation among investigators in tissue optics can be attributed to its computational simplicity which makes it an ideal candidate for clinical applications. An additional attractive feature is the ease with which it can be extended to time-dependent problems.

1.5 Steady-state vs. time-resolved studies

1.5.1 Steady-state studies

In steady-state measurements, the number and angular distribution of photons emerging from the surface at any point constitute the observable quantities. Groenhuis et

al. (1983a and 1983b) were among the first to perform such measurements. They used diffusion theory to derive the Green's functions for photon current resulting from an isotropic point source at depth in a semi-infinite tissue as an infinite sum of modified Bessel functions. The radial reflectance for an arbitrary light source was then determined by integrating the Green's function over the tissue volume, treating each scatter site as an isotropic point source. Steinke et al. (1986) used this formulation to predict the changes in diffuse reflectance at a single radial position from blood in a cuvette as the hemoglobin oxygenation was changed. Schmitt et al. (1990) extended this approach and developed an expression for the radial reflectance from a multi-layered tissue such as skin.

Patterson et al. (1989) have presented a simple model in which the observed quantities were the relative reflectance at a number of distances from a "point" source and the total diffuse reflectance. Diffusion theory was then used to derive analytic expressions for the absorption and transport scattering coefficients in terms of those quantities. Several papers have been published (Bonner et al. 1987, Nossal et al. 1988, Weiss et al. 1989 and Nossal et al. 1989) in which a random walk model of photon migration was used to relate the fluence at the tissue surface to parameters such as the mean pathlength travelled by photons in the medium.

All of the methods discussed above involve either an absolute measurement of the reflectance vs. distance curve, or a relative measurment of the reflectance curve, which yields the effective attenuation coefficient, combined with some other absolute measurement, such as the total diffuse reflectance. These methods are problematic since

measurements of radial reflectance can be affected by small changes in any of the elements of the measurement. For example, changes in the output or spectral characteristics of the light source, changes in the optical fibers, filters, lens and in the sensitivity of the detector. Thin layers of dirt, blood or other fluids on the surface of the tissue under investigation can affect the absolute measurement of reflectance. (Farrell et al. 1992). A technique which depends only on the shape of the radial reflectance curve, i.e., a relative reflectance measurement is much more desirable.

Wilson et al. (1990) recently proposed such a technique. However, there were discrepancies between the measured reflectance and that predicted by their simple model at small source-detector separations. This was attributed to a lack of a rigorous boundary condition in their model.

Farrell et al. (1992) have recently extended the simple model to account for the correct boundary conditions. The model was in good agreement with both Monte Carlo simulations and experimental measurements performed in tissue-simulating phantoms. These preliminary results suggest that it may be possible to determine the optical properties directly from the shape of the radial reflectance curve, however, it must be emphasized that the model has only been tested under very limited conditions. Further studies must be performed to assess fully the validity of the model.

In summary, the limitations of steady-state measurements can be stated as follows: (i) both measurements and model are extremely sensitive to the boundary conditions at the tissue surface. (ii) it may be necessary to measure the absolute reflectance value at each point, (iii) measurements are required at multiple points over a full range of source-

detector separations and, (iv) effects of tissue heterogeneity and of finite tissue volume are not known and may lead to significant errors in the derived optical properties. Nevertheless, instrumentation is relatively straighforward and inexpensive, and measurements can be made in real-time thus allowing investigation of dynamic processes in tissue.

1.5.2 Time-resolved studies

Time-resolved measurements may be performed either directly in the time domain (Chance et al. 1988 and Wilson et al. 1989) or in the frequency domain (Lakowicz et al. 1989). In the former, the photon "time-of-flight", t, is directly related to the optical pathlength,

$$L = ct \tag{10}$$

where c is the speed of light in the material. Measurements of $R(\rho,\lambda,t)$ or $T(\rho,\lambda,t)$ then depend on the distribution of pathlengths. Models analogous to those of steady-state, based on time-dependent diffusion theory, have been developed (Patterson et al. 1989) in which $R(\rho,\lambda,t)$ can be expressed in closed analytic form as a function of ρ, t, $\mu_a(\lambda)$, $\mu_s'(\lambda)$ and n.

The basic principle of time-resolved reflectance measurements is illustrated in Figure 1.5. A picosecond pulse is incident on a semi-infinite, homogeneous, tissue-simulating medium. Multiple photon scattering results in a wide distribution of

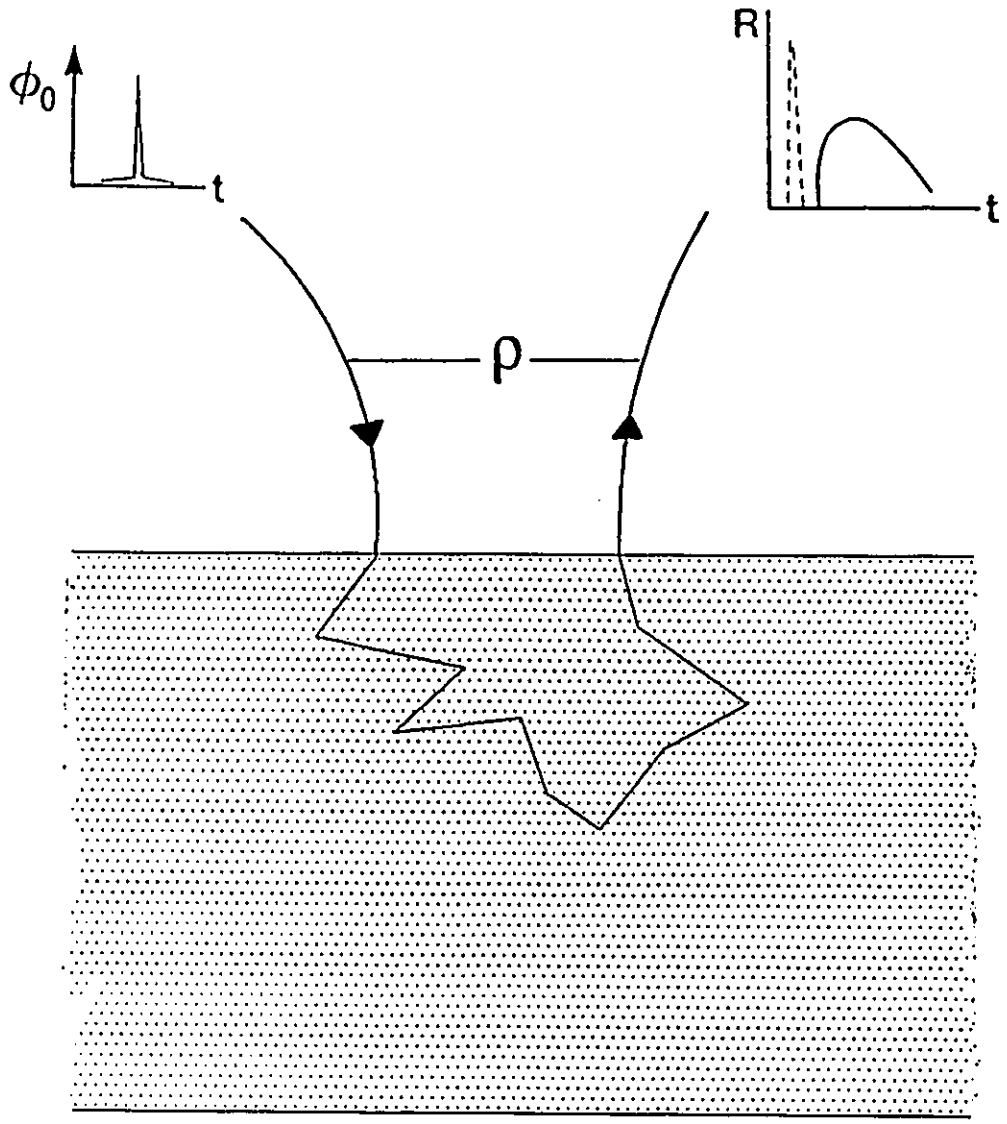

Figure 1.5 Principle of time-resolved reflectance measurements.

pathlengths and, hence a temporal broadening of the remitted pulse. The shape of this pulse depends on the source-detector separation and on the optical properties of the material probed. Typically, the remitted photons are collected over times ranging from tens of picoseconds to several nanoseconds. In the picosecond time regime, photons undergo only a few scattering events, thus the angular dependence of the scattering may strongly influence the observed remittance, and the absorption will be less important in tissues of high albedo. In this regime, the effective radius of the volume sampled is only a few mm. In the nanosecond time regime, the light becomes highly diffused, the absorption strongly influences the signal strength, and the details of the scattering interactions (the scattering anisotropy) will be less important. Thus, for long detection times, larger tissue volumes can be probed.

Some spatial localization of the signal is possible through relative placement of the light source and detectors. For example, a degree of depth discrimination in layered tissues can be achieved by scanning the detector along the tissue surface, since deeply penetrating photons have a higher probability of exiting the surface distant from the surface (Jacques 1989).

In the frequency domain, the intensity of the incident light is modulated at a high frequency (10^7-10^9 Hz) and the signal is measured by a phase-sensitive detector. The time delay due to the spread in photon propagation time causes a phase shift which, together with the amplitude modulation of the signal, depends on the pathlength distribution and, hence on $\mu_a(\lambda)$, $\mu_s'(\lambda)$, ρ and n. Measurements in the time and frequency domain are equivalent in principle - the differences being mainly technical in nature. The phase and

modulation are related to the time domain signal through simple Fourier transformations (Patterson et al. 1991c). In this thesis, discussion will be confined almost exclusively to the time domain.

The potential advantages of using time-dependent rather than steady-state techniques for nonivasive tissue spectroscopy are: (i) the measurements are relatively insensitive to tissue boundary conditions, which affect mainly the absolute signal values rather than distorting their time or frequency dependence, (ii) the time or frequency range can be adjusted such that it may be possible to perform absolute quantitative spectroscopy, even in limited tissue volumes, and (iii) spatially-resolved measurements are not required, thus contact probes may be based on a single detector fiber which can be very close to the source fiber to allow endoscopic or catheter probes.

In terms of imaging applications, time-dependent measurements offer several advantages over steady-state methods which rely on the measurement of intensity (W/m^2). Firstly, in transmission methods, scattered photons may be eliminated due to their longer time-of-flight through tissue. Secondly, in reflective methods, it may be possible to obtain information preferentially from one region of the tissue by imposing different time gates on the diffusely reflected photons. Thirdly, some property of the detected light (e.g. mean time-of-flight and/or time-to-peak) may be more sensitive to changes in tissue optical properties than is the intensity. Finally, the addition of time-resolved information may allow reconstructive imaging by constraining the set of possible solutions to the inverse problem (Wilson et al. 1992).

The cost of time-resolved systems depends on the tunability and time resolution

requirements. Inexpensive systems using diode lasers can easily be built, however, the lack of tunability and insufficient resolution may prohibit their use in many situations. Tunability and excellent time resolution may be obtained with mode-locked solid state pumped dye lasers, however, such systems are very expensive and, at present, must be confined to a major laboratory setting - the complexity of the light sources precludes routine use as clinical instruments. In such cases, steady-state measurements are significantly cheaper and simpler, and clinical instrumentation is fairly straightforward.

1.6 Thesis proposal

When a picosecond pulse is incident on a turbid medium such as tissue, the shape of the remitted pulse will be altered due to absorption and scattering of photons as they propagate through the medium. Through application of suitable models of light propagation, it may be possible to determine the optical properties of the medium from the shape of the remitted pulse. This is of clinical interest since such measurements may provide the basis for the noninvasive determination of tissue optical properties in vivo. The information derived from these measurements may be used spectroscopically to probe the metabolic and/or physiologic status of tissue, or it may be used in imaging applications to study the internal structure of organs.

This thesis is comprised of three distinct projects: (i) steady-state evaluation of the optical properties of a tissue-simulating phantom, (ii) time-resolved studies of the optical properties of tissue-simulating homogeneous phantoms of varying geometries, and (iii)

time-resolved studies of a tissue-simulating inhomogeneous phantom.

The purpose of the first project was to determine the optical properties (absorption and transport scattering coefficients) of phospholipid emulsions and ink solutions. Mixtures of phospholipid and ink are commonly used to construct tissue-simulating phantoms. Steady-state diffusion theory was used to determine the optical properties of phospholipid emulsions, while the optical properties of dilute ink solutions were determined by comparing the results of Monte Carlo computer simulations to measurements of the total attenuation coefficient and the diffuse reflectance and transmittance. The optical properties of the tissue-simulating phantoms, determined from established steady-state techniques, became the "gold standards" against which the time-resolved optical properties were compared. The study of the optical properties of dilute ink solutions (Section 2.2) was originally published in *Phys. Med. Biol.*, 37, 985-995, 1992, under the title: "The use of India ink as an optical absorber in tissue-simulating phantoms". Several changes have been made to the original paper. They include the addition of Figures 2.2 - 2.5 and 2.7, and detailed descriptions of the Monte Carlo code and the experimental procedure. The experiments were performed solely by the author. The Monte Carlo code, originally developed by Dr. Doug Wyman, was modified by the author to suit the particular experimental geometry.

In the second project, described in Chapter 3, the ability of a simple time-dependent diffusion model (Patterson et al. 1989) to derive the absorption and transport scattering coefficients from the shape of a remitted pulse in homogeneous media of different geometries was tested. This was accomplished by fitting the analytic expressions

of diffusion theory to the experimental pulse shape. The validity of the derived optical properties was ascertained through comparison with the steady-state values obtained in the first project. Initially, the validity of the model was examined in the geometry for which it was derived (a semi-infinite medium) over a range of transport-scattering and absorption coefficients. The model was also tested under more biologically realistic conditions using spherical and cylindrical phantoms. By varying the size of the different geometries and the source-detector separation, the effects of the boundaries on the optical properties estimated with the simple model was also studied. Chapter 3 was originally published in *Appl. Opt.*, 31, 3509-3517, 1992, under the title: "Experimental tests of a simple diffusion model for the estimation of scattering and absorption coefficients of turbid media from time-resolved diffuse reflectance measurements". Changes to the original paper include the following. Figures 3.5, 3.9, 3.10 and 3.11 have been corrected for the scattering of ink based on the results discussed in Section 2.2. Figures 3.4, 3.7 and 3.8 did not appear in the original publication. The time-resolved experiments described in Chapter 3 were performed at the Harrison Spectroscopy Laboratory, Massachusetts Institute of Technology with the assistance of Dr. Young Park. The Monte Carlo codes were written by Dr. Tom Farrell and modified by Rob Hemmerich and the author.

In the third project, time-resolved studies were conducted in a homogeneous tissue-simulating phantom containing discrete absorbing or scattering objects of varying size and optical properties. Picosecond pulses were launched into the phantom and the effects of the object on the remitted pulse shape were analyzed. A simple finite difference model was developed to describe the photon propagation in the inhomogeneous medium.

The validity of the model was ascertained by comparing the shape of the experimental pulses to that predicted by the model.

CHAPTER 2

STEADY-STATE MEASUREMENTS

2.1 The optical properties of Intralipid

2.1.1 Introduction

Intralipid (Kabivitrum, Inc., Ca.) is an emulsion of phospholipid micelles and water that is used clinically as an intravenously administered nutrient. Since Intralipid is turbid and has no strong absorption bands in the visible part of the electromagnetic spectrum, it is commonly used as a tissue-simulating phantom in light dosimetry experiments (Flock et al. 1987, Driver et al. 1989, Wilson et al. 1989, van Staveren et al. 1991, Flock et al. 1992 and Madsen et al. 1992). The name Intralipid comes from the fact that the scattering particles consist of soybean oil encapsulated within a monolayer membrane of lecithin with a thickness of approximately 2.5-5.0 nm (van Staveren et al. 1991). Studies using transmission electron microscopy show that the particles are approximately spherical with a mean diameter of 97 nm (van Staveren et al. 1991). The scattering of light in the suspension can thus be described by Mie theory. It is unclear what causes the slight absorption of light by Intralipid. Flock et al. (1992) conclude it is primarily due to soybean oil, whereas Driver et al. (1989) attribute the absorption to water.

The purpose of this study was to determine the optical properties of Intralipid and a similar phospholipid emulsion known as Liposyn (Abbott Laboratories, Montreal, Canada) at 584 nm using the added absorber method (Profio and Sarnaik 1984 and

Wilson et al. 1986). This wavelength was chosen to match that at which the time-resolved experiments were performed.

2.1.2 Theory

For a large diameter light beam incident normally on the surface of an optically homogeneous semi-infinite medium, the fluence rate, ϕ, decays exponentially with depth, z, except close to the surface and, invoking diffusion theory, may be expressed as (Wilson et al. 1986)

$$\phi(z) = \phi_0 k e^{-\mu_{eff} z} \tag{11}$$

where ϕ_0 is the irradiance (W/cm^2), k is a scalar that depends on the amount of backscattered light and μ_{eff} is the effective attenuation coefficient. For infinite beam diameter,

$$\mu_{eff}^2 = 3\mu_a(\mu_a + \mu_s') \tag{12}$$

and

$$\mu_a = \mu_{a\,IL} + \mu_{a\,ink} \tag{13}$$

where $\mu_{a\,IL}$ is the inherent absorption coefficient of Intralipid and $\mu_{a\,ink}$ is the absorption coefficient of the added absorber (India ink in this case). It should be noted that, in all cases considered, $\mu_{s\,ink} << \mu_{s\,IL}$.

For a given μ_a, a plot of $\ln(\phi(z)/\phi_0)$ versus z yields a straight line with slope $-\mu_{eff}$.

This procedure is repeated several times after the addition of known amounts of added absorber. From equation (12), if $\mu_s' >> \mu_a$ then a plot of μ_{eff}^2 versus μ_a will yield a straight line of slope $3\mu_s'$ and intercept $3\mu_a\mu_s'$. From such measurements, it is possible to determine the absorption and transport scattering coefficients of Intralipid.

2.1.3 Materials and methods

The experimental setup is illustrated in Figure 2.1. The output from an arc lamp was focussed into a monochromator and the resultant 584 nm output beam was coupled into an optical fiber. The fiber was placed a sufficient distance from the bottom of a 30 x 30 x 75 cm glass tank such that the beam could be considered infinite, i.e., the beam diameter (~ 20 cm) was much greater than μ_{eff}^{-1}. The glass tank was filled with varying concentrations of Liposyn diluted with deionized water. Light collection was accomplished with the use of an isotropic fiber, i.e., an optical fiber with a spherical diffusing tip (2 mm dia.). This fiber was connected to a monochromator (incidental to these experiments) and the output was incident on a photomultiplier tube (PMT). The PMT signal was fed to an amplifier, discriminator and scaler for single photon counting.

Measurements of the fluence rate as a function of detector depth were first made in a 1 % (by solids) Liposyn solution containing no added absorber. The detector depth was increased in increments of 2 mm until the signal-to-noise ratio fell below 3:1. A known amount of absorber (India ink) was then added and the process repeated. Plots of $\ln(\phi(z)/\phi_0)$ versus z were constructed for added absorption coefficients ranging from 0

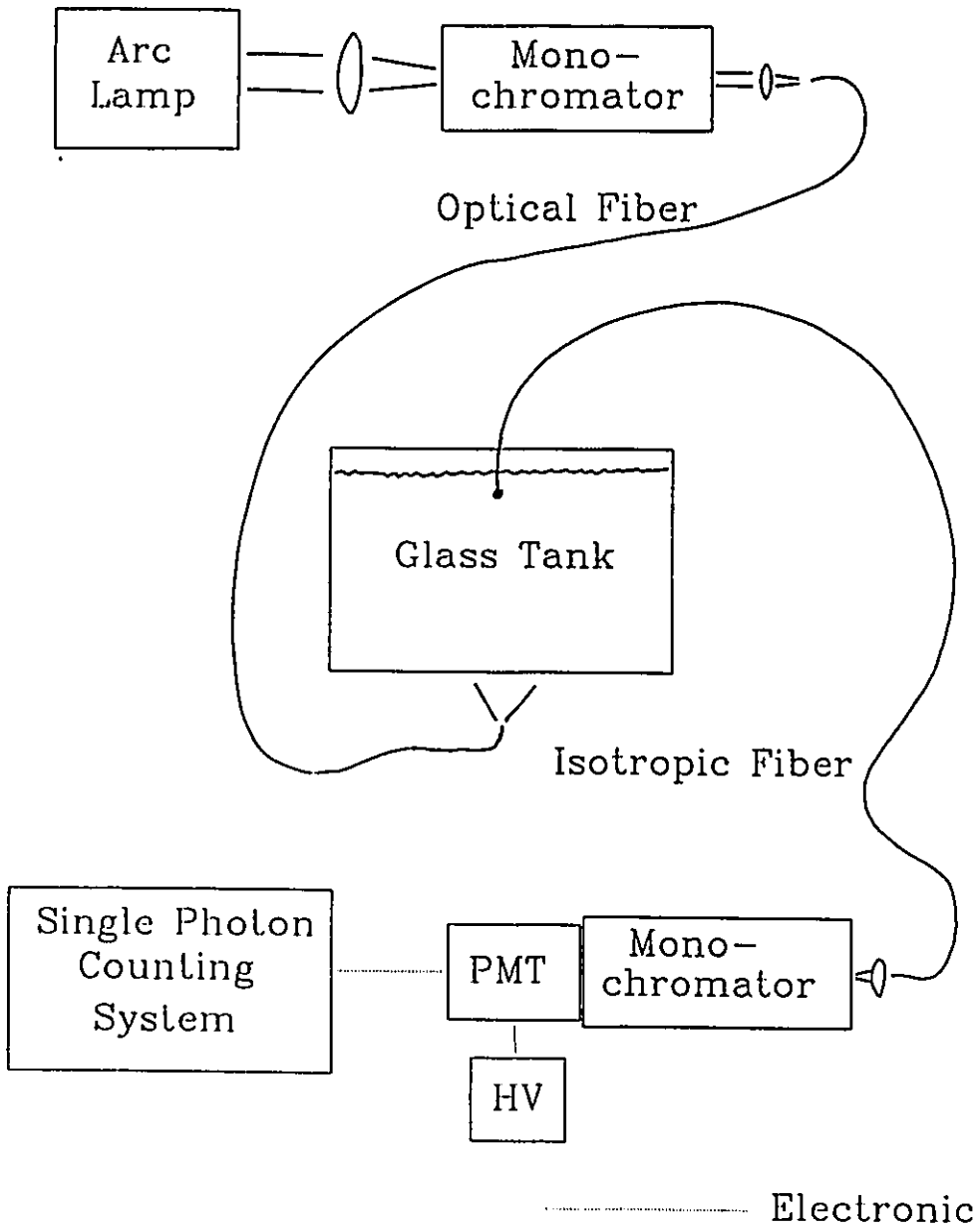

Figure 2.1 Experimental setup for measuring the optical properties of Liposyn. HV denotes the high voltage supply.

to 0.001 mm^{-1}. The procedure described above was repeated in Liposyn solutions of 2.2, 3.5 and 4.5 % solids. Measurements were also made in a 1 % solution of Intralipid in order to determine whether there were any differences in the optical properties of the two emulsions.

2.1.4 Results and Discussion

Typical plots of $\ln(\phi(z)/\phi_o)$ vs. depth and μ_{eff}^2 vs. added absorber are shown in Figures 2.2 and 2.3 respectively. The optical properties of Liposyn (μ_a and μ_s') as a function of concentration are summarized in Figures 2.4a and 2.4b. In both cases, the optical interaction coefficients are linear with concentration over the range studied. In the case of the absorption coefficient, extrapolation to 0 % concentration yields a value of $(2.75 \pm 0.47) \times 10^{-4}$ mm^{-1} which is somewhat higher than the absorption coefficient of pure water at 585 nm (1.68×10^{-4} mm^{-1} (Hale and Querry 1973)). At a concentration of 1 %, the absorption coefficient obtained here ($(4.13 \pm 0.50) \times 10^{-4}$ mm^{-1}) is in excellent agreement with that obtained by Flock et al. (1992) at 590 nm ($(4.25 \pm 0.25) \times 10^{-4}$ mm^{-1}). The transport scattering coefficient obtained at a concentration of 1 % Liposyn ((1.59 ± 0.17) mm^{-1}) is in good agreement with the experimental results of Pogue (1992) at 590 nm ((1.39 ± 0.14) mm^{-1}), Woolsey (1992) at 584 nm ((1.50 ± 0.15) mm^{-1}) and the theoretical Mie calculations of van Staveren et al. (1991) at 584 nm ((1.39 ± 0.01) mm^{-1}).

The optical properties of Intralipid agreed to within 5 % of those obtained for liposyn. This is comparable to the variation observed in different batches of the same

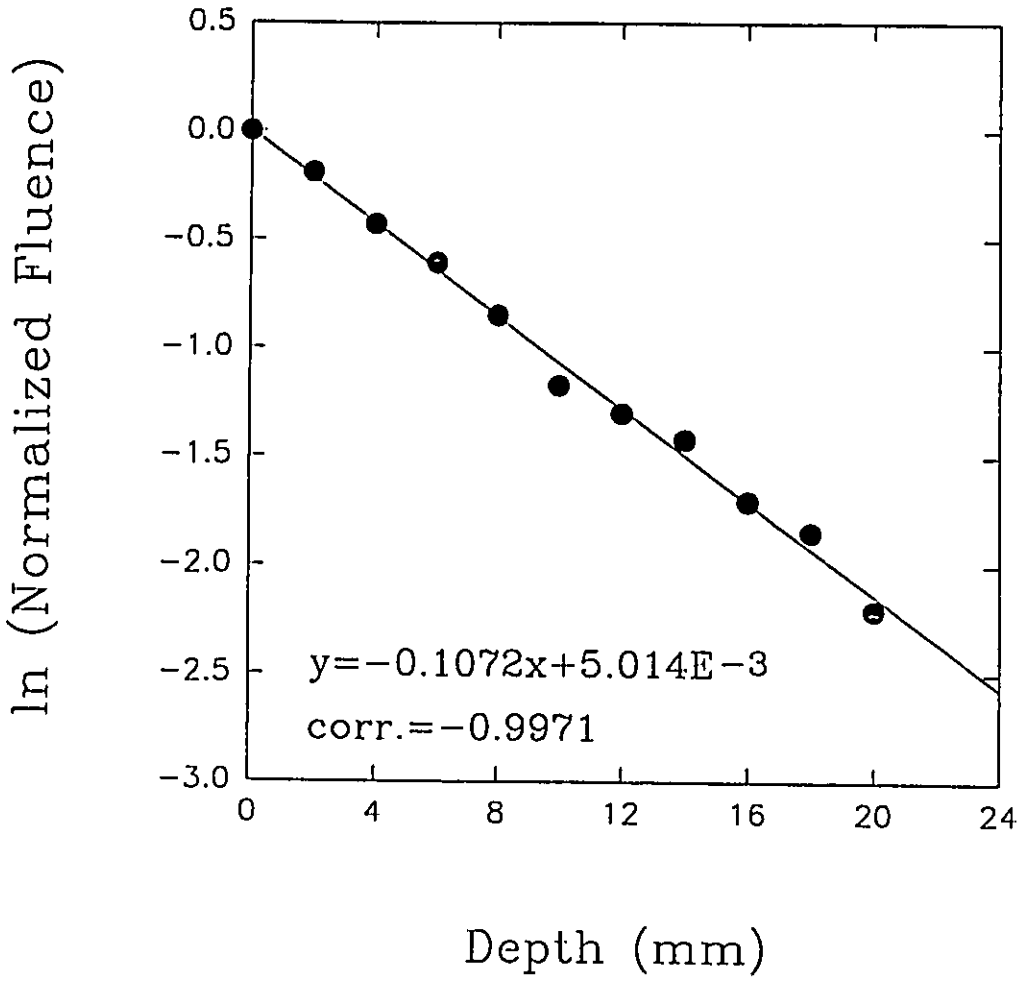

Figure 2.2 Log_e (normalized fluence) versus depth. Measurements were made in a 2.2 % Liposyn solution containing India ink ($\mu_a = 0.0006\ mm^{-1}$). The solid line represents a linear fit to the experimental data.

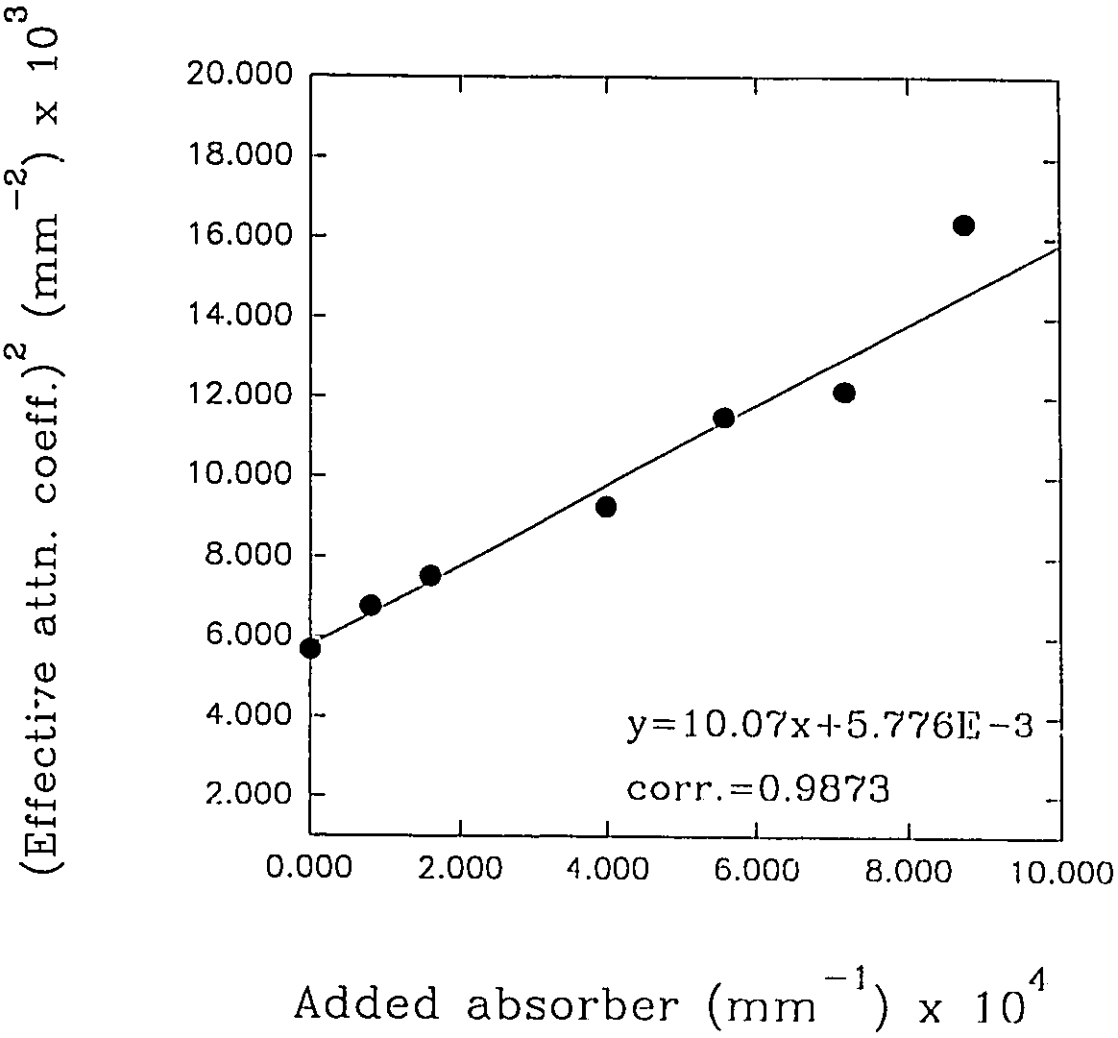

Figure 2.3 (Effective attenuation coefficient)^2 versus added absorber in a 2.2 % Liposyn solution. The solid line represents a linear fit to the experimental data.

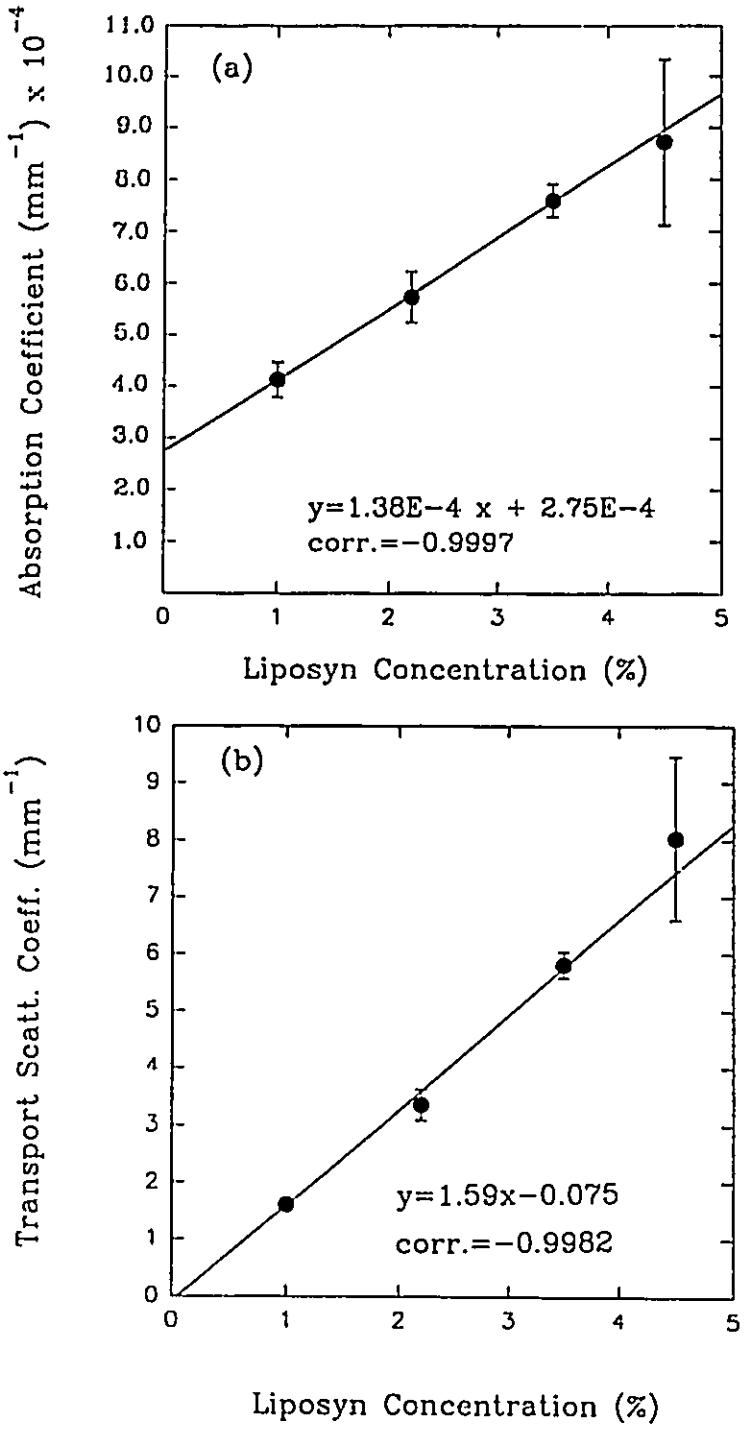

Figure 2.4 Optical properties of Liposyn as a function of concentration. (a) Absorption coefficient. (b) Transport scattering coefficient. The solid lines represent linear fits to the experimental data.

brand.

2.1.5 Conclusions

An added absorber method was used to determine the absorption and transport scattering coefficients of Liposyn. The results were found to be in good agreement with the theoretical and experimental results of others. Differences in the optical properties of Intralipid and Liposyn were of the same order as batch variations of the same brand. Thus Intralipid and Liposyn can be used interchangeably.

2.2 The optical properties of India ink

2.2.1 Introduction

India ink is a particulate absorber consisting of carbon particles (dia. ≈ 0.1 - 1.0 μm) suspended in water. Since it is strongly absorbing across the visible portion of the electromagnetic spectrum, and is readily available and inexpensive, it is frequently used as an optical absorber in tissue-simulating phantoms for light dosimetry (Driver et al. 1989, Wilson et al. 1989 and Flock et al. 1992). Unfortunately, the optical properties of particulate absorbers, such as India ink, have not been thoroughly investigated. A common and important assumption has been that ink acts as a perfect black body absorber. The validity of this assumption will be examined here.

In this chapter, the optical properties of India ink at a representative visible

wavelength are reported. It is assumed here that the scattering phase function can be described by the Henyey-Greenstein function (Henyey and Greenstein 1941) given by

$$f(\hat{\Omega}'\cdot\hat{\Omega}) = \frac{0.5(1-g^2)}{(1+g^2-2g(\hat{\Omega}'\cdot\hat{\Omega}))^{\frac{3}{2}}} . \qquad (14)$$

This function has often been used to represent anisotropic light scattering (van de Hulst 1981) such as that in tissue. It contains one free parameter, g, the mean cosine of the scattering angle, which changes the shape of the function.

The optical properties were measured as follows (Peters et al. 1990). The total attenuation coefficient, μ_t, was measured for dilute ink solutions. The diffuse reflectance (R_m) and transmittance (T_m) were measured using integrating spheres. Monte Carlo simulations of the integrating sphere measurements were then used to estimate a and g. μ_s and μ_a were then calculated from a and μ_t.

In addition, the size distribution of the ink particles was determined by electron microscopy. The albedo was calculated from Mie theory (Penndorf 1962, van de Hulst 1981) using the simplifying assumption that the ink comprised only two components: small (0.1 μm dia.) and large (1.0 μm dia.) particles. This value was then compared to the experimental albedo.

2.2.3 Theory

The albedo of an absorbing sphere can be derived from Mie theory (van de Hulst

1981) if its size and complex refractive index, m=n(1-iκ) are known. The imaginary part of the refractive index, nκ, is the damping factor, while κ is called the index of attenuation. If the sphere is in a transparent medium of refractive index $n_o \neq 1$, m is the actual refractive index divided by n_o, and the wavelength in the medium λ_o, not in air, should be used in computing the size factor $x=2\pi r/\lambda_o$, where r is the radius of the sphere.

The single particle cross sections for extinction, scattering and absorption are denoted by σ_t, σ_s and σ_a respectively, where conservation of energy requires that $\sigma_t=\sigma_a+\sigma_s$. The efficiency factors for extinction, scattering and absorption are given by $Q_i=\sigma_i/G$, where G is the geometrical cross section (πr^2).

(i) Small spheres ($x \leq 0.8$).

For small absorbing spheres, Q_t can be expressed as a power series in x from which Q_s and Q_a can be evaluated (Penndorf 1962).

$$Q_t=\frac{24n^2\kappa}{Z_1}x + \left\{\frac{4n^2\kappa}{15} + \frac{20n^2\kappa}{3Z_2}\right\}x^3 + 4.8n^2\kappa\left\{\frac{7(n^2+n^2\kappa^2)^2 + 4(n^2-n^2\kappa^2-5)}{Z_1^2}\right\}x^3 + \frac{8}{3}\left\{\frac{[(n^2+n^2\kappa^2)^2 + (n^2-n^2\kappa^2-2)]^2 - 36n^4\kappa^2}{Z_1^2}\right\}x^4 \quad (15)$$

where

$$Z_1 = (n^2+n^2\kappa^2)^2 + 4(n^2-n^2\kappa^2) + 4 \quad (16)$$

and

$$Z_2 = 4(n^2+n^2\kappa^2)^2 + 12(n^2-n^2\kappa^2) + 9. \quad (17)$$

The efficiency factor for scattering is given by

$$Q_s = \frac{8}{3Z_1^2}\{[(n^2+n^2\kappa^2)^2 + n^2-n^2\kappa^2-2]^2 + 36n^4\kappa^2\}x^4 \cdot \left\{1 + \left(\frac{6}{5Z_1}\right)[(n^2+n^2\kappa^2)^2-4]x^2 - \left(24n^2\kappa\frac{x^3}{3z_1}\right)\right\} \quad (18)$$

and $Q_a = Q_t - Q_s$. The above are valid in the range n = 1.25 - 1.75 and $n\kappa \leq 1$.

(ii) Large spheres (x >> 1).

Anomalous diffraction theory can be used to evaluate the efficiency factors of an absorbing sphere if $|n-1| << 1$, $n\kappa << 1$ and $x >> 1$ (van de Hulst 1981). Then Q_t is given (van de Hulst 1981) by

$$Q_t=2-4e^{-w}\frac{\cos\beta}{\rho}\sin(\rho-\beta)-4e^{-w}\left(\frac{\cos\beta}{\rho}\right)^2\cos(\rho-2\beta)+4\left(\frac{\cos\beta}{\rho}\right)^2\cos2\beta\ , \quad (19)$$

where $w=\rho\tan\beta$, $\rho=2x(n-1)$ and $\tan\beta=n\kappa/(n-1)$. The efficiency factor for absorption is (van de Hulst 1981)

$$Q_a = 1 + \frac{e^{-2w}}{w} + \frac{e^{-2w}-1}{2w^2} \quad (20)$$

and $Q_s = Q_t - Q_a$.

(iii) Suspensions of spheres.

In a suspension containing a range of sphere sizes, the total linear scattering and

absorption coefficients are given by

$$\mu_s = \sum_i N_i \, \sigma_{si} \tag{21}$$

and

$$\mu_a = \sum_i N_i \, \sigma_{ai} \tag{22}$$

where N_i is the volume concentration of spheres of radius r_i.

2.2.4 Monte Carlo model

The Monte Carlo model described here is very similar to that used by Peters et al. (1990). The geometry of the Monte Carlo simulation of the reflectance and transmittance measurements is illustrated in Figure 2.5. A parallel beam of light (diameter d) of uniform intensity was incident normally on the sample, held between 1.0 mm thick glass slides. The calculated transmittance (T_c) was the fraction of the incident light emerging through the exit face within the detection aperture of diameter D, including both unattenuated and scattered photons. The calculated reflectance (R_c) was the fraction of the incident light which was backscattered through the aperture on the entrance face of the sample holder. R_c did not include the photons specularly reflected at the first air-glass interface: estimated to be 4 % based on a refractive index of 1.515 for crown glass (Corning Glass Works 1991). R_c also did not include photons which reflected off the exit face and emerged through the entrance face without interacting with the sample.

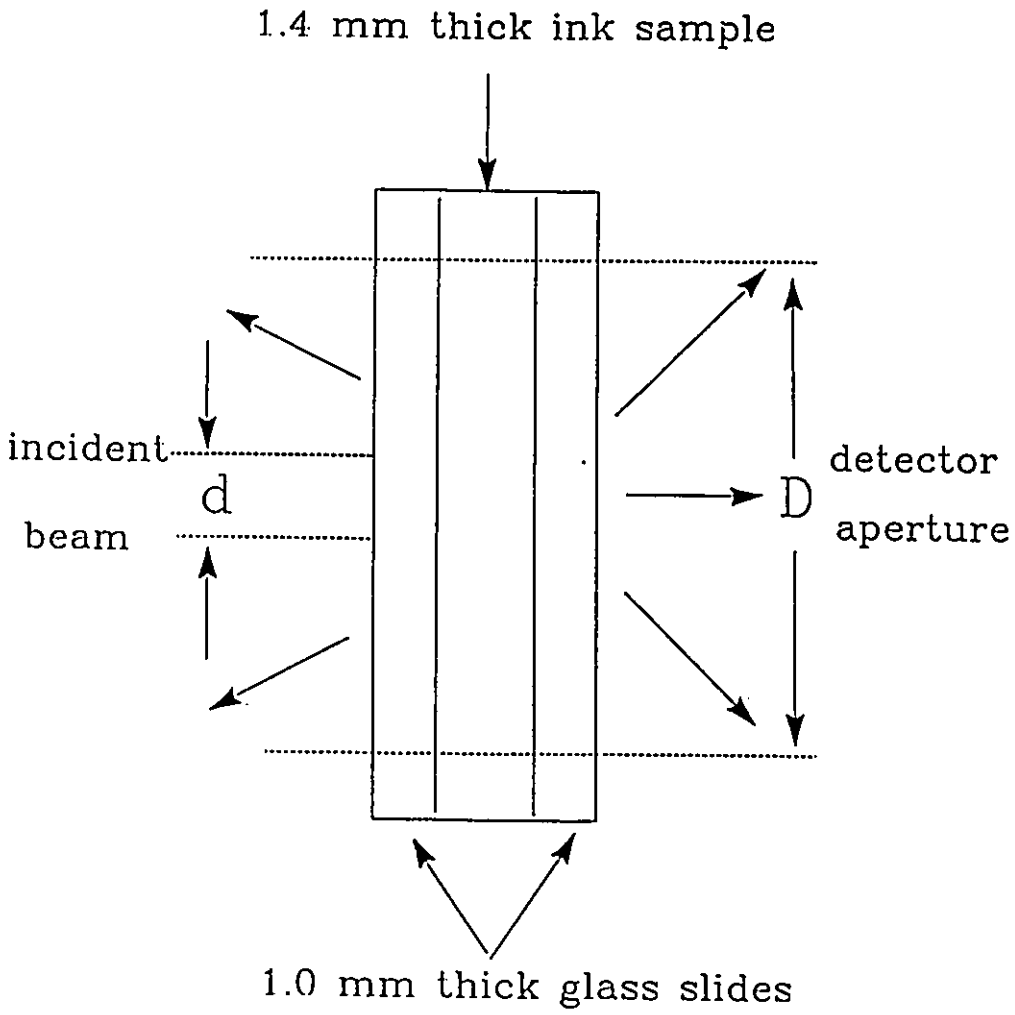

Figure 2.5 Geometry used in the Monte Carlo simulation of reflectance and transmittance measurements.

The input to the Monte Carlo program included the geometric parameters d and D as well as a, g and μ_t of the ink sample. Specular reflectances were calculated using the Fresnel coefficients for randomly polarized light. The program was run for a selected set of the parameters a, g and μ_t using d = 1.5 mm and D = 12.7 mm to correspond with the experimental conditions. The albedo and anisotropy were obtained from the results by determining the combination yielding R_c and T_c values matching most closely the experimental values, R_m and T_m. The total attenuation coefficient was determined directly by a narrow beam experiment.

Pathlengths in ink were calculated using the cumulative distribution sampling method (Carter and Cashwell 1975) given by

$$l_j = -\ln|n_j|/\mu_t \qquad (23)$$

where n_j is a randomly generated number between 0 and 1. For interactions in ink, the scattering angle was randomly sampled from the Henyey-Greenstein function. The azimuthal angle was randomly and uniformly sampled between 0 and 2π. Survival weighting was used for each interaction as a means of variance reduction, i.e., each interaction was assumed to be a scatter, with absorption accounted for by reducing the photon weight. The scattered weight after the interaction was the product of the albedo and the weight of the photon prior to the interaction. For interactions at glass-air interfaces, the Fresnel reflection coefficient replaced the albedo in the product. The weighted fraction which crossed the glass-air interface within the limits of the detector aperture was scored as reflected or transmitted depending on the surface through which

it escaped. The history of the scattered fraction continued until the surviving weight fell below a sufficiently small value that roulette (Carter and Cashwell 1975) was used to determine the fate of the particle. The simulation then continued with the selection of a new photon.

For each Monte Carlo run, R_c and T_c were determined from 5000 photon histories. In each case the photons were divided into five groups of 1000 photons with the uncertainties in R_c and T_c taken as the standard uncertainties in the mean of the value obtained for the five groups. In almost all cases, the relative errors were within 2 %.

2.2.5 Materials and methods

(i) Ink samples

Two different commercial brands of India ink (Higgins - Faber-Castell Corp., N.J. and Regal - L.A. Reeves Inc., Downsview, Ont.), were investigated. Two samples of Regal ink purchased one year apart were investigated to check for batch variations. All samples were diluted to 0.01 - 1 % with de-ionized water. The sample holder consisted of two glass spacers sandwiched between two 1 mm thick glass slides and sealed with epoxy: pathlengths 1.40 to 1.50 mm. The ink particles were sized using the electron microscope at McMaster University. The ink sample was prepared by passing a 0.01 % solution of Regal 1 ink through a 30 nm filter, which was then placed on a stub, air dried and coated with gold. No fixatives were used.

(ii) Apparatus

A 5 mW He-Ne (λ=594 nm) laser (PMS Electro-Optics Div., CO) was used as the light source, attenuated where necessary by neutral density filters. For all measurements the incident beam was modulated by a mechanical chopper (80 Hz) so that lock-in detection could be used.

(iii) Total attenuation measurements

To measure μ_t, the laser beam was incident directly onto a photodiode coupled to a preamplifier (Figure 2.6). The samples were positioned approximately 100 cm in front of the photodiode and a 1.0 mm aperture was placed over the diode. The solid angle subtended by the detector was thus 7.85×10^{-7} sr.

In accordance with Beer's Law, the attenuation coefficient of the ink sample is given by

$$\mu_t = -\frac{1}{t}\ln\left(\frac{I}{I_0}\right) \qquad (24)$$

where I is the intensity with the sample between the source and detector assuming no scattered light is detected, I_0 is the intensity with a water sample and t is the pathlength of the cuvette.

For each ink brand, measurements of μ_t were made at concentrations of 0.01, 0.05, 0.1, 0.5 and 1.0 %. Five measurements were made at each concentration and the mean and standard deviations evaluated. The total attenuation coefficient was then plotted as a function of concentration. The points were fitted to a straight line and μ_t determined from the slope of this line.

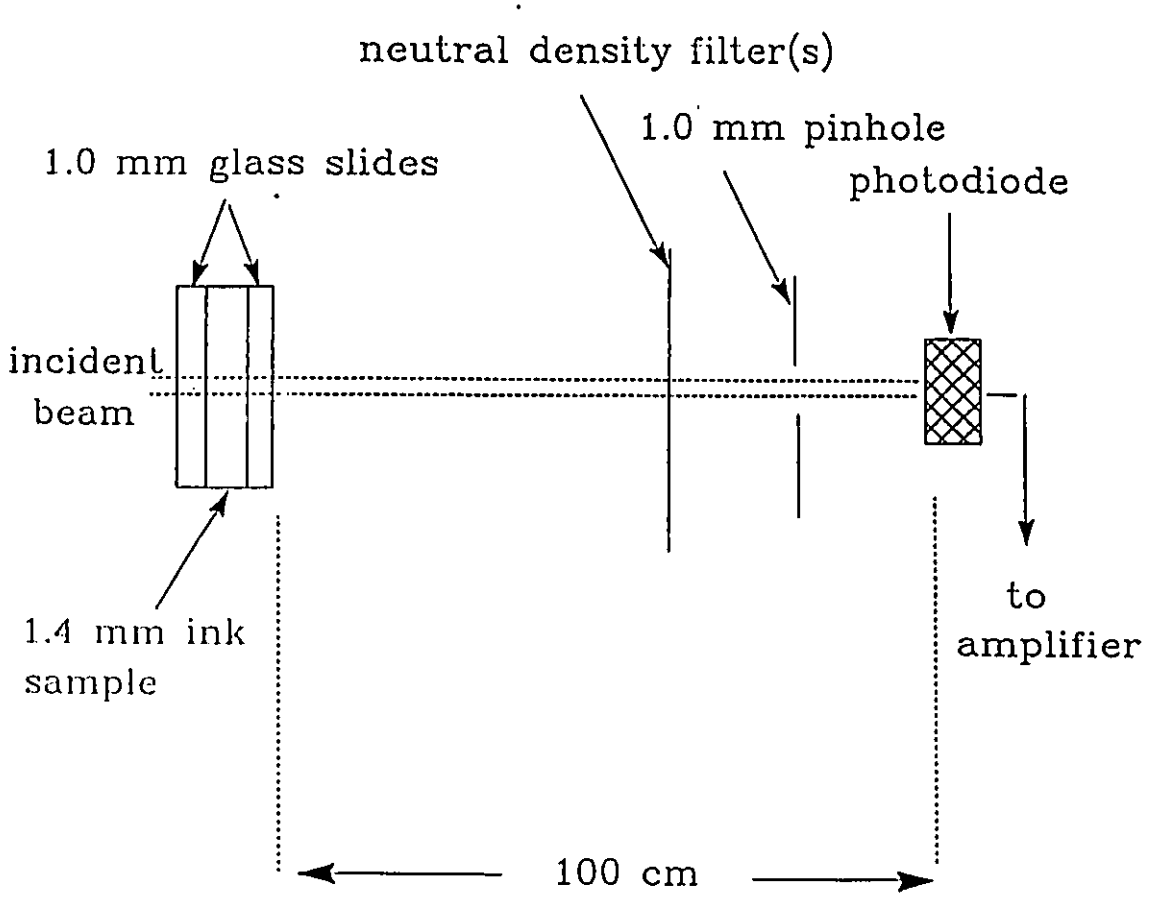

Figure 2.6 Experimental setup for measuring the total attenuation coefficient.

(iv) Reflectance and transmittance measurements

Standard integrating sphere techniques were used to measure the diffuse reflectance and transmittance. The geometry for measuring reflectance is shown in Figure 2.7. The sphere was 10.2 cm in diameter and contained two opposing beam ports, 1.27 cm in diameter. A third port, located at 90° to the other ports, was used to mount a photodiode detector for measurements of the diffuse reflectance and transmittance. A light baffle was inserted between the detector port and the sample port to ensure multiple internal reflections before detection. The inner surface of the sphere was coated with barium sulphate. For transmittance measurements, the sphere was rotated 180° and the open port was covered with a barium sulphate reflective plate.

For both detector geometries, the signal from the photodiode was amplified using a lock-in amplifier. The incident beam was modulated by a mechanical chopper which also provided a reference signal to the lock-in amplifier.

For the geometry used here, the reflectance of the sample is given (Kortum 1969) by

$$R = R_s \left(\frac{I_R}{I_S} \right) \tag{25}$$

where I_R is the reflectance measured with the sample, I_S is the reflectance measured with a barium sulphate reflective plate in the sample position and R_S is the reflectivity of the barium sulphate sphere coating (0.965: Peters et al. 1990). Similarly, the transmittance can be approximated as

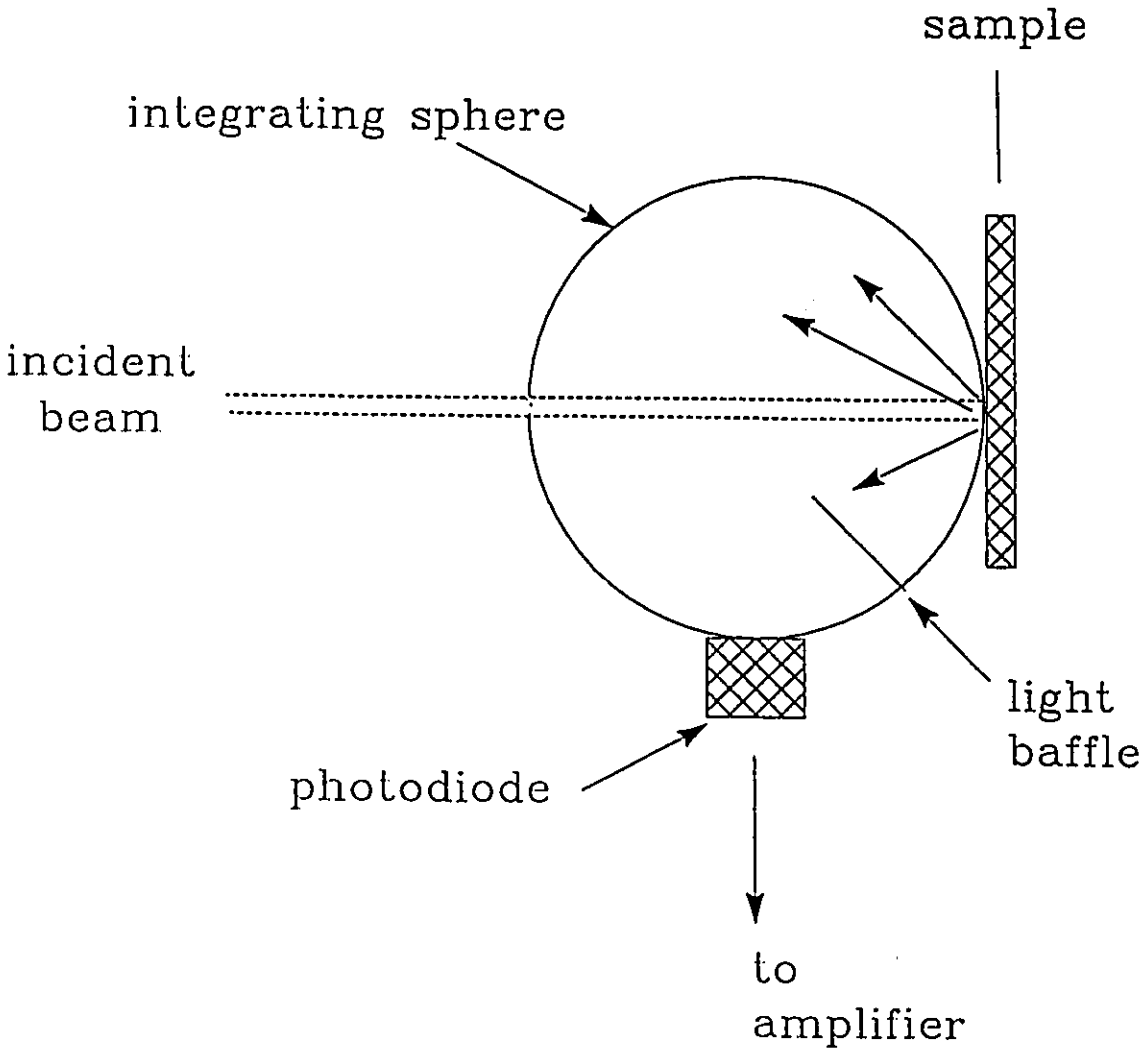

Figure 2.7 Integrating sphere geometry used for the measurement of reflectance. For transmittance measurements the sphere was rotated 180° on the vertical axis and the open port covered with a barium sulphate reflective plate.

$$T = R_s \left(\frac{I_T}{I_s} \right) \tag{26}$$

where I_T is the transmittance measured for the sample. I_s is the reflectance measured with the barium sulphate reflective plate covering the exit port and no sample.

For each brand of ink, measurements of R_m and T_m were made over the same concentration range previously described, and the mean and standard deviations evaluated from five measurements at each concentration. Equations (25) and (26) were used to evaluate R_m and T_m, which were compared to the Monte Carlo R_c and T_c values in order to determine a and g. The albedos were then compared to those derived from Mie theory.

2.2.6 Results

Analysis of the electron micrographs revealed an approximately bimodal size distribution with particle diameters around 0.1 and 1.0 μm. The small particles were nearly spherical and appeared structureless. Here they will be considered as single spherical particles. The large particles were highly irregular and may have consisted partly of aggregates of smaller particles. There were approximately 200 small (dia. ≈ 0.1 μm) and 3 ± 1 large (dia. ≈ 1.0 μm) particles in the field of view of a typical micrograph: that in Figure 2.8 contains 210 single (dia. = 106 ± 33 nm) and 3 large ink particles (indicated by the white arrows).

The optical properties of the three ink samples considered in this study are summarized in Table I. There was no systematic concentration dependence of g and a

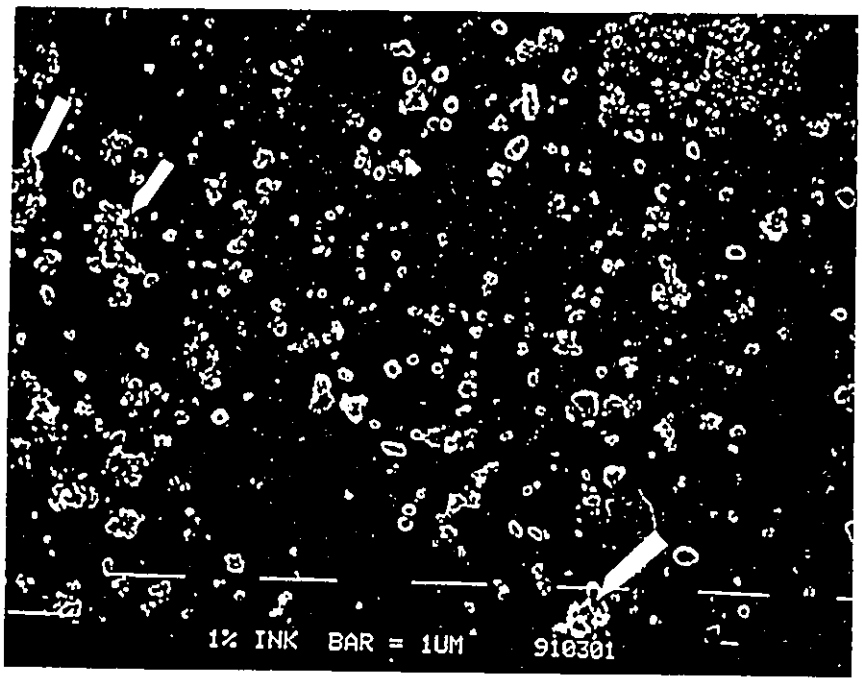

Figure 2.8 Electron micrograph of a 1 % solution of Regal ink. The large ink particles (dia. ~ 1 μm) are denoted by the arrows.

Table I

Optical Properties of Three Ink Solutions at 594 nm

Sample	μ_t ($mm^{-1}/\%$)	g	a
Regal 1	7.17 ± 0.05	0.69 ± 0.09	[illegible]9 ± 0.04
Regal 2	34.5 ± 1.0	0.78 ± 0.08	[illegible] ± 0.05
Higgins	12.3 ± 0.2	0.68 ± 0.10	0.31 ± 0.05

over the measured concentration range studied. The optical properties of Regal 2 were significantly different from those of the other samples, whereas the scattering anisotropy and albedo of Regal 1 and Higgins were in good agreement.

The total attenuation was evaluated at several concentrations using equation (24). For each sample, the value listed in Table I corresponds to the slope of a straight line fit of μ_t versus concentration. The mean values of a and g were determined as follows. At each concentration, the experimentally determined μ_t was input to the Monte Carlo code along with pre-selected values of a and g. For example, for fixed μ_t and g, simulations were initiated for values of a ranging from 0.20 to 0.50 in increments of 0.02. Since g ranged from 0.50 to 0.86 (0.02 increments), a total of 304 simulations (yielding 304 distinct sets of R_c and T_c) were performed for a given μ_t. The range of a and g over which the Monte Carlo results (R_c and T_c) were within the experimental uncertainties in the measured (R_m and T_m) values were recorded. The mean values listed in Table I are the midpoints of these ranges.

2.2.7 Discussion

Assuming that the ink particles are spheres suspended in water ($n_0 = 1.333$) and that they can be classified simply as either large or small, it should be possible to calculate the albedo given the complex refractive index of carbon. Using $m = 1.488 - 0.495i$ for carbon in water (Senftleben and Benedict 1919), the albedo has been plotted as a function of the percentage of large particles (N_l: Figure 2.9).

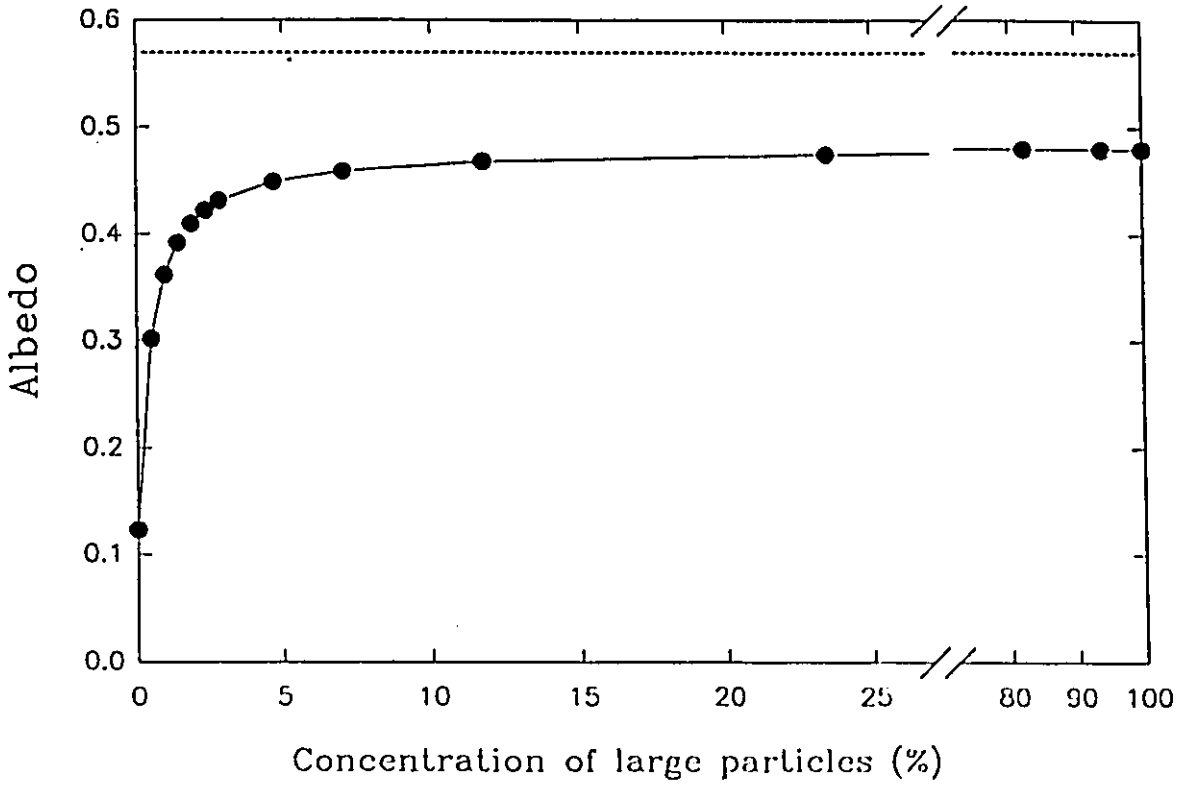

Figure 2.9 Albedo vs. large particle concentration. The dashed line represents the limiting albedo in the geometrical optics regime for carbon spheres suspended in water (Kerker 1969). The symbols represent the calculated albedo based on the theory of section 2.2.3.

Small particles (N_l = 0) have a small scattering efficiency (Q_s = 0.108) but a substantial absorption component (Q_a = 0.836). A solution of such particles acts approximately as a black body, as indicated by its low albedo (0.115). The results of Irvine (1965) show that the scattering is nearly isotropic; g ≈ 0.09.

For a solution composed entirely of large particles, anomalous diffraction theory yields an albedo of approximately 0.48 (Q_s = 0.907 and Q_a = 0.982). Mie theory calculations by Irvine (1965) show that the scattering is highly forwardly peaked; g ≈ 0.88. As previously stated, anomalous diffraction theory is strictly valid only if n ≈ 1 and $n\kappa \ll 1$. The results of Deirmendjian (1960) imply that the theory is valid if $1 < n \leq 1.50$ and $0 < n\kappa \leq 0.25$. Clearly, the second condition is violated since $n\kappa \approx 0.50$ for the ink particles studied here. However, the calculated albedo (0.48) was in good agreement with the albedo (0.50) of identically sized spheres of comparable refractive index (m = 1.59 - 0.66i) as determined from Mie theory by Fenn and Oser (1965), suggesting that anomalous diffraction theory is adequate for the purposes of this study.

The absorption efficiencies of the large (Q_a = 0.982) and small (Q_a = 0.836) particles are much closer than the corresponding scattering efficiencies. Thus, in a solution containing both types of particles the albedo is dominated by the large particles, as illustrated in Figure 2.9. Likewise, the high g values indicate that the scattering anisotropy is dominated by the large particles.

From Figure 2.9 it can be seen that there is a rapid initial rise in albedo with increasing concentration of large particles. For example, for a large particle concentration (C_l) of 4.7 %, the albedo (0.45) has already reached 93 % of its final value. Based on the

electron microscopy results, the albedo of the Regal 1 solution (C_i = 1.4 ± 0.5 %) should range from 0.36 to 0.41, which is in fair agreement with the experimental albedo (0.29 ± 0.04), given that only two distinct particle sizes were considered.

The sensitivity of the albedo to N_l is a potential problem for practical phantom studies, since different ink solutions may have different concentrations of large particles. The fact that the two different ink brands studied here (Regal 1 and Higgins) had almost identical albedos (Table I) is probably fortuitous, especially in view of the large albedo variation between Regal 1 and Regal 2. The high albedo of the Regal 2 sample is probably due to a greater concentration of large ink particles, as indicated by the high μ_l and g values.

2.2.8 Conclusions

The results presented here show that the optical attenuation coefficient of India ink has a significant scattering component, and it cannot be regarded as a pure absorber. The scattering component is due mainly to a small fraction of micron-sized particles. The scattering cross section and, hence, the albedo is very sensitive to the concentration of these large particles. The observed discrepancies between the albedos of different ink solutions can probably be explained on the basis of this large particle dependence. The anisotropy parameter is also strongly dependent on the size distribution, tending to higher values as the particle size increases.

The non-negligible scattering can cause two types of error in optical phantom work

if the ink is assumed to be a pure absorber: i) it may lead to underestimation of the total phantom scattering if the concentration of ink is high compared to that of the scattering medium itself and, more importantly, ii) it causes an overestimation of the absorption if this is determined, for example, using spectrophotometry or μ_t measurement of the ink solution.

Determination of the optical properties of ink is a tedious procedure involving time consuming measurements and simulations which must be repeated for every sample of ink, due to the possibility of inter-brand and inter-batch variations. Once determined, however, these properties appear to be stable over time, as no significant variation in μ_t has been observed over a period of several months for a given ink solution. A simpler alternative is to use, where possible, non-particulate absorbers, such as molecular dyes (Anderson et al. 1989 and Moes et al. 1989), for which scattering is insignificant.

CHAPTER 3

TIME-RESOLVED STUDIES IN HOMOGENEOUS PHANTOMS

3.1 Introduction

Knowledge of the optical properties of tissue has become important in recent years due to the increased use of optical techniques in diagnostic and therapeutic medicine. For clinical applications it is desirable to develop noninvasive techniques to determine tissue optical properties in vivo. This implies that such information must be deduced from measurements of the light scattered out of the tissue. Steady-state reflectance spectroscopy may be employed to obtain this information but, as previously discussed, this technique is somewhat cumbersome since it requires several independent measurements at different source-detector spacings to yield the optical properties of interest (Patterson et al. 1989).

Significant advances in noninvasive measurements have been made possible through the use of time-resolved diffuse reflectance and transmittance measurements. These have become feasible with the advent of picosecond pulsed laser sources and fast photodetector systems such as streak cameras and microchannel plate photomultiplier tubes operating in time-correlated-single-photon-counting mode (Wilson et al. 1989). Yoo et al. (1990a and 1990b) have shown that the temporal dependence of the coherent backscatter peak can be related to the scattering and absorption coefficients. An alternative approach is to examine the temporal broadening of a pulse due to multiple scattering as the light propagates from source to detector. The shape of the detected pulse

also depends strongly on the tissue optical properties.

Determination of the optical properties from the detected pulse requires a model of light propagation. Patterson et al. (1989) have proposed a simple model based on diffusion theory which yields analytical expressions for the time-resolved diffuse reflectance and transmittance from a slab in terms of the absorption and transport scattering coefficients. Some predictions of this model have been shown to be in good agreement with Monte Carlo computer simulations (Patterson et al. 1989 and Madsen et al. 1991). Preliminary experimental results by Wilson et al. (1989) have shown the pulse shape recorded from a tissue-simulating semi-infinite phantom to be in qualitative agreement with the predictions of the model, but thorough quantitative tests of its validity were not undertaken.

The purpose of the work reported here was to test the accuracy of estimates of the absorption and transport scattering coefficients made by fitting the analytical expressions of diffusion theory for the pulse shape to experimental observations. Initially, the validity of the model was examined in the geometry for which it was derived (a semi-infinite medium) over a range of transport scattering and absorption coefficients. The thickness of the phantom was then decreased to study the influence of finite slab thickness on the derived coefficients. The model was also tested under more biologically realistic conditions using spherical and cylindrical phantoms. Exact solutions in these geometries are avalilable (Madsen et al. 1991), but they suffer from the computational complexities associated with the repeated evaluation of series of cylindrical and spherical Bessel functions. By varying the size of the different geometries and the separation between

source and detector, the effects of the boundaries on the optical properties estimated using the simple model were studied.

3.2 Theory

Only the salient features of the diffusion model will be described here. For a comprehensive derivation of this model, the original paper by Patterson et al. (1989) should be consulted. The model is derived assuming a narrow collimated pulsed light beam normally incident on the surface of a semi-infinite homogeneous tissue slab. The time-dependent diffusion equation, as derived from the equation of radiative transfer (Patterson et al. 1989) is given by

$$\frac{1}{c}\frac{\partial}{\partial t}\phi(\underline{r},t) - D\underline{\nabla}^2\phi(\underline{r},t) + \mu_a\phi(\underline{r},t) = S(\underline{r},t) \qquad (27)$$

where D is the diffusion coefficient,

$$D = [3(\mu_a + \mu_s')]^{-1} \qquad (28)$$

and $S(\underline{r},t)$ is the photon source. Note that $S(\underline{r},t) = \delta(\underline{r},t)$ for an impulse from an isotropic point source.

If we assume that all the incident photons are initially isotropically scattered at a depth of one effective mean free path,

$$z_0 = [(1-g)\mu_s]^{-1} \qquad (29)$$

the actual source term becomes the simple delta function described above. We also

assume that $\phi(\underline{r},t) = 0$ on the surface of the tissue ($z = 0$). This boundary condition is not physically the most correct but, as discussed later, results in an expression for the pulse shape which is quite accurate. It may be satisfied by adding a negative source of photons to the infinite medium geometry (Eason et al. 1978) - an application of the method of images.

Given the above assumptions, equation (27) may be solved to yield an expression for the local reflectance (relative number of photons reaching the surface per unit time per unit area) as a function of radial distance (ρ) and time (t) after the initial scatter

$$R(\rho,t) = (4\pi Dc)^{-3/2} z_0 t^{-5/2} \exp(-\mu_a ct) \exp(-\frac{\rho^2+z_0^2}{4Dct}). \qquad (30)$$

The small time delay (a few picoseconds) between entry of the light pulse into the turbid medium and the first scatter will be ignored in the remainder of the chapter.

From equation (30) it follows that the optical properties of a semi-infinite slab medium can be obtained through measurements of the diffusely reflected light some distance from the source as a function of time. In all cases presented here, the validity of the diffusion model was tested by fitting equation (30) to the experimental data.

3.3 Materials and methods

The experimental setup is illustrated in Figure 3.1. A mode-locked frequency-doubled Nd:YAG (Coherent Antares 76-s) emitting a train of 532 nm pulses at 76 MHz pumped a cavity-dumped (1 MHz) dye (Rhodamine 6G) laser. The resultant 588 nm 25

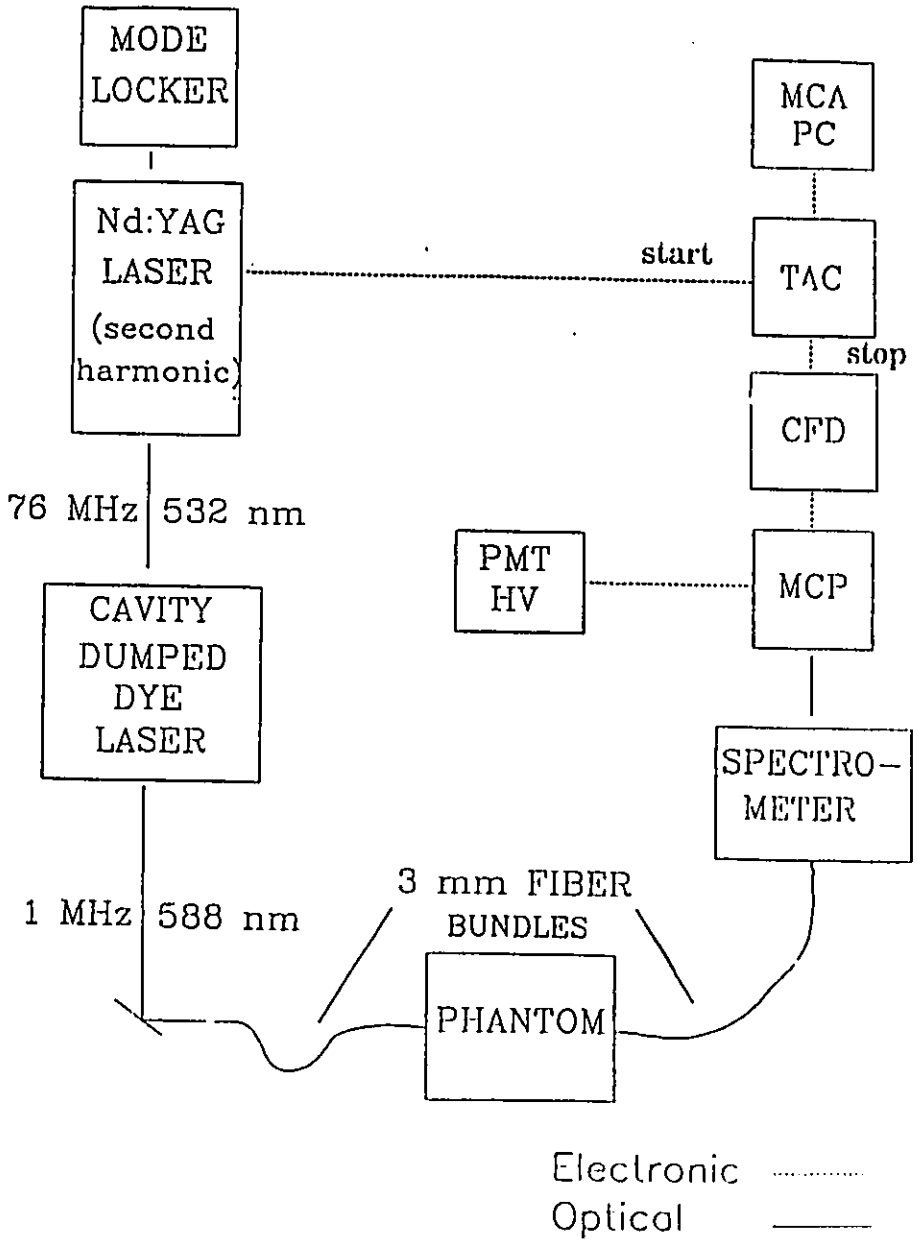

Figure 3.1 Experimental apparatus for the measurement of time-resolved diffuse reflectance.

nJ pulses (FWHM = 5 ps) passed through a series of neutral density filters and were coupled into a one metre long 3 mm diameter fiber bundle in contact with the phantom. The diffusely reflected light was collected with an identical fiber bundle located at various positions around the phantom. This fiber was coupled to the detector through a grating monochromator which was incidental to the present experiments. The photon counting system consisted of a microchannel plate photomultiplier tube (MCP-PMT), a constant-fraction timing discriminator (CFTD), a time-amplitude converter (TAC) and a multichannel analyzer (MCA). The MCP-PMT (Hamamatsu R1564U-01) was operated at 3000 V and the neutral density filters adjusted to give a count rate of approximately 2.5 kcps. In almost all cases, a data acquisition time of 3 minutes was used for each reflected pulse measurement. The amplified detector output, fed to the CFTD, provided the stop pulse to the TAC (Canberra 2143). The start pulses were obtained electronically from the Nd:YAG laser. The TAC output, which is proportional to the time interval between start and stop pulses, was then sent to the 4096 channel MCA. The time resolution of the system, as determined from the full width at half-maximum of the directly detected pulse (fiber bundles abutted), was approximately 120 ps.

In all cases a dilute solution of 20% Intralipid (Kabivitrum Inc., Ca) and deionized water was used as the scattering medium. In these experiments the inter-particle distance ranged from 2.7 to 5.3 μm. As described in Chapter 2, a steady-state technique derived from time-independent diffusion theory, commonly referred to as the added absorber or poisoned moderator method (Profio and Sarnaik 1984 and Wilson et al. 1986), was used to determine the optical properties (μ_a and μ_s') of this scattering medium. The absorption

of the medium was controlled independently by the addition of India ink.

In the tissue-like phantoms ($\mu_a \approx 0.01$ mm^{-1}) the absorption contribution of Intralipid (4.13×10^{-4} mm^{-1} for 1 % solids) was negligible compared to that of ink, while, at the lowest concentration of added absorber, the Intralipid accounted for approximately 40 % of the total absorption. This is only a rough estimate since the absorption coefficient of Intralipid is difficult to determine accurately. In situations where Intralipid accounts for a large percentage of the total absorption, i.e., in phantoms with low ink concentrations, uncertainties in the Intralipid absorption coefficient may result in discrepancies between the steady-state and time-resolved absorption coefficients.

At all concentrations considered, it was assumed that the scattering properties of the phantom material were determined entirely by Intralipid while, under tissue-like conditions, its absorption properties were governed by the added absorber (ink). The optical properties of India ink have been discussed in Section 2.2.

In the first set of experiments, the diffusion model was tested in a slab geometry. The phantom consisted of a black, non-reflecting lucite box (200 x 200 x 150 mm) with a height adjustable lid holding the source and detector fibers. Pulses were acquired as a function of fiber separation (ρ = 30, 50 and 70 mm) and slab thickness. The thickness was determined by the distance of the lid from the bottom of the phantom (d = 10, 55 and 100 mm). The derivation of equation (30) assumes that the speed of light is the same inside and outside the scattering slab, i.e., refractive index matching. In a separate experiment designed to study the influence of a mismatch in refractive index on the measured pulse shape, a solid gelatin phantom containing known amounts of ink and

Intralipid was prepared. This had absorption and scattering coefficients of approximately 0.001 and 1.0 mm^{-1} respectively. By leaving the phantom in air or immersing it in water, the diffusely reflected pulse could be measured under different boundary conditions.

In a further set of experiments, the utility of the slab diffusion model was examined in cylindrical and spherical geometries even though equation (30) is not strictly applicable to these cases. Three different sized cylinders (radius of 20, 40 and 50 mm) and spheres (radius of 25, 50 and 75 mm) were used. The cylinders (length 100 mm) were made of black polyvinyl chloride. At the midpoint of each, holes were drilled around the circumference and pulses were acquired by placing the source and detector bundles in contact with plastic windows covering these holes. Identical plastic windows were used to cover similar holes in the spheres which were manufactured from aluminum. In the cylindrical phantom experiments, pulses were acquired at four different angles (45, 90, 135 and 180°). Due to time constraints, acquisition of data at 135° was omitted from the spherical experiments. The interior surfaces of the cylinders and spheres were coated with a black non-reflecting paint and, in both cases, the phantoms were placed in a light tight box to eliminate background light.

The model-derived pulse (equation (30)) was convolved with the measured system response and fitted to the data using a grid search chi-square fitting routine (Bevington 1969). Failure to perform the convolution resulted in significant errors when the width of the detected pulse was comparable to the system response. As a precaution, this convolution was, therefore, included as a part of all the fits. Three free parameters were varied in the fits - μ_a, μ_s' and an overall scaling factor. Only time bins with greater than

50 counts (10 times the background) were included in the fits. In all cases, the direct chord distance between source and detector rather than the distance along the surface was used in the model. The optimum values of the time-resolved absorption ($\mu_a tr$) and transport scattering ($\mu_s' tr$) coefficients obtained from the fitting procedure were then compared to the (μ_a and μ_s') obtained using the steady-state techniques.

3.4 Results and discussion

The response of the reflectance to changes in the fundamental optical properties of the test medium is illustrated in Figures 3.2 and 3.3. The solid curves represent the best fits to the experimental data. Figure 3.2 shows the changes in reflectance with added absorber while ρ and μ_s' were fixed. The addition of absorber results in a shift in the position of the peak to earlier times, a much more rapid decay of the pulse and an overall decrease in pulse amplitude. Changes in reflectance due to the reduced scattering coefficient (ρ and μ_a fixed) are illustrated in Figure 3.3. The final slope approaches the same value under both scattering conditions, while the peak shifts to longer times and the pulse broadens as the reduced scattering coefficient increases.

Typically, the reduced chi-square (χ^2_{red}) obtained in this study ranged from 1.0 to 3.0. A contour plot of the χ^2_{red} as a function of μ_a and μ_s' for a typical data set (Figure 3.4) shows that the χ^2_{red} space is very well behaved, i.e., there is a convergence to a global mimimum. Plots of the residuals versus time showed that the major contribution to the χ^2_{red} occurred at early times. There did not appear to be a systematic correlation between

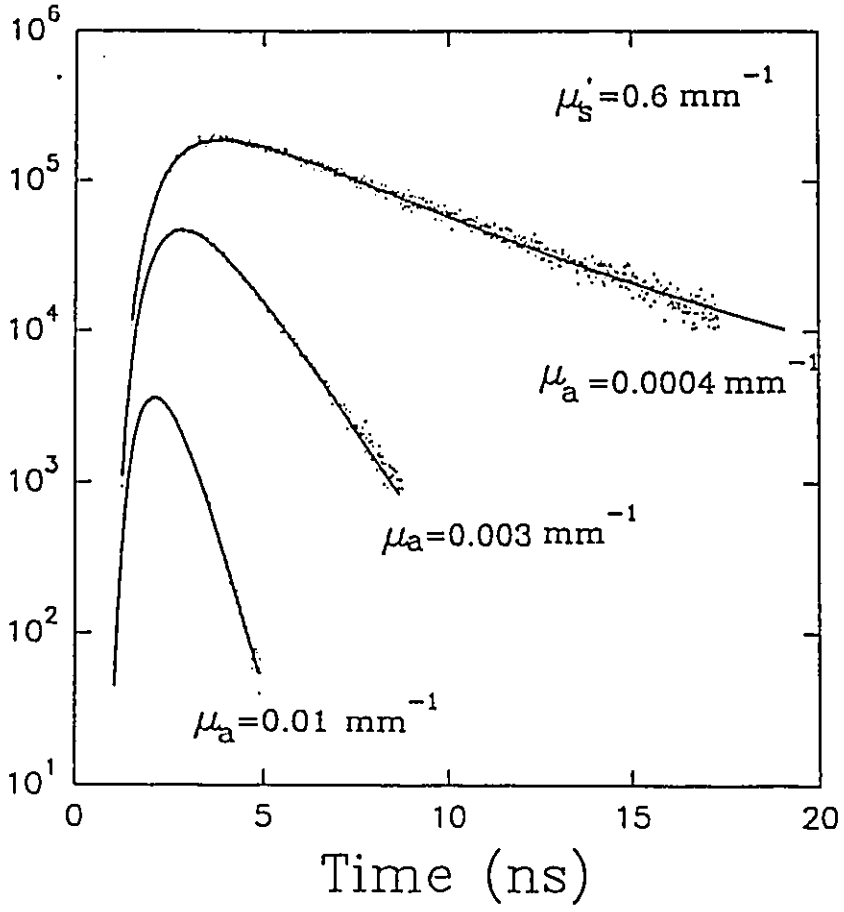

Figure 3.2 Pulse shape as a function of added absorber for the 100 mm thick slab phantom (ρ = 70 mm). The solid curves represent fits to the experimental data (dots) using the simple diffusion model of Eq. (30). The absorption coefficient is the sum of the Intralipid and ink coefficients as determined by steady-state methods. The values shown are the measured steady-state coefficients.

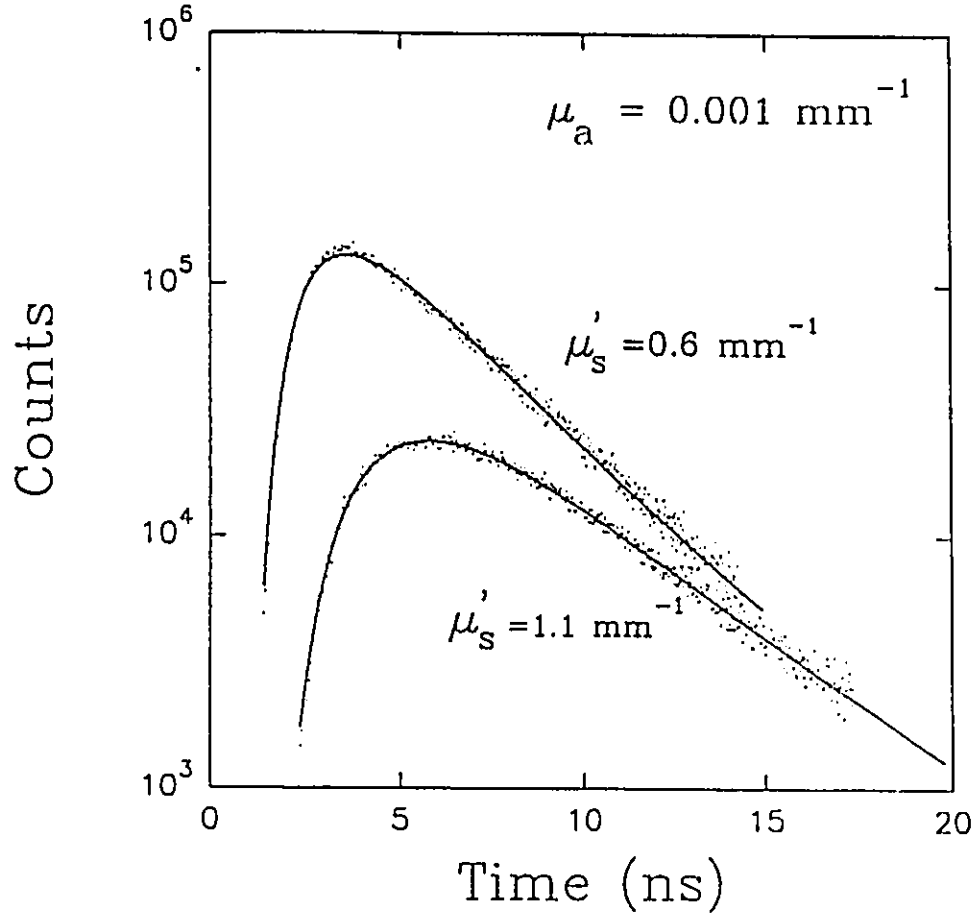

Figure 3.3 Pulse shape as a function of transport scattering coefficient for the 100 mm thick slab phantom (ρ = 70 mm). The solid curves represent fits to the experimental data (dots) made by using the simple diffusion model of Eq. (30).

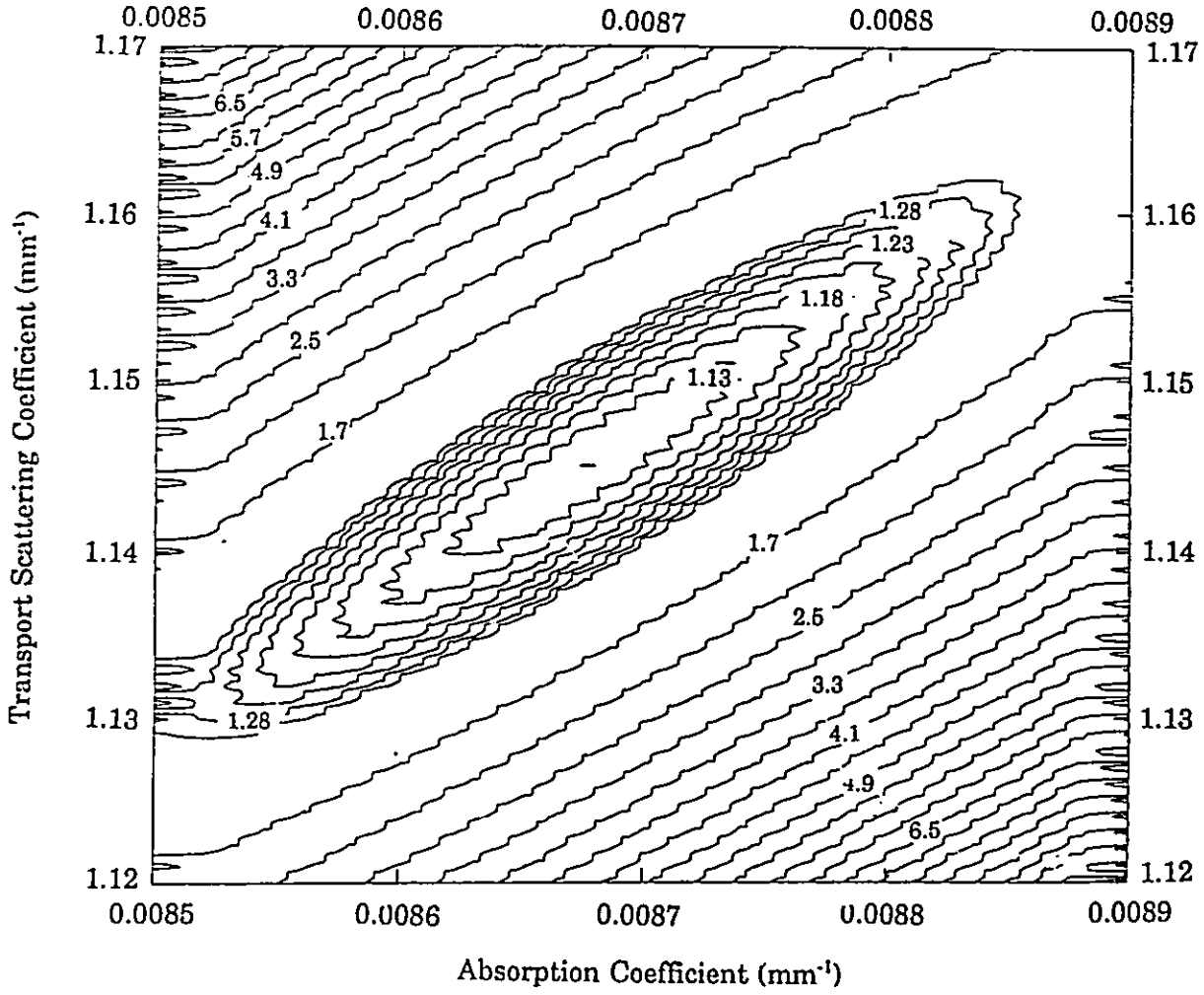

Figure 3.4 Contour plot of χ^2_{red} as a function of absorption and scattering for the 100 mm thick slab phantom (ρ = 50 mm).

χ^2_{red} and agreement of estimated optical properties with the steady-state values. The uncertainty in the fitted parameters was estimated from fits of measurements repeated under identical conditions and was less than 1 % in all cases.

Results in the thick slab geometry (d = 100 mm) are summarized in Figures 3.5a-f. Good correlations are observed between the time-resolved and steady-state absorption coefficients and between the time-resolved and steady-state transport scattering coefficients. Estimates of $\mu_a tr$ are best for small ρ and large μ_s', but differences do not appear to be systematic. For example, in the low scattering case (Figures 3.5a and b), $\mu_a tr$ is overestimated in almost all cases at 30 mm, while at 70 mm there is good agreement throughout the absorption range examined. Conversely, in the high scattering case (Figures 3.5c and d), the overestimate in $\mu_a tr$ is greater at 70 mm. The estimate of $\mu_s' tr$ (Figures 3.5e and f) depends somewhat on μ_a and is very good in almost all cases.

The results of greatest interest in this study were those obtained in media with optical properties most closely resembling those of tissues. Under such conditions (μ_a = 0.01 mm^{-1} and μ_s' = 1.0 mm^{-1}), the noninvasive time-resolved method employed here yielded optical parameters accurate to within 10 % in the thick slab. The reasons for the systematic overestimate of $\mu_a tr$ is not understood. The influence of finite phantom size does not explain this trend since a reduction in the phantom thickness by a factor of two (see below) did not significantly change the estimates of $\mu_a tr$ and $\mu_s' tr$. It appears, therefore that the phantom is sufficiently large to be regarded as semi-infinite.

Another possibility is that the diffusion model does not provide a sufficiently accurate description of radiation transport. Discrepancies between diffusion theory and

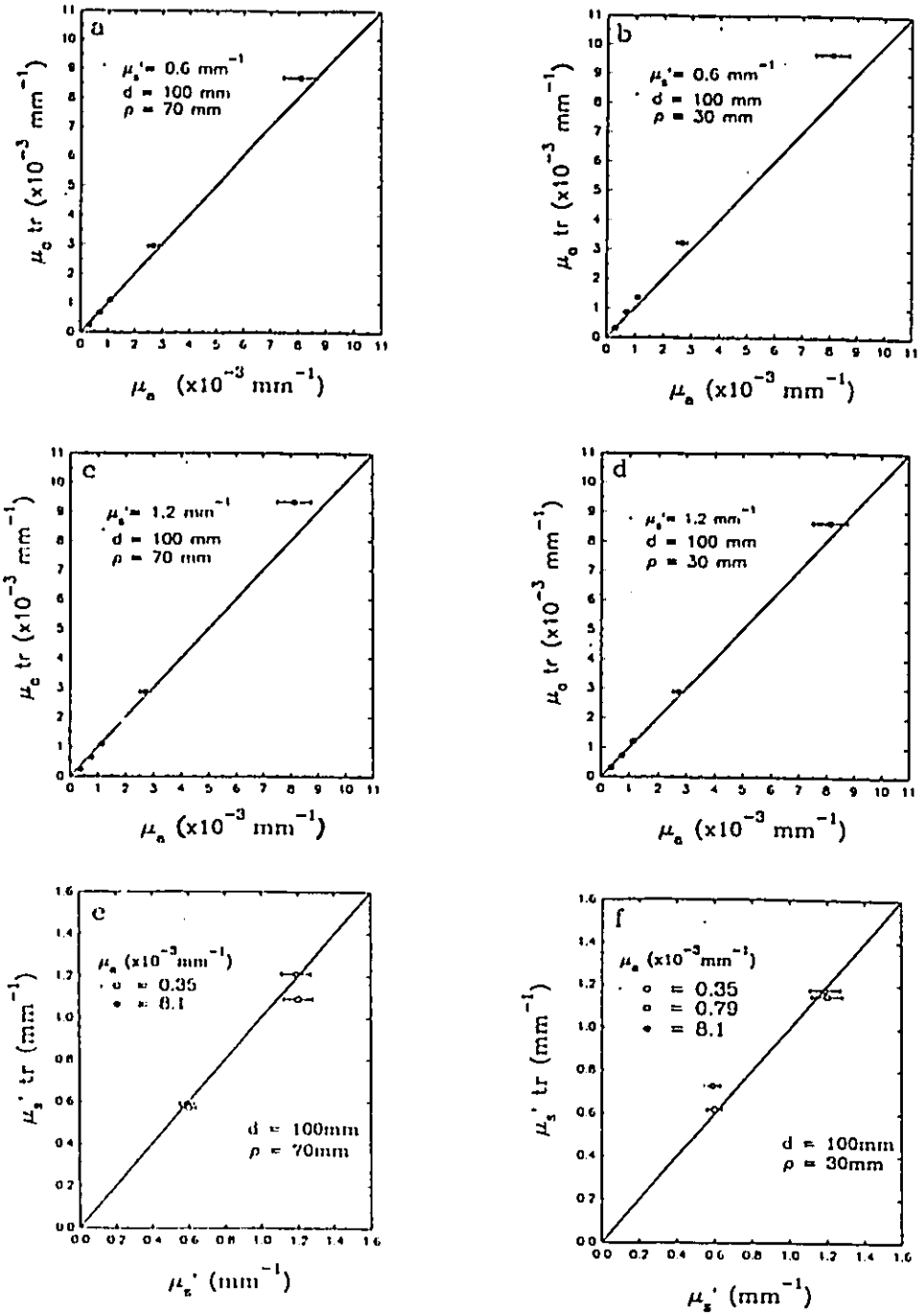

Figure 3.5 Summary of time-resolved versus steady-state results in the thick slab (d = 100 mm) phantom. The solid line represents equivalence between the steady-state and time-resolved values.

experiment have been noted previously by Yoo et al. (1990) for the case of time-resolved transmission through a slab. As a test, a Monte Carlo simulation of the experiment was performed using the parameters μ_a = 0.01 mm^{-1} , μ_s' = 1.5 mm^{-1} and ρ = 10 mm. The transport scattering coefficient used in the Monte Carlo simulation was slightly higher than the corresponding experimental value (1.0 mm^{-1}) due to the fact that the simulations were performed prior to the evaluation of the optical properties of the phantom. However, this is more than compensated for by the smaller value of ρ used in the simulation. For computational speed, isotropic scattering (g = 0) was assumed even though Intralipid is known to scatter light primarily in the forward (g = 0.69) direction (Flock et al. 1987). We have performed Monte Carlo simulations which show that the pulse shape depends only on $(1-g)\mu_s$ and not on μ_s and g separately as long as the detected photons have undergone a large number of scattering events. As shown in Figure 3.6 the results of the Monte Carlo simulation are in excellent agreement with the prediction of the diffusion model. Using the Monte Carlo data as input to our fitting routine, we obtained estimates of 0.0098 mm^{-1} for the absorption coefficient and 1.48 mm^{-1} for the transport scattering coefficient. We also were able to discount the influence of finite source and detector size (up to the experimental diameter of 3 mm) on the results by changing these parameters in the Monte Carlo simulation.

In the Monte Carlo simulation and the diffusion model it was assumed that the boundary was either index matched or completely absorbing - in both cases photons reaching the boundary do not re-enter the medium. We attempted to create this situation in the experiment by coating the boundaries of the phantoms with flat black paint but

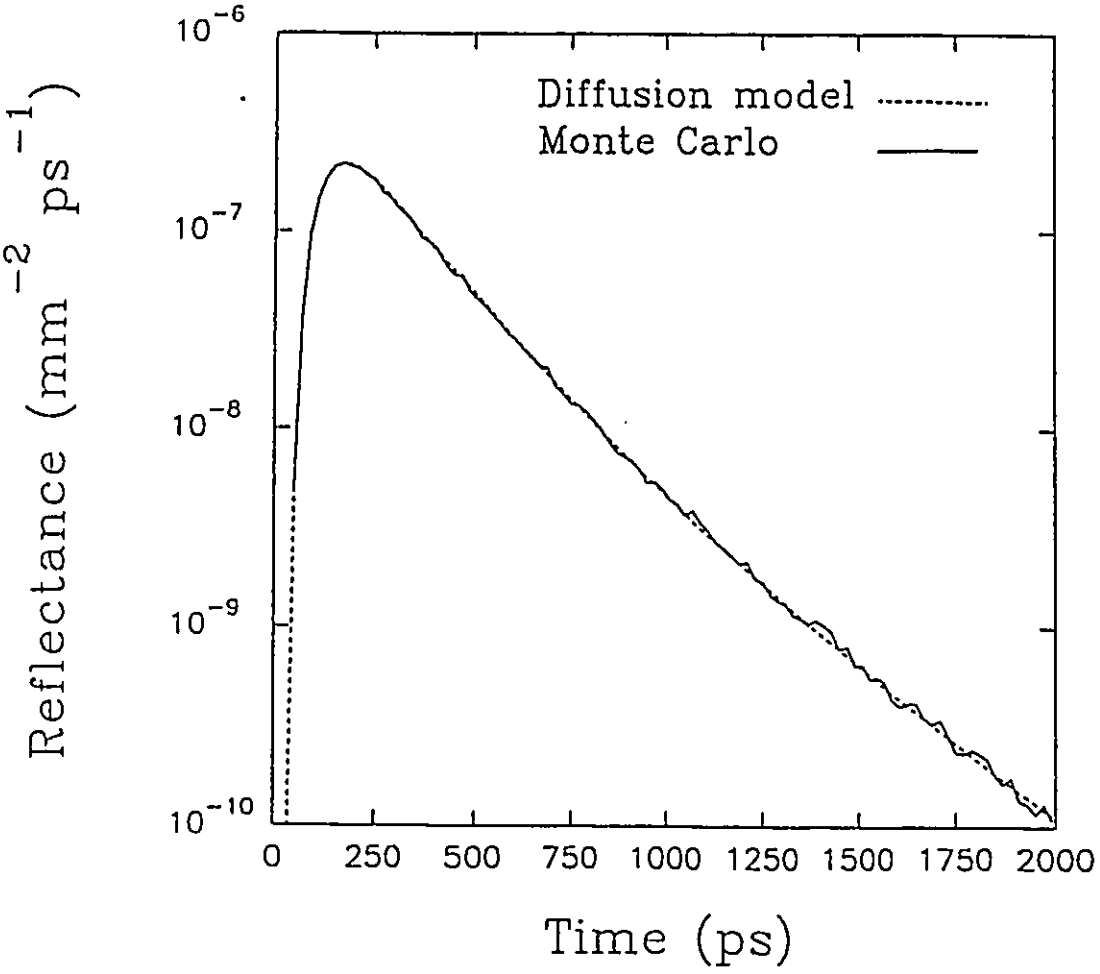

Figure 3.6 Comparisons of the predictions of the diffusion model and the Monte Carlo results. The diffusion model results have been matched to the Monte Carlo data at 170 ps. Better absolute agreement can be obtained with a more exact boundary condition (Patterson et al. 1990). The reflectance corresponds to the number of photons reaching the surface per unit time per unit area per incident photon. 2 x 10^6 photons were used in the simulations.

some diffuse reflectance could still occur. The influence of this internal diffuse reflectance on the observed pulse shape (and the estimated parameters) was studied in two ways. First, the diffusion model was extended to include internal diffuse reflectance by the use of an extrapolated boundary (Madsen et al. 1991). Even assuming a large mismatch (and hence reflection) at the boundary, we found no significant difference in the scattering and absorption coefficients found by fitting the measured pulse shape to this model. Secondly, we compared pulses measured in the gelatin phantom under matched (water/gelatin) and mismatched (air/gelatin) boundary conditions (Figure 3.7). Again, even though the absolute magnitude of the pulse was different, the pulse shape was practically identical except for small differences in the rising edge. The "kink" in the rising edge of the matched pulse is probably due to internal reflection of light from the water/air boundary. The discrepancy of 10 % or less in the absorption coefficient thus remains unexplained, but it should be noted that this uncertainty is acceptable for many biological measurements.

While the diffusion model was developed for a semi-infinite geometry, a second set of experiments was performed to test its utility in a range of other geometries. A summary of the geometries considered is shown in Figure 3.8. The presence of other boundaries where photons escape or are absorbed will cause preferential loss of long pathlength photons which would have been detected in a semi-infinite geometry. This should result in an overestimate in the absorption coefficient and an underestimate of the transport scattering coefficient. However, if the object is sufficiently large or the source and detector sufficiently close together, these effects may be insignificant.

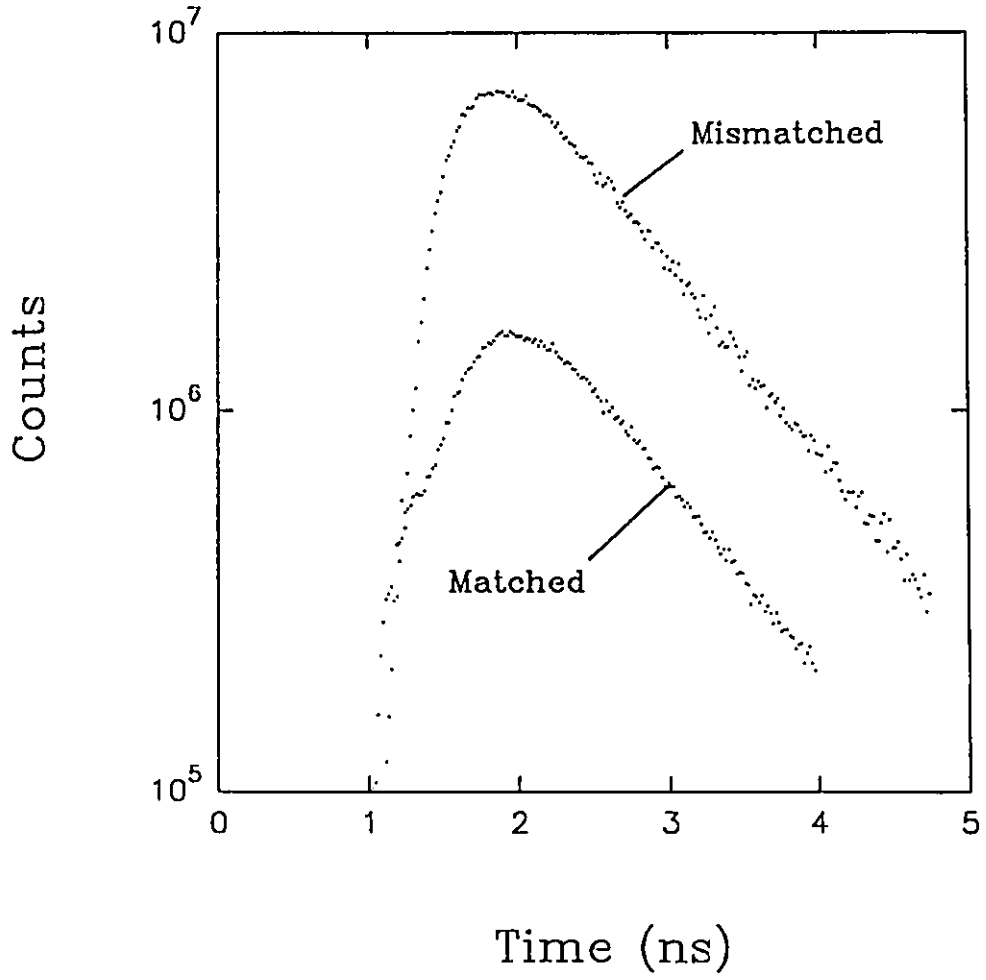

Figure 3.7 Measured pulse shapes under two different boundary conditions in a semi-infinite geometry. ρ = 15 mm, μ_a = 0.001 mm^{-1} and μ_s' = 1.0 mm^{-1}. Matched = water/gelatin, mismatched = air/gelatin.

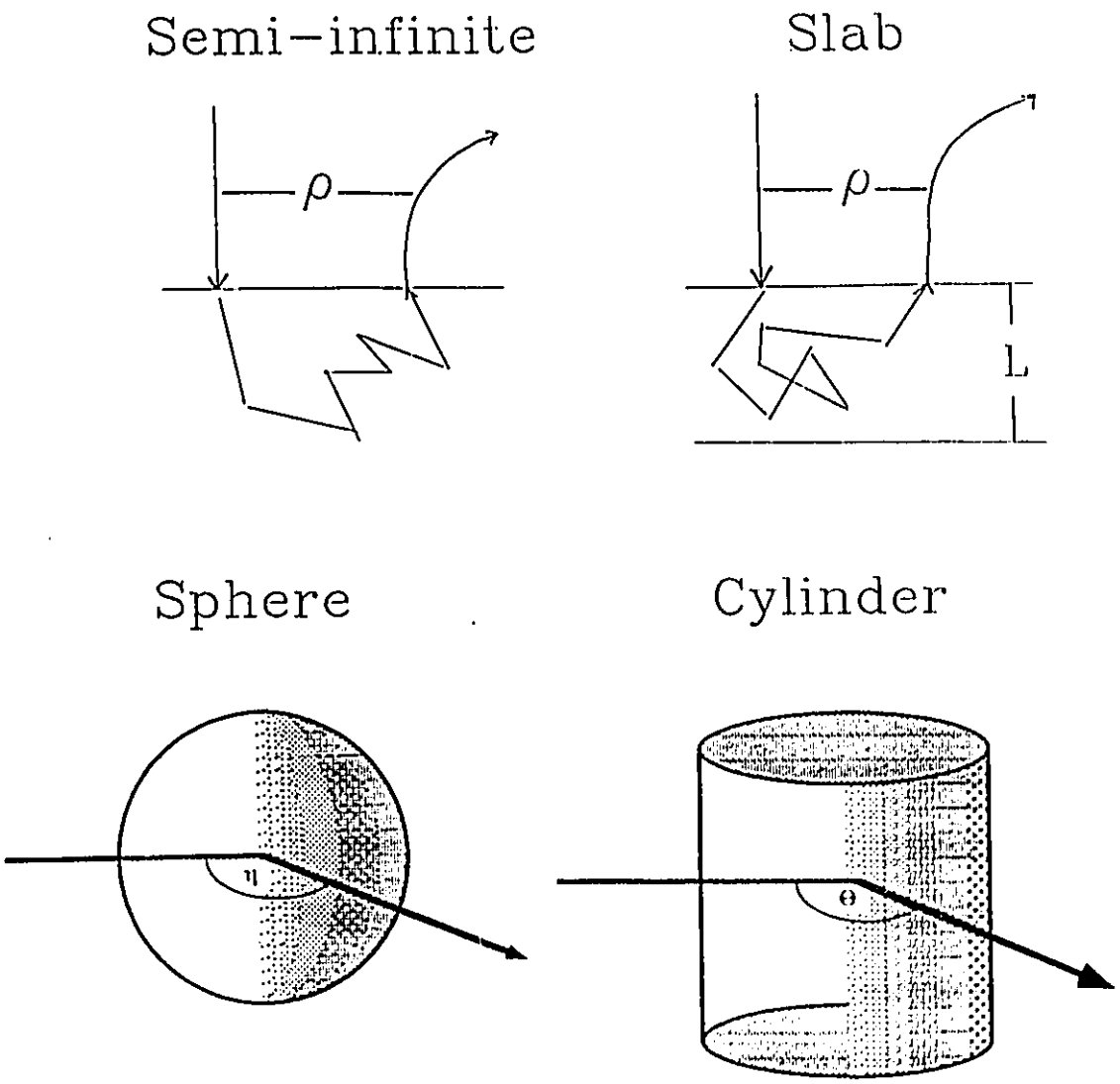

Figure 3.8 Summary of geometries considered. ρ is the source-detector separation, L is the slab thickness and η and θ are angles between the source and detector.

To illustrate this, we consider first a slab of limited thickness with $\mu_a = 0.01$ mm^{-1} and $\mu_s' = 1.00$ mm^{-1}. The absorption coefficient is at the low end of the range for normal tissues but this is the highest value which yielded useful signals at all values of ρ. In Figure 3.9 we have plotted the optical interaction coefficients derived using Eq. (30) as a function of slab thickness. As expected, the absorption coefficient is overestimated by a large factor for the 10 mm slab but is independent of slab thickness above 50 mm. No systematic dependence of the transport scattering coefficient on slab thickness was shown in these experiments. Clearly, it would be useful to have guidelines as to when the semi-infinite model can be applied and when a complete finite slab model (Patterson et al. 1989) must be used. Such guidelines would have to incorporate the absorption and reduced scattering coefficients of the slab material, the thickness of the slab, the separation of source and detector, and the time range over which the fit is performed.

The results for the spherical and cylindrical phantoms are summarized in Figures 3.10 and 3.11. For the spherical phantom $\mu_a = 0.0035$ mm^{-1} and $\mu_s' = 1.9$ mm^{-1} while, for the cylindrical phantom, the corresponding values were 0.0048 mm^{-1} and 1.9 mm^{-1}. Again, these values were limited by signal-to-noise considerations as larger source-detector separations were used in these geometries. The pattern established for the slab phantom is also observed here as reliable estimates of $\mu_a$tr and μ_s'tr are obtained for large objects but $\mu_a$tr is significantly overestimated for the smallest phantoms. It is interesting to note that, except for the smallest phantom, the derived coefficients show little systematic dependence on the angular separation of source and detector. Again, the purpose of future work in this area will be to establish criteria delimiting the range of μ_a, μ_s', object size,

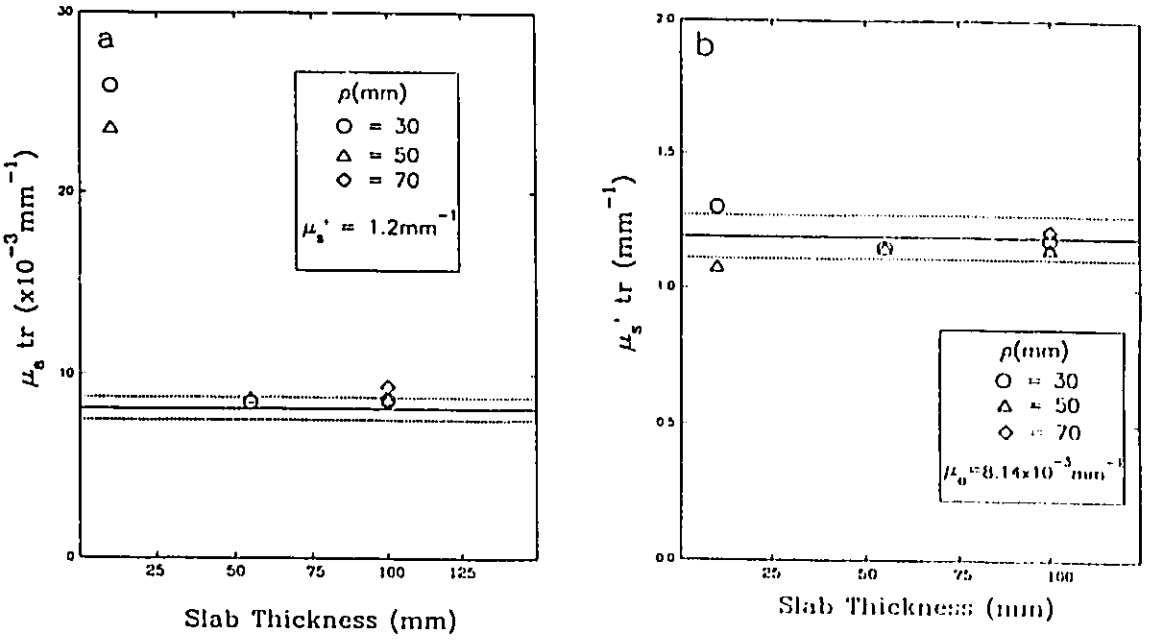

Figure 3.9 Summary of results in the slab geometry; (a) estimated absorption coefficient versus slab thickness and (b) estimated transport scattering coefficient vs. slab thickness. The solid lines correspond to the steady-state value, whose uncertainty is given by the dashed lines.

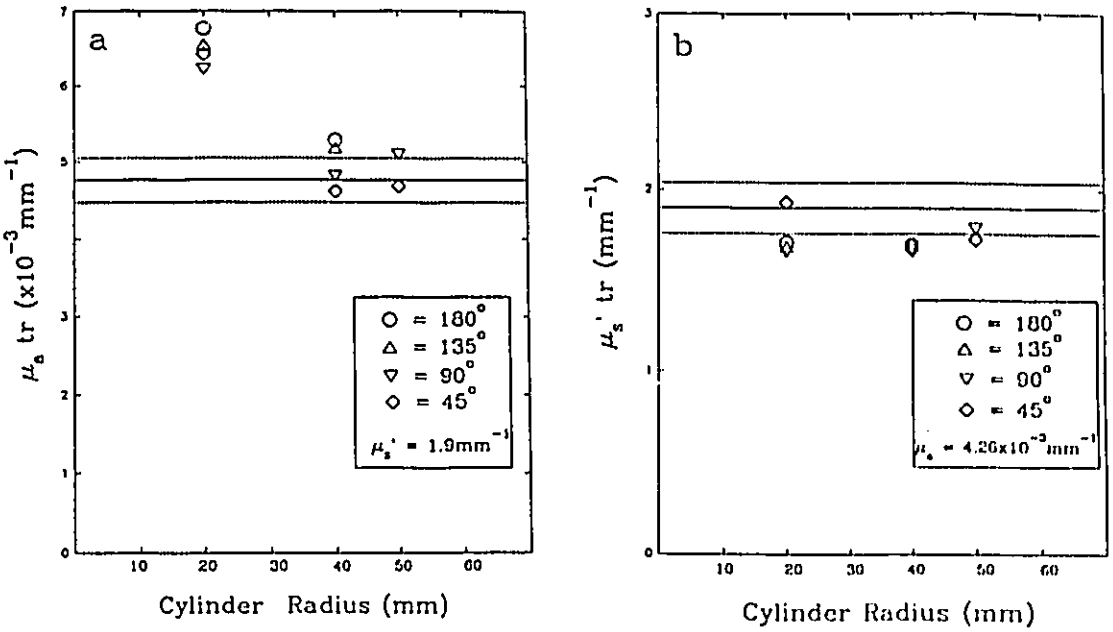

Figure 3.10 Summary of results in the cylindrical geometry; (a) estimated absorption coefficient versus cylinder radius and (b) estimated transport scattering coefficient versus cylinder radius. The steady-state value and its uncertainty are indicated by the solid and dashed lines respectively.

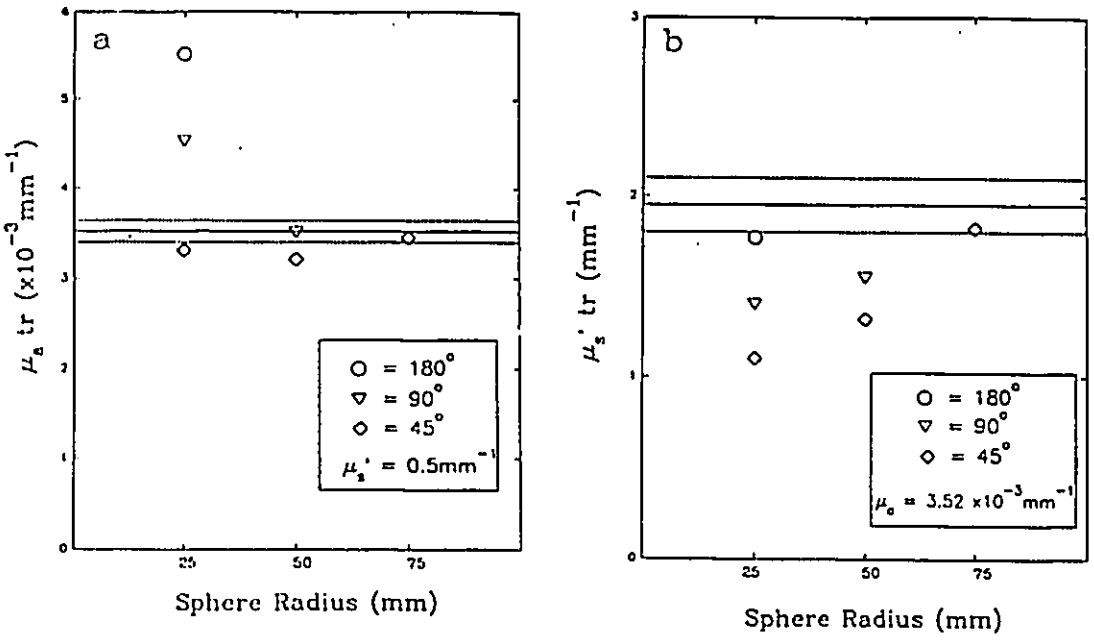

Figure 3.11 Summary of results in the spherical geometry; (a) estimated absorption coefficient versus sphere radius and (b) estimated transport scattering coefficient versus sphere radius. The steady-state value and its uncertainty are indicated by the solid and dashed lines respectively.

angular separation and time interval over which the simple model may be used with confidence.

3.5 Conclusions

We have demonstrated that a simple diffusion model of time-resolved diffuse reflection allows the deduction of the absorption and transport scattering coefficients of a semi-infinite homogeneous medium with an error of 10 % or less. The source of the overestimation of the absorption coefficient remains unidentified, but comparison with Monte Carlo simulations indicate that the model itself is not in error. The possibility of systematic errors in the steady-state measurements of optical properties cannot be ruled out. Experiments with polystyrene microspheres (for which the scattering properties can be precisely calculated) might help to identify the source of this error. In any case, an absolute error of 10 % is not prohibitively large for many biological experiments. Relative errors in, for example, comparing absorption coefficients before and after some physiological event would be much smaller. Measurements on different optical phantoms, prepared to have identical optical properties, agreed to within 5 %.

Any real biological measurement must however be performed on finite volumes. The experiments reported here showed that, for relatively large objects, the simple model can be used with excellent results. For smaller objects, however, loss of light at the boundaries leads to a large overestimation of the absorption coefficient. Since this can occur for objects with dimensions comparable to those encountered in measurements on

typical organs, especially in small animals, it is important to establish when the simple (semi-infinite) model can be used and when the exact geometry-dependent models must be applied. Compared with the predictions of the semi-infinite model, theoretical calculations (Moulton 1990) of the diffuse reflectance in finite cylinders, spheres and slabs yield pulses with earlier peaks and greater slopes. These changes are attributed to the fact that the absorbing boundaries have been accounted for in the exact models. Fitting of the experimental data to such models would likely produce better estimates of the absorption coefficient.

CHAPTER 4

TIME-RESOLVED STUDIES IN INHOMOGENEOUS PHANTOMS

4.1 Introduction

The extension of time-resolved measurements to inhomogeneous media for imaging purposes has been attempted only very recently. For example, the characteristics of time-dependent light propagation imaging in cylindrical phantoms containing highly absorbing rods have been investigated in a number of studies (Arridge et al. 1990, Arridge et al. 1991 and Sevick et al. 1991). In most cases, the effect of the absorbing object on the total integrated signal and the mean time-of-flight was examined.

Potential biomedical applications of time-dependent photon imaging include imaging of light absorbing hematomas, tumors and hypoxic tissue volumes. The principle is relatively straightforward. Since time-resolved remittance spectra, detected at different locations around a particular organ, are affected differently by the presence of the internal structure, it should be possible in principle to reconstruct the internal structure from these external measurements (Wilson and Jacques 1990). However, this requires as one step the development of models of photon migration in inhomogeneous media. Possible candidates include diffusion theory, Monte Carlo computer simulations and random walk models. Since no exact analytic solutions of the diffusion equation exist in generalized inhomogeneous media, one must resort to cumbersome numerical solutions. Many numerical techniques have been developed to solve partial differential equations, such as

the time-dependent diffusion equation. For example, numerical solutions have been attempted using complex techniques such as finite element methods (Arridge et al. 1990, Arridge et al. 1992 and Schweiger et al. 1992) to reconstruct tissue parameters based on measurements of either the total integrated signal or the mean time-of-flight. In biologically realistic situations, Monte Carlo simulations typically require tens of hours of cpu time (Barbour et al. 1990 and Arridge et al. 1991), even on the fastest computers available. Thus, in a clinical situation where time is of the essence, Monte Carlo simulations appear to be unacceptable. Random walk models (Bonner et al. 1987 and Sevick et al. 1991), on the other hand, are clinically appealing since they have the potential of being very fast.

The purpose of the work described in this chapter was to determine the effects of discrete absorbing and scattering objects on light propagation characteristics in an otherwise homogeneous medium. Light propagation in the inhomogeneous medium was modelled using a finite difference representation of the time-dependent diffusion equation. This model is similar to that of Haselgrove et al. (1992) and, under some conditions, is identical to the random walk approach of Bonner et al. (1987). Time-resolved experiments were conducted in brain-simulating phantoms containing objects of various sizes and absorbances. The validity of the model was ascertained by comparing the experimental pulse to that predicted by the model.

4.2 Model

By finite differencing, in the case where μ_a is position dependent, the time-dependent diffusion equation (equation (30)) becomes (Press et al. 1989)

$$N_{i,j,k}^{p+1} = \{1-\mu_{aijk}c\Delta t\}\cdot (N_{i,j,k}^{p} + K\cdot (N_{i-1,j,k}^{p} + N_{i+1,j,k}^{p} + N_{i,j-1,k}^{p} + N_{i,j+1,k}^{p} + N_{i,j,k-1}^{p} + N_{i,j,k+1}^{p} - 6N_{i,j,k}^{p})) \quad , \tag{31}$$

where

$$K = \frac{cD\Delta t}{\Delta L^2}. \tag{32}$$

Equation (31) represents the time evolution of photons on a three-dimensional lattice, each lattice point having six nearest neighbours. $N_{i,j,k}^{p}$ is the photon density at lattice point i,j,k at the p^{th} time step, and Δt and ΔL represent the time step and lattice spacing respectively. This differencing scheme is known as the Forward Time Center Space (FTCS) scheme and is only first-order accurate in time, and stable only for sufficently small time steps. Stable solutions of equation (31) exist for $K \leq 1/6$ - the so-called Courant-Friedrichs-Lewy (CFL) stability criterion (Press et al. 1989). ΔL can take on any value, however, once chosen, Δt is constrained by the CFL stability criterion. The upper limit on K arises from the fact that the maximum allowable timestep (Δt) cannot be greater than the diffusion time across a cell of width ΔL. If it is, K will exceed 1/6 and physically unrealistic (i.e. negative) solutions result. There are practical limits governing the minimum value of Δt since execution time increases as Δt gets smaller. In situations

where K = 1/6, equation (31) reduces to the random walk model of Bonner et al. (1987). The simulation is initiated by injecting a single photon into the lattice. At each lattice point the photon weight is reduced due to isotropic scattering and absorption. The "reduced" photons propagate through the lattice in a stepwise manner until they reach the scoring region.

4.3 Materials and Methods

The experimental setup is illustrated in Figure 4.1. A mode-locked frequency-doubled Nd:YAG laser (Coherent Antares 76-s), emitting a train of 532 nm pulses at 76 MHz, pumped a cavity-dumped (3.8 MHz) dye (Rhodamine 6G) laser. The resultant 584 nm 50 nJ pulses (FWHM = 2 ps) passed through a series of neutral density filters before entering the phantom. The remitted light was collected with a one metre long 3 mm diameter fiber bundle located at various positions around the phantom. The other end of the fiber was coupled to a photodetector. The stability of the laser was monitored by splitting a small portion of the beam (10 %) and steering it into an integrating power meter. The total beam energy was measured for the duration of the data acquisition and the remitted pulses were corrected accordingly.

The photon counting system consisted of a microchannel plate photomultiplier tube (MCP-PMT), a constant fraction timing discriminator (CFTD), a time-amplitude converter (TAC) and a multichannel analyzer (MCA). The MCP-PMT (Hamamatsu R2809U-11) was operated at 2900 V and the neutral density filters at the source adjusted for each

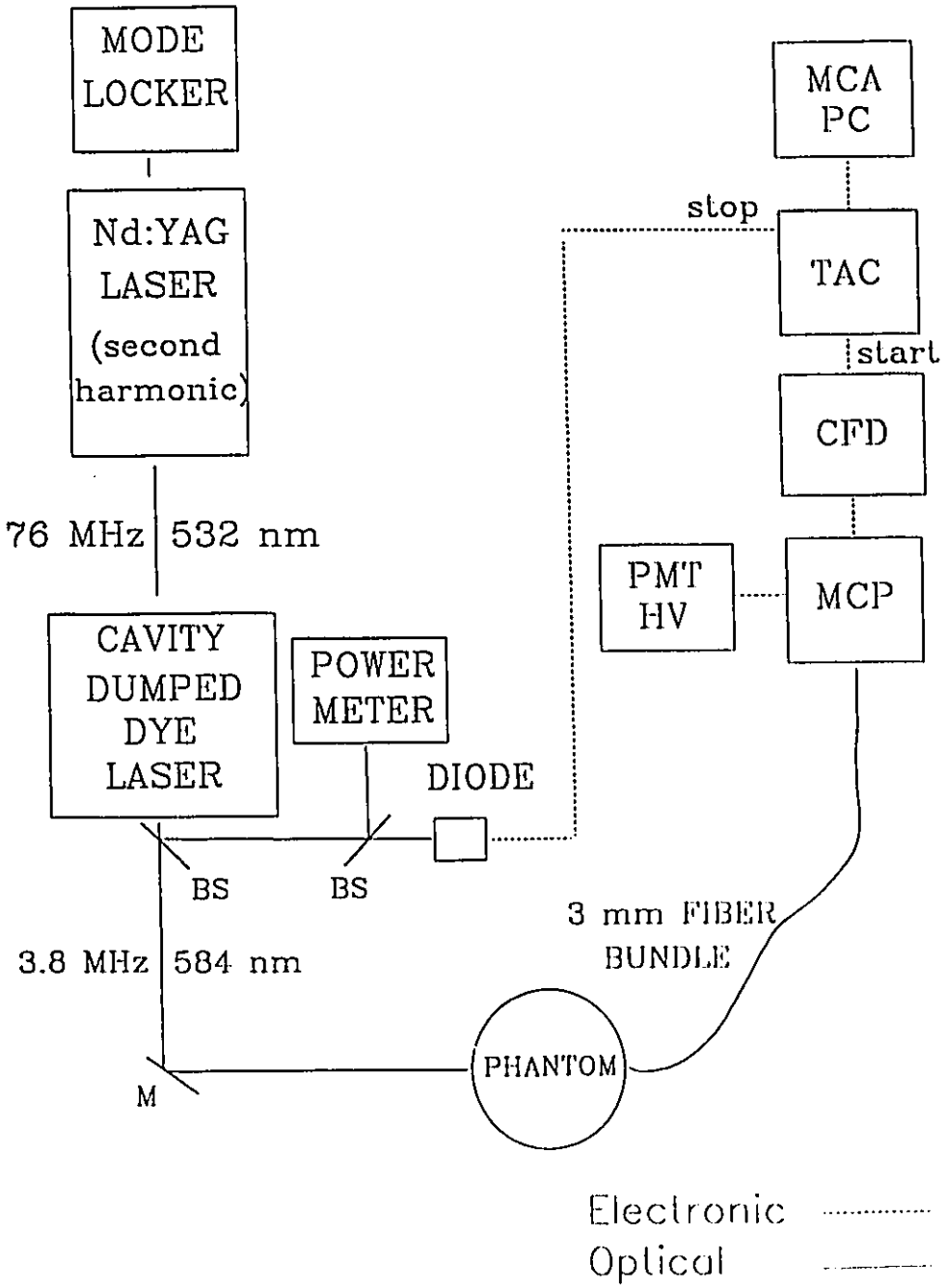

Figure 4.1 Experimental setup for the measurement of remitted pulses in an inhomogeneous medium. HV = high voltage, M = mirror and BS = beam splitter. In contrast to the setup in Chapter 3, the TAC was operated in inverted mode, i.e., the start and stop pulses were provided by the detector and diode respectively.

phantom configuration to give a count rate of approximately 1.0 kcps. In almost all cases, a data acquisition time of 3 minutes was used for each pulse measurement. The amplified detector output, fed to the CFTD, provided the start pulse to the TAC (Tennelec TC 864). The stop pulses were obtained optically by splitting the dye laser beam and steering part of it into a photodiode. The TAC output, which is proportional to the time interval between start and stop pulses, was then sent to the 4096 channel MCA. The time resolution of the system, as determined from the full width at half-maximum of the directly detected pulse (beam incident on the detector fiber), was approximately 70 ps.

In all cases, the scattering medium consisted of a dilute solution of 20 % Liposyn (Abbott Laboratories, Montreal, Canada) and deionized water. Measurements of the optical properties of Liposyn were accomplished using the steady-state techniques described in Section 2.1. The absorption of the medium was controlled independently by the addition of India ink with known optical properties.

The brain phantom consisted of a black, non-reflecting plastic cylinder (radius = 75 mm, height = 150 mm) with a circular lid (Figure 4.2a). In order to position the absorbing objects, a series of holes were drilled in the bottom of the lid. The holes, located on a straight line, were positioned in such a way that the objects could be placed against the source, at the center, or at the midpoint between the source and the center (Figure 4.2b). To allow light coupling into and out of the phantom, holes were drilled around the circumference (at the midpoint) at 30 degree increments in the source plane and sealed with thin transparent plastic windows.

Initially, the optical properties of the phantom material were chosen to mimic

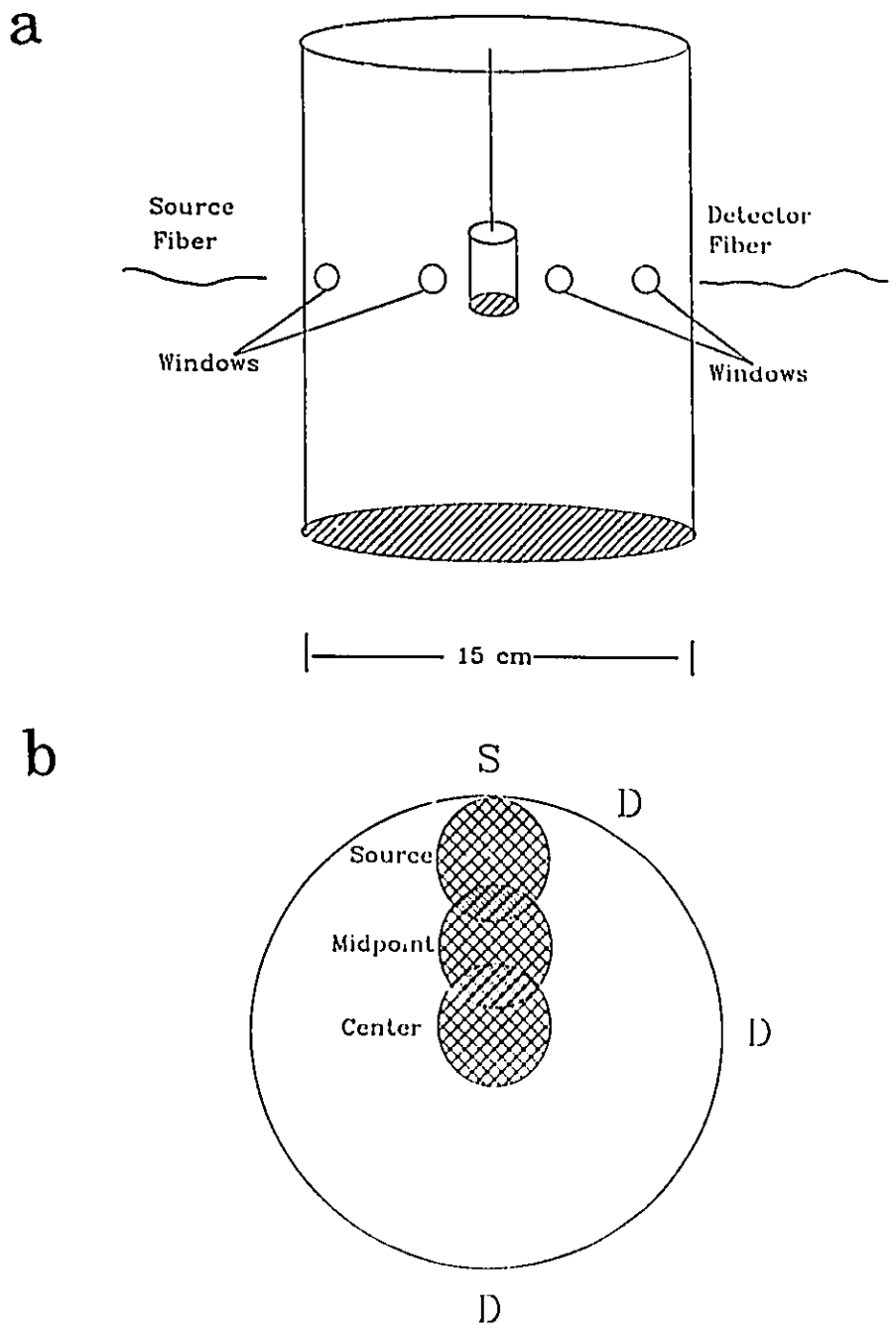

Figure 4.2 Cylindrical brain phantom. (a) Side view showing object in the center position. (b) Overhead view illustrating the three object positions considered.

closely those of the human brain at 584 nm, however, due to a lack of signal the optical coefficients of the material were reduced. At the experimental wavelength (584 nm), the absorption coefficient (0.005 mm^{-1}) was approximately 20 times lower than that of the human brain, while the transport scattering coefficient (0.5 mm^{-1}) was comparable (Splinter et al. 1989). In the near infrared, where clinical investigations are likely to be performed, the absorption used in these experiments is comparable to that of the human brain (Cheong et al. 1990).

The objects consisted of hollow transparent plastic cylinders (wall thickness = 0.1 mm) with lucite tops and bases (2 mm thick). A white plastic rod (diameter = 3.3 mm), fixed to the bottom of each cylinder, could be inserted into the lid holes to position the object. Filling and emptying of the object was accomplished through a screw hole in the top of the cylinder. A screw was used to prevent leakage of the object material into the surrounding medium. Each object was positioned such that its center was in the source-detector plane. Two different sized cylinders (radius = 20 mm, height = 40 mm and radius = 10 mm, height = 20 mm) were used. They will be referred to as the large and small objects throughout this chapter. In the first part of this investigation, each object was filled with Liposyn and India ink such that its scattering coefficient was identical to that of the surrounding medium while its absorption coefficient was 2, 10 or 100 times higher. In the case of the scattering object, the absorption coefficient was similar to the surrounding medium while the scattering coefficient was ten times greater.

Pulses were acquired as a function of source-detector position (30, 90 and 180°), object absorbance or scatter, position and size. The effect of the object walls on the pulse

shape was examined by filling the object with a sample solution taken from the surrounding medium. The shape of this pulse was then compared to that obtained in the absence of the object.

Analysis of the time-resolved data revealed a few anomalies in the total integrated intensity. This was attributed to the sensitive dependence of the signal on the detector fiber position. In order to investigate this, the total intensity was re-measured in a steady-state experiment using a 200 mW multimode (λ = 488 and 514 nm) continuous wave argon laser. The remitted light was detected using an MCP-PMT. Standard photon counting techniques were used to determine the total number of counts in the counting interval. A data acquisition time of 10 s was used for both the signal and the background. The signal was corrected for background. The optical properties of the phantom and objects were scaled such that they matched those of the time-resolved experiments at 584 nm. With the exception of the above changes, the measurements were identical to those described for the time-resolved experiments. The time-dependent data was normalized by equating the area under the curve (i.e., the total integrated intensity) to the steady-state data.

4.4 Results and Discussion

4.4.1 Homogeneous phantom

The validity of the numerical model was first examined through direct comparison with analytic solutions of the time-dependent diffusion equation in a homogeneous

medium with no internal structure (Figure 4.3). The diffusion equation was solved analytically for a 124 mm long cylinder of radius 75 mm (Moulton 1990). The absorption and transport scattering coefficients were 0.005 and 0.5 mm^{-1} respectively and the source and detector, located at the midpoint of the cylinder, were separated by 90°. Numerical calculations were performed under identical conditions and, as illustrated in Figure 4.3, there is excellent agreement between the numerical and analytical solutions. The finite difference model typically required about two hours of cpu time on a Microvax II (Digital Equipment Corporation, Maynard, MA). Obviously, the execution time (τ) will depend on the lattice density and on the size of the time step. Both parameters were chosen with the aim of minimizing the execution time. For example, for the coarsest lattice considered here ($\Delta L = (2)^{1/2}/\mu_s'$), the minimum execution time was achieved by choosing the largest possible time step given the restriction on the maximum value of K, i.e., $\Delta t = 1/(\mu_s' c)$.

4.4.2 Absorbing inhomogeneity

The results with the large absorbing object in the medium are summarized in Figures 4.4 - 4.6. In all cases, the experimental and model curves are represented by dots and solid lines respectively. The number associated with each curve represents the ratio of the absorption of the object to that of the surrounding medium. In each case, the effect of the object walls on the pulse shape was examined by filling the objects with a sample of the surrounding medium, i.e., the absorption ratio was 1. In all cases, the model curves denoted by 1 were normalized to the identical experimental case. The remaining model

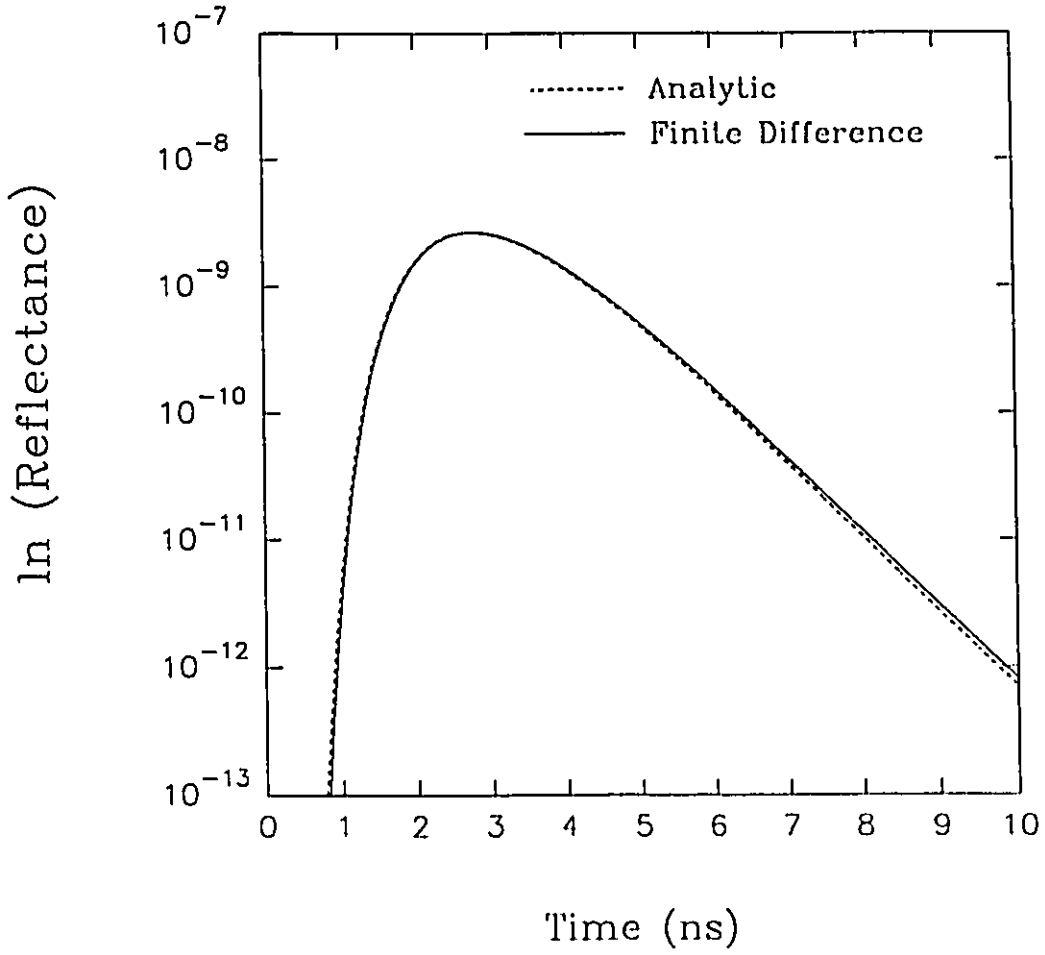

Figure 4.3 Comparison between an analytic solution and a finite difference representation of the time-dependent diffusion equation in a homogeneous cylindrical medium.

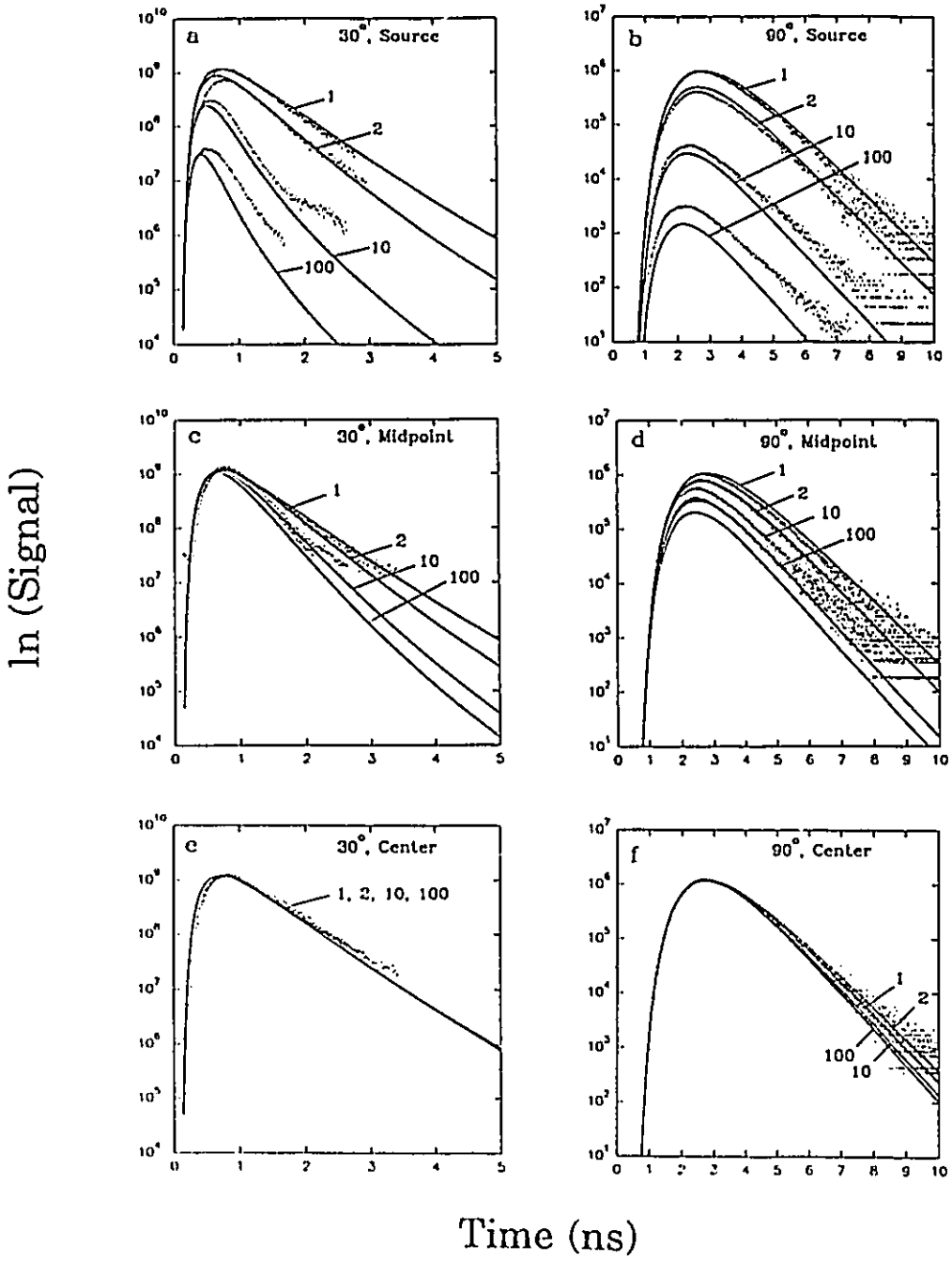

Figure 4.4 Pulse shapes as functions of source-detector separation (30 and 90°) and object position. The solid curves represent the model. The numbers associated with each curve represent $\mu_{a\ object}/\mu_{a\ surroundings}$.

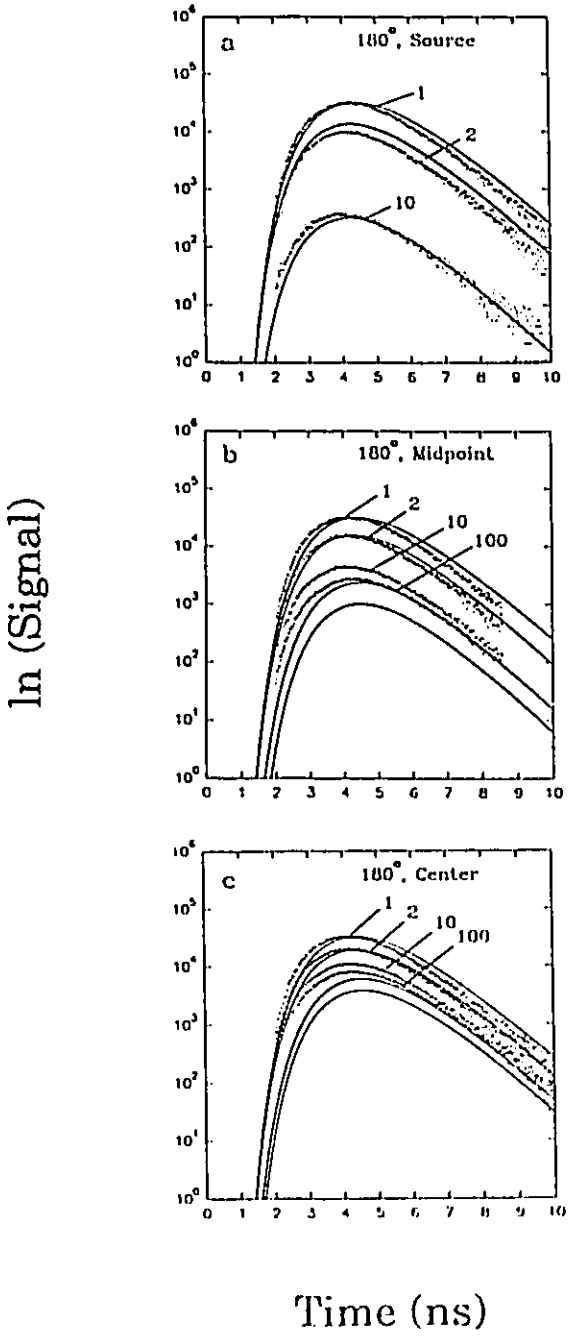

Figure 4.5 Pulse shapes as functions of source-detector separation (180°) and object position.

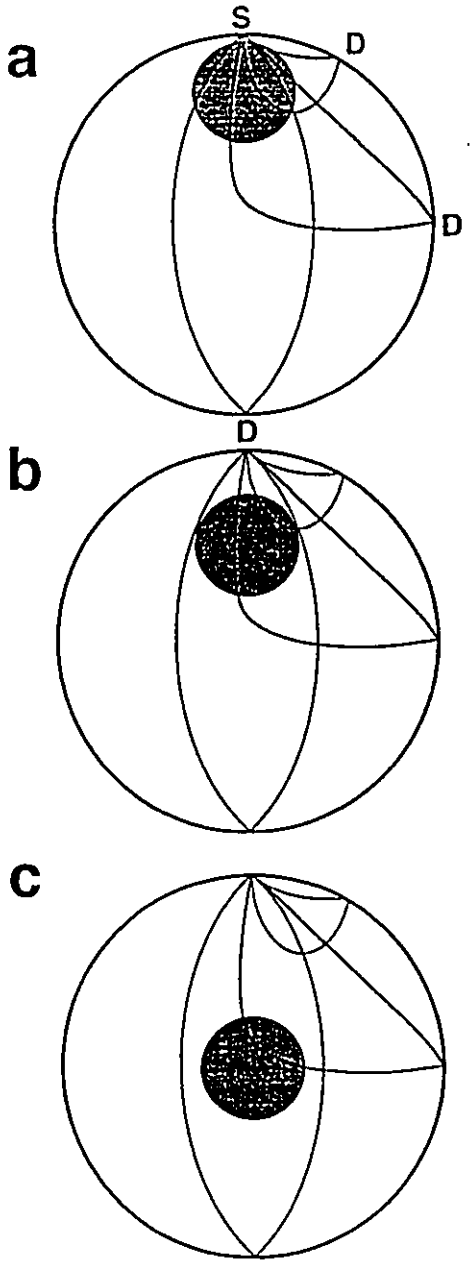

Figure 4.6 Typical photon sampling region versus source-detector separation; (a) source, (b) midpoint and (c) center.

curves were then multiplied by this factor. In all figures, the curve denoted by 1 includes the cylindrical plastic container. The presence of the plastic container affected the peak of the time-resolved curves by only a few percent, whereas the total integrated intensity was very sensitive to its presence. For example, the presence of the large object resulted in an intensity reduction of approximately 25 % compared with 15 % for the small object. This suggests that the plastic used here is slightly absorbing. This was confirmed in a series of integrating sphere experiments in which the total transmittance and reflectance were measured for a 0.1 mm thick plastic sheet. The plastic sheet was found to attenuate the incident beam by approximately 5 % (4 % due to specular reflection and 1 % due to absorption).

In general, there was good agreement between the model and experiment at an absorption ratio of 1 or 2, and poor agreement at a ratio of 100. At a ratio of 10, the agreement between model and experiment was somewhere between the two extremes. The large discrepancy in the high absorption case is probably due to the fact that the absorption in the object was too high for diffusion theory to be valid. The diffusion approximation is only valid in regions where the flux is linearly anisotropic. This is only true in regions far from sources and boundaries and where the scattering is much greater than the absorption. Certainly the last criterion is not satisfied here since $\mu_a \approx \mu_s'$ (0.5 mm^{-1}). At a ratio of 10 the diffusion approximation is starting to break down. From a practical point of view, the low absorption object might represent a tumor or the presence of an exogenous photosensitizer. For example, investigations of the optical properties (μ_a and μ_s') of brain tissue have shown that there is little difference between normal and

cancerous tissue (Cheong et al. 1990). Based on these results, it is highly unlikely that the absorption coefficient of cancerous tissue will be more than twice that of normal brain tissue.

The position dependence of the signal obtained with the large absorbing object is illustrated in Figures 4.4 and 4.5. Illustrations of the object position with respect to the optically sampled region are shown in Figure 4.6. At a given angle, as the object moves away from the source, differences in the experimental curves (total integrated intensity and time-to-peak) decrease. This is due to the fact that the object is moving out of the region sampled by the detected photons. For example, at 30°, when the object is at the source (Figures 4.4a and 4.6a), the four experimental curves can easily be distinguished. In this case, an increase in absorption results in a decrease in the total integrated intensity and a shift in the peak to earlier times. Moving the object to the center (Figures 4.4e and 4.6c) results in an inability to distinguish between the curves indicating that the object is effectively out of the sampled region. The predictions of the model are in qualitative agreement with the experimental data, i.e, differences in the model curves also decrease as the object moves away from the source.

At a given position of the object, as the observation angle is increased, differences in the experimental curves increase. This is due to the fact that the sampled region increases with angular separation. Thus, the probability that the photon will interact with the object increases. This effect is particularly evident when the object is located at the center and the angle is increased from 30 to 180° (Figures 4.4e,f and 4.5c). For example, as previously discussed, the four experimental curves in Figure 4.4e (30°, object at center)

cannot be resolved since the object is not in the sampled region. At 180° (Figure 4.5c), however, the object is always in the sampled region and differences in absorption properties of the objects show up as differences in the experimental curves. Again, the predictions of the model are in qualitative agreement with the experimental data.

Results for the small object are summarized in Figure 4.7. As expected, differences in the four experimental curves were smaller than those observed for the large object (Figure 4.4b). This can be attributed to a higher probability of photon absorption in the larger object. At an absorption ratio of 2, agreement between the model and experiment is comparable to that found for the large object. At ratios of 10 and 100, the trend is opposite to that of the large object, i.e., the model overestimates the experimental data in the case of the small object. The significance of this is not known since the diffusion approximation is probably not valid at such high absorptions.

The effect of the model grid size is illustrated in Figures 4.7 and 4.8. In general, a decrease in lattice point separation of $(2)^{1/2}$ has little effect on the model curve and does not lead to better agreement with the experimental data. There is a significant discrepancy between the coarse and fine model curves in the case of the small, highest absorbing object (Figure 4.7). Again, it should be emphasized that the significance of this discrepancy is not known since the diffusion approximation is not valid in this case. Due to computer memory constraints, a systematic study of the grid size effect for very dense grids in three dimensions was not possible. This effect was however investigated in two-dimensional lattices (Figure 4.9). The results shown in Figure 4.9 represent simulations performed in a homogeneous medium (solid lines) and with the large absorbing object

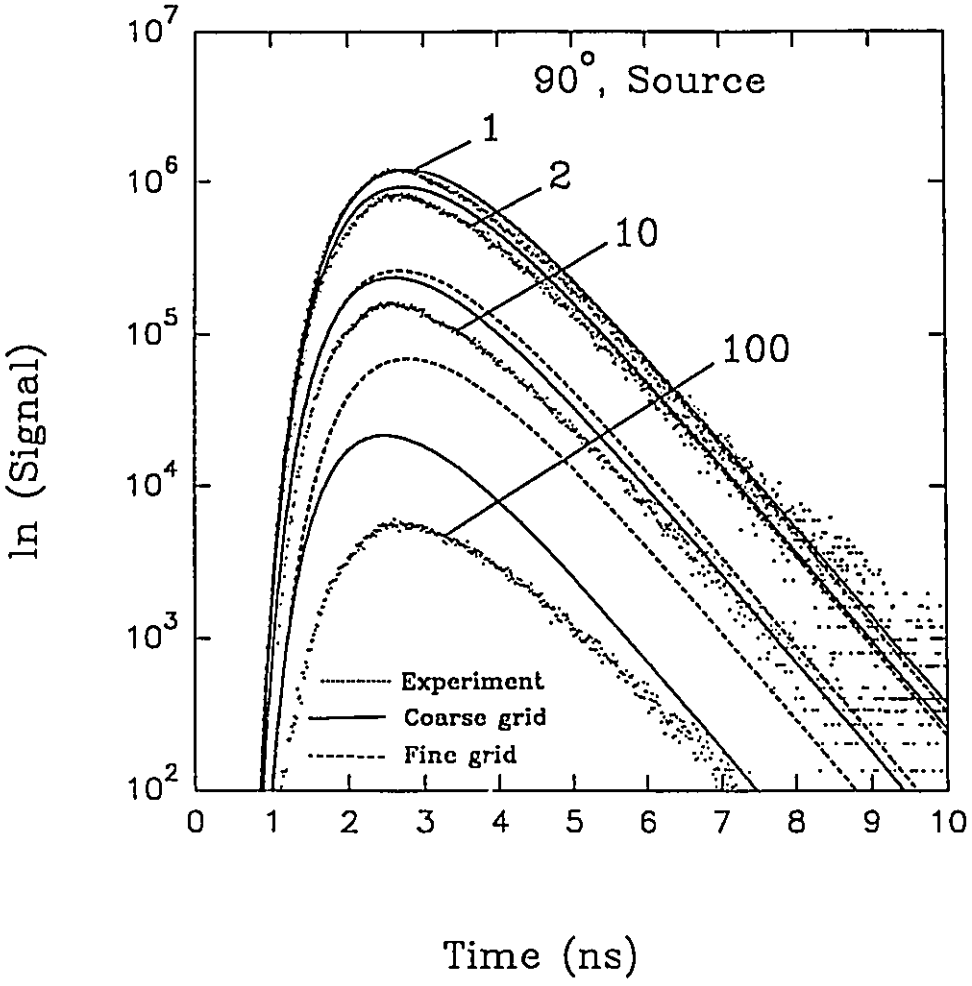

Figure 4.7 Pulse shape as a function of small object absorption and grid size.

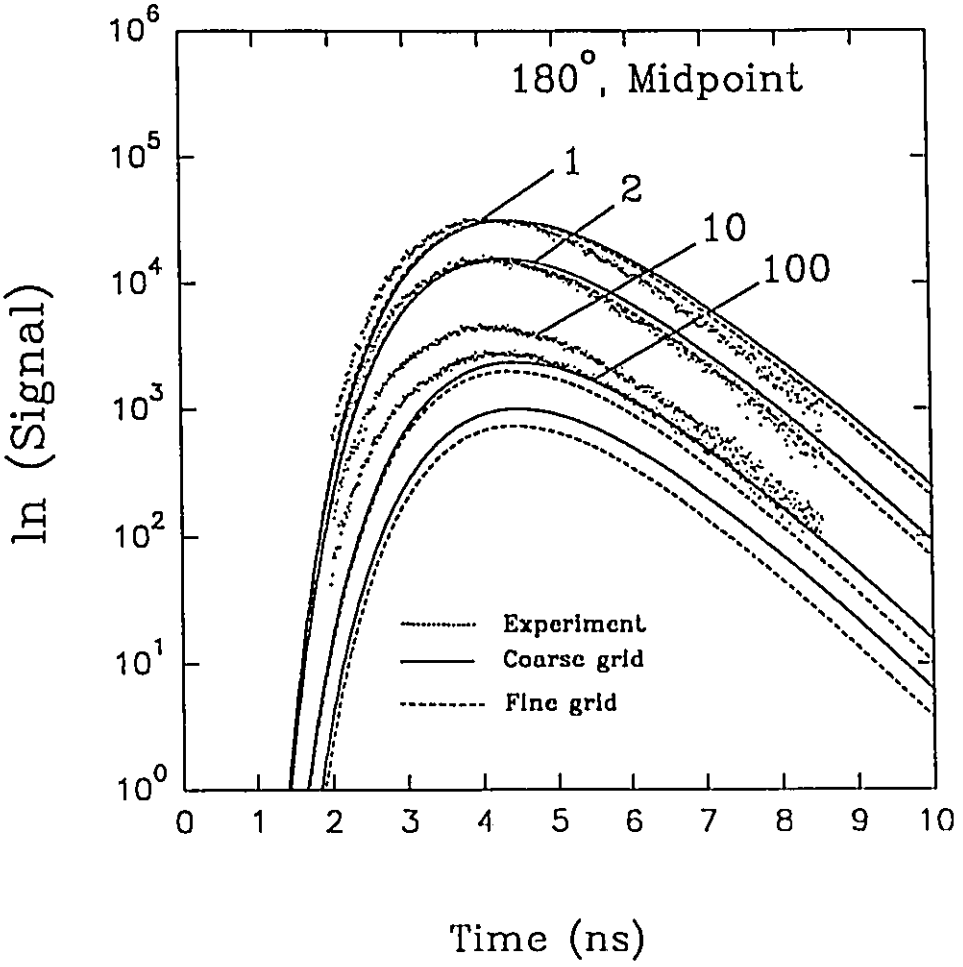

Figure 4.8 Pulse shape as a function of large object absorption and grid size.

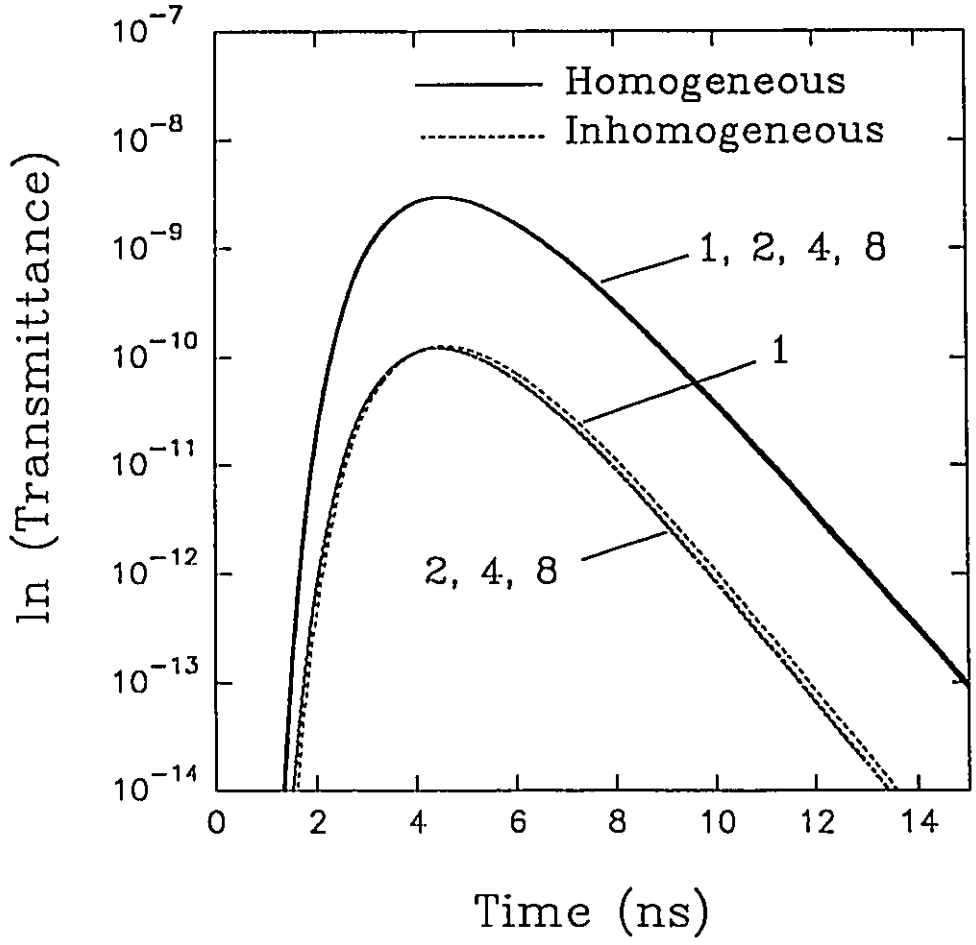

Figure 4.9 Investigation of grid size effect on a two-dimensional lattice. The inhomogeneous simulations were performed with a circular (r = 20 mm) absorbing object ($\mu_{a\ object}/\mu_{a\ surroundings}$ = 10) located at the midpoint of a large circle (r = 75 mm). The detector was positioned 180° from the source. The numbers denote the factor by which the coarsest grid ($\Delta L = (2)^{1/2}/\mu_s'$) was reduced.

(absorption ratio of 10) located at the midpoint (dashed lines). Four different grid sizes were considered and, in each case, the ratio of Δt to ΔL^2 was kept constant. The lattice separation of the coarsest grid was given by $(2)^{1/2}/\mu_s'$ (denoted by 1 in Figure 4.9). In subsequent simulations, the lattice separation was reduced by factors of 2, 4 and 8. In order to maintain the maximum allowable K (1/6), Δt was reduced by factors of 4, 16 and 64. It follows that the time advantage gained with this model is rapidly lost for fine lattices since $\tau \propto 1/\Delta L^2$. As shown in Figure 4.9, the model-derived curves rapidly converge as a function of lattice separation - a constant pulse shape being reached when the lattice separation is reduced by a factor of 2.

The two-dimensional results suggest that a finer grid than that used in the three-dimensional case will not result in better agreement between the model and experiment. For example, in Figure 4.8, a finer grid resulted in a decrease in the total integrated intensity and thus poorer agreement between the model and experimental data.

4.4.3 Scattering inhomogeneity

The results with the large scattering object in the medium are summarized in Figures 4.10 and 4.11. As before, the experimental and model curves are represented by dots and solid lines respectively, and the model data were normalized as discussed in section 4.4.2. The number associated with each curve represents the ratio of the scattering coefficient of the object to that of the surrounding medium.

The position and angular dependence of the changes in signal obtained with the

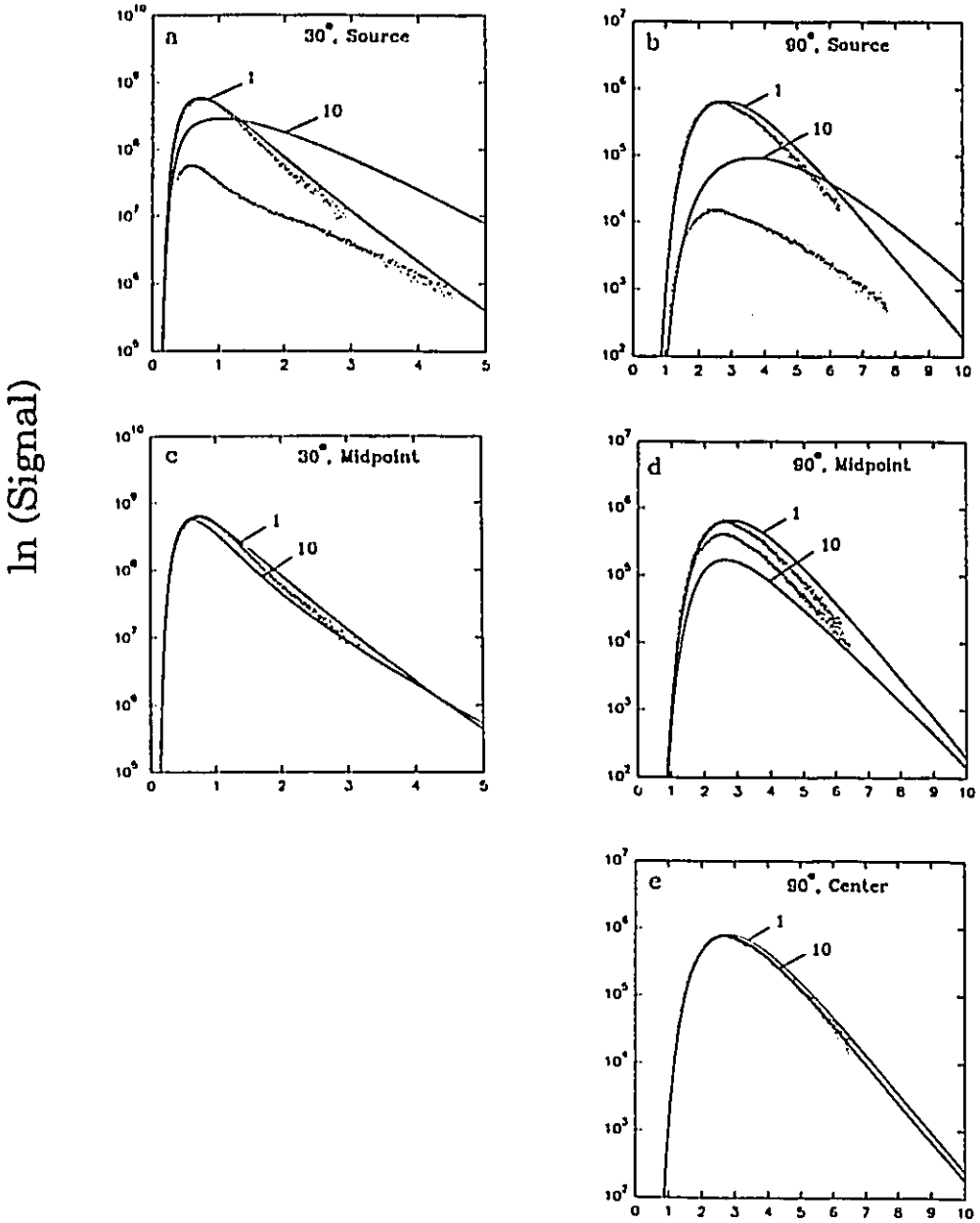

Figure 4.10 Pulse shapes as functions of source-detector separation (30 and 90°) and object position. The numbers associated with each curve represent $\mu'_{s\ object}/\mu'_{s\ surroundings}$.

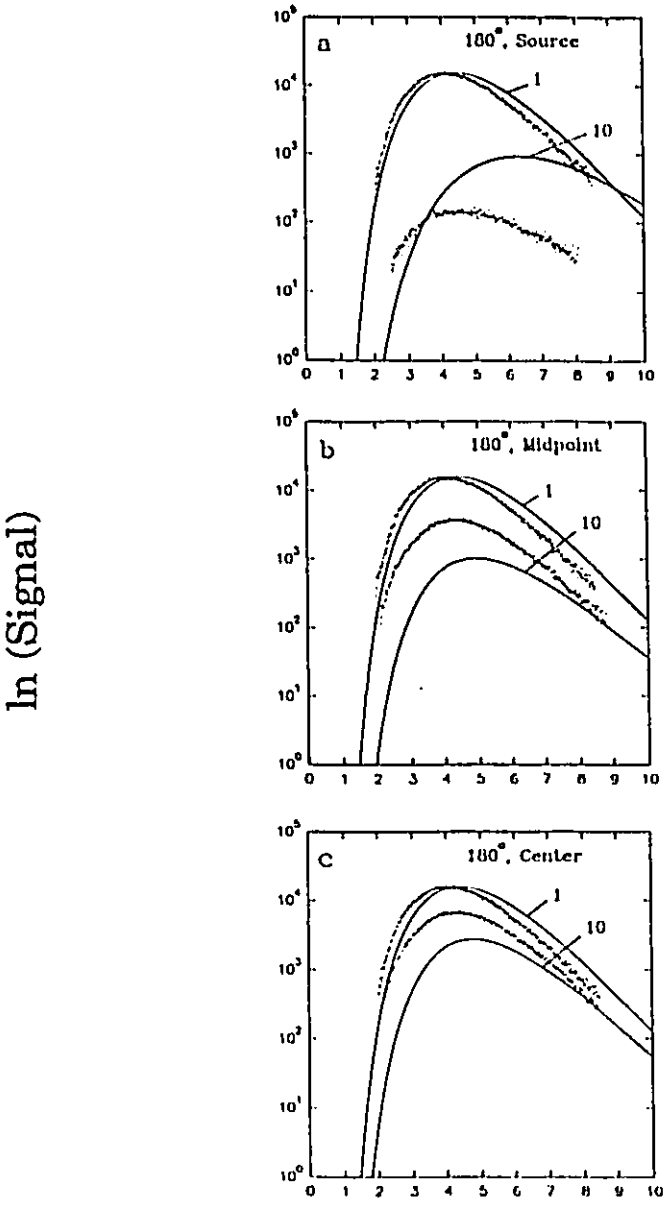

Figure 4.11 Pulse shapes as functions of source-detector separation (180°) and object position. The numbers associated with each curve represent $\mu'_{s\,object}/\mu'_{s\,surroundings}$.

large scattering object were similar to those observed for the absorbing object. At a given angle, as the object moves away from the source, differences in the experimental curves decrease. Again, this can be explained by the fact that the object is moving out of the region sampled by the photons. For example, at 30 and 90° the object is effectively out of the sampled region when it is located at the midpoint and center, respectively. At a given object position, as the observation angle is increased, differences in the experimental curves increase. This is due to the fact that the sampled region increases with angular separation.

In the case of the scattering inhomogeneity, discrepancies between the experimental data and the model calculations were much greater than those observed for the absorbing inhomogeneity. In cases where the scattering object was located in the sampled region, significant discrepancies in the total integrated intensity and the peak location were observed between the experimental and model curves. In general, the slope of the curves predicted by the model at long times was in qualitative agreement with that observed experimentally.

In order to determine whether the discrepancy between the model and experiment could be attributed to the grid size, two-dimensional simulations were performed at the three angles with the object at the source position. The results are summarized in Figure 4.12. The solid and dashed lines represent the homogeneous and inhomogeneous simulations respectively. The number associated with each curve represents the factor by which the original lattice separation has been reduced (see the discussion in section 4.4.2). The results in Figure 4.12 show that, as a function of lattice separation, the model-derived

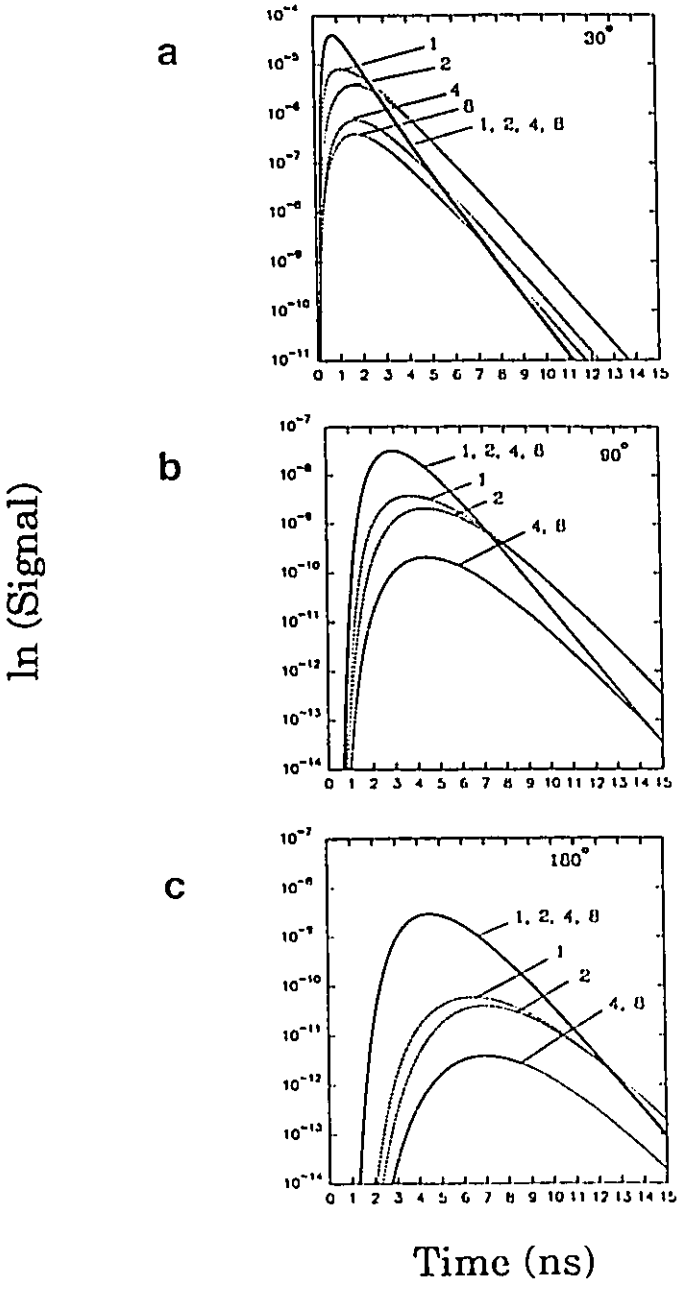

Figure 4.12 Investigation of grid size effect on a two-dimensional lattice. The inhomogeneous simulations were performed with a circular (r = 20 mm) scattering object ($\mu'_{s\ object}/\mu'_{s\ surroundings}$ = 10) located at the source of a large circle (r = 75 mm). Three detector positions were considered; (a) 30°, (b) 90° and (c) 180°.

curves do not converge as fast as was observed for the absorbing object. At 90 and 180°, the final pulse shape occurred only when the lattice separation was reduced by a factor of four. At 30°, convergence to a stable pulse was never achieved even for the finest lattice considered ($\Delta L = (2)^{1/2}/(8\mu_s')$). Extrapolation of these results to three-dimensions suggest that better agreement in the total integrated intensity between the model and experimental curves might be achieved by using a finer lattice. It is unlikely however that the discrepancy in the peak position can be resolved by resorting to finer grids. In the two-dimensional simulations, the peak actually shifts to later times as the lattice separation is reduced. To produce better agreement with the experiments would require a shift to earlier times.

In order to explore further the nature of the discrepancy between the experiments and model, two-dimensional Monte Carlo simulations were performed. Comparisons between these simulations and the predictions of the two-dimensional finite difference model are illustrated in Figures 4.13 and 4.14. In the homogeneous case, there is excellent agreement between the Monte Carlo simulations and the finite difference model at both 30 and 90°. In the inhomogeneous case, the results at 30° show a significant discrepancy in the peak location but better agreement in slope is observed at long times. It appears that the discrepancy between the Monte Carlo simulations and the predictions of the finite difference model is similar to that observed between the experimental results and the predictions of the three-dimensional model. This suggests that there was no systematic error in the experimental results and that the origin of the discrepancy is related to the model. According to the trend illustrated in Figure 4.12a, it is likely that better agreement

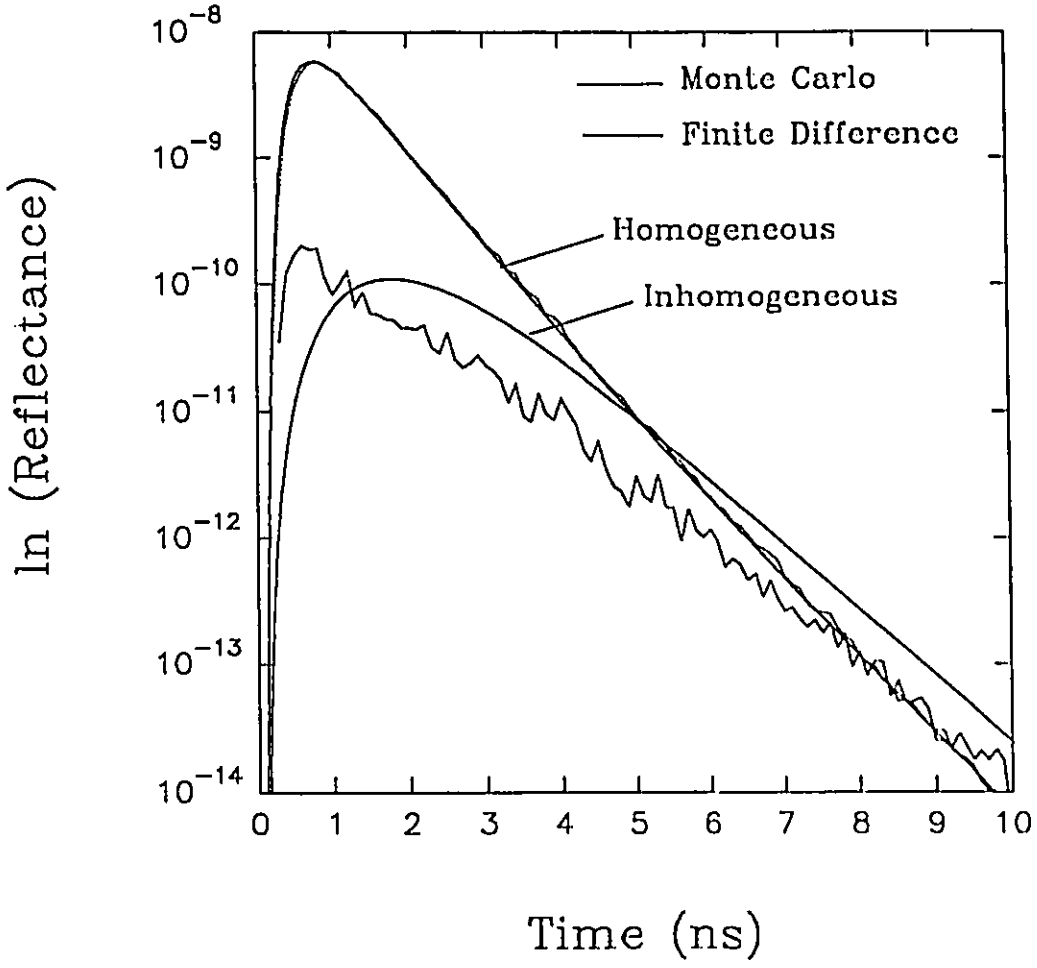

Figure 4.13 Comparison between Monte Carlo simulations and finite difference calculations in two dimensions. The angular separation between source and detector was 30°. The inhomogneity consisted of a circular (r = 20 mm) scattering object ($\mu'_{s\,object}/\mu'_{s\,surroundings} = 10$) located at the source of a large circle (r = 75 mm). 5 x 10^6 and 8 x 10^6 photons were used in the inhomogeneous and homogeneous Monte Carlo simulations respectively.

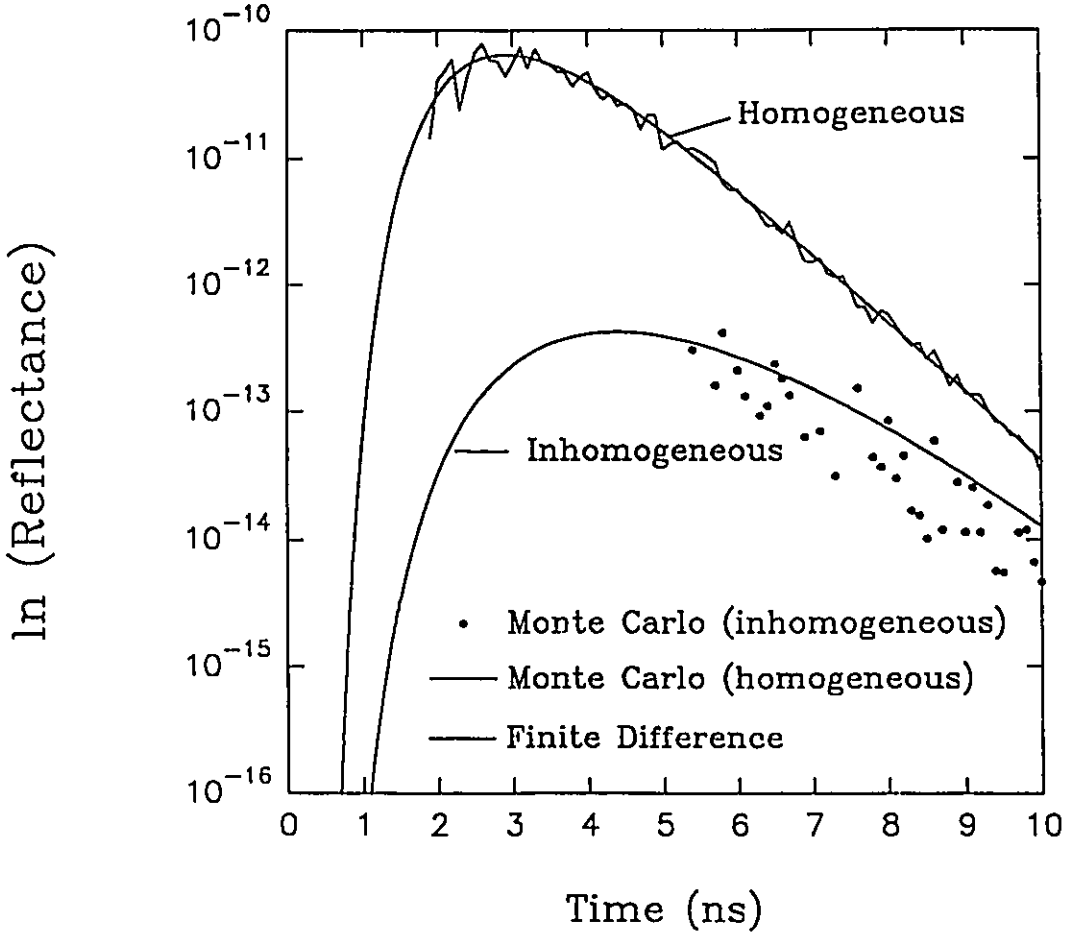

Figure 4.14 Comparison between Monte Carlo simulations and finite difference calculations in two dimensions. The angular separation between source and detector was 90°. The inhomogeneity consisted of a circular (r = 20 mm) scattering object ($\mu'_{s\,object}/\mu'_{s\,surroundings} = 10$) located at the source of a large circle (r = 75 mm). 5 x 10^6 and 8 x 10^6 photons were used in the inhomogeneous and homogeneous Monte Carlo simulations respectively.

could have been obtained at longer times by using a finer grid in the model calculations. Again, however, it is unlikely that the peak discrepancy can be resolved by resorting to finer grids. Due to computation time restrictions, calculations for grids finer than those presented here were not attempted. For example, calculations for the finest grids ($\Delta L = (2)^{1/2}/(8\mu_s')$) required approximately 23 cpu hours on a Sparc 2 workstation (Sun Microsystems, Inc. Mountain View, Ca). A further reduction of two in the lattice separation would result in a four-fold increase in the cpu time.

Due to poor Monte Carlo statistics, it is difficult to make any definitive statements regarding the inhomogeneous results at 90°, however, there appears to be fair agreement between the Monte Carlo simulation and the model calculation at long times. To improve significantly the statistics would require 10 to 100 times the number of photons considered in these simulations. Given the fact that on a Sparc 2 station it requires five cpu hours to simulate one million photons in the inhomogeneous case, such simulations would be impractical.

The failure of the model to describe adequately the experimental data was attributed to the coarseness of the three-dimensional lattice. Experimentally, the scattering mean free path in the object ($1/\mu_s' = 0.2$ mm) was approximately 14 times smaller than the lattice spacing. In the model, the lattice separation is held constant throughout the entire phantom and is determined by the transport scattering coefficient of the surrounding medium. The difference in optical properties between the object and the surroundings is incorporated in D in equation (32).

The fact that the discrepancy between the experiment and model is greatest when

the object is at the source position and the source and detector are separated by 30° supports the coarseness hypothesis. In this case, the photons spend more time in the object than in any of the other cases considered. As the model is incorrect in the object (the lattice spacing is too large), the predictions of the model will be the least accurate in this situation.

4.5 Conclusions

The shape of pulses remitted from a homogeneous medium containing discrete absorbing and scattering objects is very dependent on the source-detector separation and on the position of the object. In particular, the total integrated intensity appears to be very sensitive to these parameters. In the case of the absorbing object, computer simulations based on a finite difference representation of diffusion theory were found to be in good agreement with the experimental data as long as the object absorption was low enough that the assumptions of diffusion theory remained valid. Results of the simulations do not appear to be very sensitive to the lattice separation in this case and discrepancies between model and experiment could not be resolved by choosing a finer lattice.

Significant discrepancies between the experimental data and the model calculations were observed in the presence of the scattering object. These discrepancies were attributed to the coarseness of the lattice. Results of the two-dimensional finite difference calculations and Monte Carlo simulations suggest that, in terms of the total integrated intensity and the slope at long times, better agreement between the experimental data and

the predictions of the model would be possible if sufficient memory were available to run the three-dimensional model for finer grids. The discrepancy in peak position however, can probably not be resolved by resorting to finer grids. The origin of this discrepancy is not known.

In the experiments described here, the scattering coefficient of the object was ten times greater than that of the surrounding medium. This is not very realistic from a clinical point of view since the scattering ratio of malignant to normal tissue is probably more like 2:1 (Andersson-Engels et al. 1992). Thus, in order to simulate the presence of a tumour, a much smaller scattering coefficient than that used here could be chosen. Experimentally, the choice of a smaller object scattering coefficient would probably lessen the discrepancy observed here since the difference in the model and experimental mean free scattering path would be smaller.

A first step in the development of a model which may be useful in image reconstruction has been taken here. In the case of the absorbing object the model accurately predicts the shape of remitted pulses under conditions where the absorption of the object is up to twice that of the surroundings, i.e., conditions which may mimic the presence of a tumor or exogenous photosensitizer in vivo. The limited results presented for the scattering object show significant discrepancies between model and experiment. These discrepancies might be resolved by choosing a finer lattice and using a smaller, more biologically realistic object scattering coefficient in the experiments. The discrepancies observed here were not attributed to a breakdown of diffusion theory since reasonable agreement between experiment and theory were obtained for much lower ratios

of μ_s' to μ_a in the absorbing object.

From a clinical point of view the model is promising in that it has the potential of being very fast. Three-dimensional simulations performed on a Microvax II required only a few cpu hours, whereas comparable Monte Carlo simulations typically require tens of cpu hours for comparable precision. Time reductions of 20 to 30 fold can easily be accomplished using modern workstations. For example, simulations on a Sparc station 2 require tens of minutes of cpu time. With the workstations currently under development, simulations of the type considered here may be possible in tens of seconds of cpu time.

CHAPTER 5

CONCLUSIONS

Experimental studies of light propagation in turbid media were performed using time-resolved remittance spectroscopy. Studies were conducted in both homogeneous and inhomogeneous tissue-simulating media consisting of liquid mixtures of scattering and absorbing components. To determine the validity of the time-resolved results, the optical properties of the media were first examined using established techniques based on steady-state diffusion theory and Monte Carlo simulations. The optical properties of the scattering component (Intralipid or Liposyn) were found to be in good agreement with theoretical predictions and with the experimental results of others. The absorption and transport scattering coefficients of Liposyn are $(4.13 \pm 0.50) \times 10^{-4}$ and (1.59 ± 0.17) $mm^{-1}/\%$ respectively at 584 nm. The slight absorption at this wavelength was attributed to water. Intralipid and Liposyn can be used interchangeably since no significant difference in their optical properties was found.

The optical properties of the absorbing component (India ink), determined experimentally and from Monte Carlo computer simulations, were found to be in good agreement with theoretical predictions. Surprisingly, the results show that India ink has a significant scattering component, and thus cannot be regarded as a pure absorber. As expected, the optical properties are very sensitive to the ink particle size distribution.

Unfortunately, there appears to be significant inter-brand and inter-batch variations in particle size distributions, which explain the differences in optical properties obtained from different ink samples. This suggests that the optical properties of each new ink sample must be determined prior to use. Such a tedious procedure can be avoided by using non-particulate absorbers, such as molecular dyes, for which scattering is insignificant. The time-resolved results show that, in a semi-infinite homogeneous phantom, application of a simple time-resolved diffusion model provides estimates of the absorption and transport scattering coefficients accurate to better than 10 % over a limited albedo range. Comparable accuracy was also obtained for this simple model for finite slab, cylindrical and spherical volumes, as long as the objects were of sufficient size. For smaller volumes, the absorption coefficient was overestimated because of the significant loss of photons at the boundaries of the object.

More complete experimental studies are required in order to establish guidelines as to when the simple semi-infinite model can be used and when the exact geometry-dependent models must be applied. Such guidelines must incorporate the absorption and transport scattering coefficients of the object, the size of the object, the separation of source and detector, and the time range over which the fit is performed. Future work should be aimed at formulating expressions in the errors in $\mu_a tr$ and $\mu_s' tr$ as functions of these five parameters.

Time-resolved studies in inhomogeneous phantoms indicate that the shape of the remitted pulses are very sensitive to the size of the inhomogeneity, the source-detector separation, the position of the object and on the ratio of the optical properties of the

inhomogeneity to that of its surroundings. In the case of the absorbing object, the predictions of the model were found to be in good agreement with the experimental data as long as the object absorption was low enough such that the assumptions of diffusion theory remained valid. In the scattering object investigations, significant discrepancies were found between the experimental data and the model calculations. These discrepancies were attributed to coarse spatial sampling.

In future studies, smaller, more biologically realistic scattering coefficients should be chosen for the scattering inhomogeneity. The use of more complex models could also be attempted in future investigations. Numerous finite differencing schemes exist for discretizing partial differential equations such as the time-dependent diffusion equation. The FTCS scheme chosen here is one of the simplest and fastest. Other schemes may be more accurate, however, they are also likely to be more complex and slow and thus clinically inappropriate. There is usually a trade-off between accuracy and speed. Numerical solutions of the diffusion equation using a generalized Crank-Nicholson algorithm called the alternating-direction implicit (ADI) method (Press et al. 1989) has recently been attempted with some success to simulate photon propagation in inhomogeneous breast phantoms (Andersson-Engels et al. 1992). Such a scheme is second-order accurate in both time and space and, unlike the FTCS scheme, is stable for any size Δt. The use of such a model in combination with a smaller more appropriate choice of $\mu_{s\,object}'$ might yield better results than those obtained here.

The experimental studies described in Chapter 4 are limited in the sense that data were collected only under somewhat restrictive conditions, especially in the case of the

scattering object. In future studies, the emphasis should be on the collection of more complete data sets, i.e, collection of data at a greater number of angles and at object positions off the source-detector axis. With such a complete data set, it might be possible to determine uniquely the location and optical properties of an object embedded in a turbid medium.

The time-resolved experiments described in this thesis were performed using very expensive, complicated and bulky equipment requiring extensive technical support. The lasers had to be started many hours prior to experimentation in order to yield stable picosecond pulses. Even after the proper warm-up period, time drift and severe intensity fluctuations were quite common during a typical experiment. It is difficult to envision the use of such complicated and unreliable equipment in a clinical setting. A clinically useful system requires lasers which are user friendly, reliable and compact. These requirements are satisfied by picosecond pulsed diode lasers which do not require bulky cooling and power supplies and can usually operate from standard electrical outlets. Unlike dye lasers however, they are not tunable and their average power output is about 3 orders of magnitude lower. In spectroscopic applications where tunability may be a requirement, it is possible to use several diodes, each emitting at a different wavelength. Such studies would be somewhat limited, since presently available diodes do not emit at wavelengths below the red. The low power output is not a problem as long as the source-detector separation is relatively small and the medium probed is not too optically thick. In many of the experiments performed here, the incident light was intentionally attenuated with neutral density filters in order to ensure that early and late arriving photons were detected

with equal probability. For example, in tissue-simulating phantoms with a source-detector separation of 30 mm and average input powers of 50 mW, the incident light was attenuated by approximately five orders of magnitude. Such experiments could easily have been performed using pulsed diode lasers. The clinical usefulness of time-resolved techniques may be limited due to long acquisition times - typically a few minutes. Shorter acquisition times are possible if the experiments are performed in the frequency domain. The equipment required for such studies is relatively inexpensive and, due to the quick acquisition time (seconds), there is the possibility of performing dynamic studies in vivo. Furthermore, unlike time domain studies, the correction required to account for the instrument response function is relatively straightforward.

Both spectroscopy and imaging of turbid media have been performed in the frequency domain. It is highly unlikely however, that frequency domain imaging can be accomplished with the simple inexpensive equipment used in spectroscopic studies. Until the development of high power diodes, frequency domain imaging through thick optically dense biological tissue is probably only possible with the expensive and complicated high intensity picosecond laser systems used in the time domain.

Clearly, the choice between time and frequency domain depends on the experimental circumstances and endpoints. If possible, frequency domain studies should be performed due to low cost and rapid data acquisition. If, however, the signals are very weak, and quick data acquisition is not a requirement, the more sensitive time domain technique should be used.

In conclusion, the time-resolved experiments performed here are by no means

exhaustive. A first step has been taken towards the noninvasive determination of the optical properties of biological tissue using visible light. The results are encouraging and provide a basis for further scientific investigation of the role of light in spectroscopic and imaging applications in biology and medicine.

References

Anderson, R. R. et al., 1989, "Pulsed photothermal radiometry in turbid media: internal reflection of backscattered radiation strongly influences optical dosimetry". Appl. Opt. *28*, 2256-2262.

Andersson-Engels, S. et al., 1992, "Effects of optical constants on time-gated transillumination of tissue and tissue-like media". J. Photochem. Photobiol. B: Biol. *16*, 155-167.

Arridge, S. R. et al., 1990, "New Results for the Development of Infra-Red Absorption Imaging". In SPIE Proceedings Vol. 1245. Biomedical Image Processing.

Arridge, S. R. et al., 1991, "Reconstruction methods for infra-red absorption imaging". in SPIE Proceedings Vol. 1431. Time-Resolved Spectroscopy and Imaging of Tissues. Chance, B.(Ed.). SPIE,Bellingham, Washington, 122.

Arridge, S. R. et al., 1992, "Iterative Reconstruction of Near Infra-Red Absorption Images". In SPIE Proceedings Vol. 1767.

Barbour, R. L. et al., 1990, "Monte Carlo modeling of photon transport in tissue," Biophys. J. *57*, 381a-382a.

Bevington, P. R., 1969, Data Reduction and Error Analysis for the Physical Sciences. McGraw-Hill, New York.

Bohren, C. F. and Huffman, D. R., 1983, Absorption and Scattering of Light by Small Particles. Wiley, New York.

Bolin, F. P. et al., 1989, "Refractive index of some mammalian tissues using a fiber optic cladding method". Appl. Opt. *28*, 2297-2303.

Bonner, R. F. et al., 1987, "Model for photon migration in turbid biological media". J. Opt. Soc. Am. *A4*, 423-432.

Brazy, J. E. et al., 1985, "Noninvasive monitoring of cerebral oxygenation in preterm infants: Preliminary observations". Paediatrics *75*, 217-225.

Butler, W. L. and Norris, K. L., 1960, "The spectrophotometry of dense light-scattering material". Arch. Biochem. Biophys. *87*, 31-40, 1960.

Carter, L. L. and Cashwell, E.D., 1975, Particle Transport Simulation with the Monte Carlo Method. Technical Information Center, Office of Public Affairs, U. S. Energy

Research and Development Administration.

Chance, B. et al., 1951, "Rapid and Sensitive Spectrophotometry. I. The Accelerated and Stopped-Flow Methods for the Measurement of the Reaction Kinetics and Spectra of Unstable Compounds in the Visible Regiion of the Spectrum". Rev. Sci. Instrum. *22*, 619-627.

Chance, B. et al., 1988a, "Comparison of time-resolved and -unresolved measurements of deoxyhemoglobin in brain". Proc. Natl. Acad. Sci. USA *85*, 4971-4975.

Chance, B. et al., 1988b, "Time-resolved spectroscopy of hemoglobin and myoglobin in resting and ischemic muscle". Anal. Biochem. *174*, 698-707.

Cheong, W. F. et al., 1990, "A Review of the Optical Properties of Biological Tissues". IEEE J. Quant. Elect. *26*, 2166-2185.

Cope, M. and Delpy, D. T., 1988, "System for long term measurement of cerebral blood and tissue oxygenation on newborn infants by near infrared transillumination". Med. Biol. Eng. Comput. *26*, 289-294.

Corning Glass Works., 1991, personal communication.

Cross, F. W. et al., 1987, "Time-resolved photoacoustic studies of vascular tissue ablation at three laser wavelengths". Appl. Phys. Lett. *50*, 1019-1031.

Deirmendjian, D., 1960, "Atmospheric extinction of infra-red radiation". Q. J. R. Meteorol. Soc. *86*, 371-381.

Delpy, D. T. et al., 1988, "Estimation of optical pathlength through tissue from direct time of flight measurement". Phys. Med. Biol. *33*, 1433-1442.

Doiron, D. R. et al., 1983, "Light dosimetry in tissue: application to photoradiation therapy". In Porphyrin Photosensitization. Kessel, D. (Ed.). Plenum Press, New York, 63-76.

Driver, I. et al., 1989, "The optical properties of aqueous suspensions of Intralipid, a fat emulsion". Phys. Med. Biol. *34*, 1927-1930.

Duderstadt, J. J. and Hamilton, L. J., 1976, Nuclear Reactor Analysis. Wiley, New York.

Eason, G. et al., 1978, "The theory of the backscattering of light by blood". J. Phys. D *11*, 1463-1479.

Farrell, T. J. et al., 1992, "A diffusion theory model of spatially resolved, steady-state diffuse reflectance for the non-invasive determination of tissue optical properties in vivo". Med. Phys. *19*, 879-899.

Fenn, R. and Oser J., 1965, "Scattering properties of concentric soot-water spheres for visible and infrared light". Appl. Opt. *4*, 1504-1509.

Ferrari, M. et al., 1986a, "Cerebral blood volume and haemoglobin oxygen saturation monitoring in neonatal brain by near infrared spectroscopy". Adv. Exp. Med. Biol. *200*, 203-212.

Ferrari, M. et al., 1986b, "Effect of carotid artery compression test on regional cerebral blood volume, haemoglobin oxygen saturation and cytochrome -c- oxidase redox level in cerebrovascular patients". Adv. Exp. Med. Biol. *200*, 213-222.

Flock, S. T. et al., 1987, "Total attenuation coefficients and scattering phase functions of tissues and phantom materials at 633 nm". Med. Phys. *14*, 835-841.

Flock, S. T. et al., 1989a, "Monte Carlo Modeling of Light Propagation in Highly Scattering Tissues - I: Model Predictions and Comparison with Diffusion Theory" IEEE Trans. Biomed. Eng. *36*, 1162-1168.

Flock, S. T. et al., 1989b, "Monte Carlo Modeling of Light Propagation in Highly Scattering Tissues - II: Comparisons with Measurements in Phantoms". IEEE Trans. Biomed. Eng. *36*, 1169-1173.

Flock, S. T. et al. "The Optical Properties of Intralipid: A Phantom Medium for Light Propagation Studies". Lasers Surg. Med. *12*, 510-519.

Fox, E. et al., 1985, "Monitoring cerebral oxygen sufficiency in anaesthesia and surgery". Adv. Exp. Med. Biol. *191*, 849-854.

Furutsu, K. et al., 1980, "On the Diffusion Equation Derived from the Space-Time Transport Equation". J. Opt. Soc. Am. *70*, 360-366.

Groenhuis, R. A. J. et al., 1983a, "Scattering and absorption of turbid materials determined from reflection measurements. 1. Theory". Appl. Opt. 22, 2456-2462.

Groenhuis, R. A. J. et al., 1983b, "Scattering and absorption of turbid materials determined from reflection measurements. 2. Measuring method and calibration". Appl. Opt. 22, 2463-2467.

Hale, G. M. and Querry, M. R., 1973, "Optical Constants of Water in the 200-nm to 200-

μm Wavelength Region". Appl. Opt. *12*, 555-563.

Haselgrove, J. C. et al., 1992, "Investigation of the nonlinear aspects of imaging through a highly scattering medium," Med. Phys. *19*, 17-23 (1992).

Hazeki, D. et al., 1987, "Near infrared spectrophotometric monitoring of haemoglobin and cytochrome aa_3 in vivo". Adv. Exp. Med. Biol. *215*, 283-289.

Hemenger, R. P., 1977, "Optical properties of turbid media with specularly reflecting boundaries: applications to biological problems". Appl. Opt. *16*, 2007-2012.

Henyey, L. G. and Greenstein, J. L., 1941, "Diffuse radiation in the galaxy". Astrophys. J. *93*, 70-83.

Irvine, W. M., 1965, "Light scattering by spherical particles: radiation pressure, symmetry factor, and extinction cross section". J. Opt. Soc. Am. *55*, 16-21.

Ishimaru, A., 1978a, "Diffusion of a Pulse in Densely Distributed Scatterers". J. Opt. Soc. Am. *68*, 1045-1050.

Ishimaru, A., 1978b, Wave Propagation and Scattering in Random Media Vol. 1. Academic Press Inc., New York.

Jacques, S. L., 1989, "Time-resolved reflectance spectroscopy in turbid tissues". IEEE Trans. Biomed. Eng. *36*, 1155-1161.

Jacques, S. L. and Prahl, S. A., 1987, "Modelling Optical and Thermal Distributions in Tissue during Laser irradiation". Lasers Surg. Med. *6*, 494-503.

Jobsis, F. F., 1977, "Non-invasive, infra-red monitoring of cerebral and myocardial oxygen sufficiency and circulating parameters". Science *198*, 1264-1267.

Keilin, D. and Hartree, E. F., 1939, "Cytochrome and cytochrome oxidase". Proc. Roy. Soc. London *B 127*, 167-191.

Kerker, M., 1969, The Scattering of Light and other Electromagnetic Radiation. Academic Press Inc., New York.

Kortum, G., 1969, Reflectance Spectroscopy - Principles, Methods, Applications. Springer, New York.

Kubelka, P., 1948, "New contributions of the optics of intensely light-scattering materials". J. Opt. Soc. Am. *38*, 448-457.

Lakowicz, J. R. et al., 1989, "Frequency- and time-domain measurements of photon migration in tissues". Photochem. Photobiol. *49*, 825 (abstr.).

Long, F. H. et al., 1987, "Pulsed photothermal radiometry for depth profiling of layered media". Appl. Phys. Lett. *51*, 2076-2078.

Madsen, S. J. et al., 1991, "Time resolved diffuse reflectance and transmittance studies in tissue simulating phantoms". In SPIE Proceedings Vol. 1431. Time-resolved spectroscopy and imaging of tissues. Chance, B. and Katzir, A. (Eds.). Bellingham, Washington, 42-51.

Madsen, S. J. et al., 1992, "Experimental tests of a simple diffusion model for the estimation of scattering and absorption coefficients of turbid media from time-resolved reflectance measurements". Appl. Opt. *31*, 3509-3517.

Marijnissen, J. P. A. and Star, W. M., 1984, "Phantom measurements for light dosimetry using isotropic and small aperture detectors". In Porphyrin Localization and Treatment of Tumors. Doiron, D. R. and Gomer, C. J.(Eds.). Alan R.Liss Inc., New York, 133-148.

McKenzie, A. L., 1985, "How may external and interstitial illumination be compared in laser photodynamic therapy?". Phys. Med. Biol. *30*, 455-460.

Mie, G., 1908, "Beitrage zur Optik truber Medien, Speziell Kolloidaler Metallosungen" Ann. Physik *25*, 378-445.

Millikan, G. A., 1937, "Experiments on muscle haemoglobin". Proc. Roy. Soc. London *B123*, 218.

Moulton, J. D., 1990, Diffusion Theory Modelling of Picosecond Laser Pulse Propagation in Turbid Media, M. Eng. Thesis, McMaster University, Hamilton, Canada.

Moes, C. J. M. et al., 1989, "Measurements and calculations of the energy fluence rate in a scattering and absorbing phantom at 633 nm". Appl. Opt. *28*, 2292-2296.

Mudgett, P. S. and Richards, L. W., 1972, "Multiple scattering calculations for technology II". J. Coll. Interface Sci. *39*, 551-567.

Nossal, R. et al., 1988, "Photon migration in layered media". Appl. Opt. *27*, 3382-3391.

Nossal, R. et al., 1989, "Influence of pathlength on remote sensing of properties of biological tissue". Appl. Opt. *28*, 2238-2244.

Patterson, M. S. et al., 1989a, "Time resolved reflectance and transmittance for the noninvasive measurement of tissue optical properties". Appl. Opt. *18*, 3484-3488.

Patterson, M. S. et al., 1989b, "Quantitative reflectance spectrophotometry for the noninvasive measurement of photosensitizer concentration in tissue during photodynamic therapy". In SPIE Proceedings Vol. 1065. Photodynamic Therapy: Mechanisms. Dougherty, T. J. (Ed.). SPIE, Bellingham, Washington, 115-122.

Patterson, M. S. et al., 1990, "Applications of time resolved light scattering measurements to photodynamic therapy dosimetry". In SPIE Proceedings Vol. 1203. Photodynamic Therapy: Mechanisms II. Dougherty, T. J. (Ed.). SPIE, Bellingham, Washington, 62-75.

Patterson, M. S. et al., 1991a, "The Propagation of Optical Radiation in Tissue. 1. Models of Radiation Transport and their Application". Lasers Med. Sci. *6*, 155-168.

Patterson, M. S. et al., 1991b, "The Propagation of Optical Radiation in Tissue. 2. Optical Properties of Tissues and Resulting Fluence Distributions". Lasers Med. Sci. *6*, 379-390.

Patterson, M. S. et al., 1991c, "Frequency-domain reflectance for the determination of the scattering and absorption properties of tissue". Appl. Opt. *30*, 4474-4476.

Penndorf, R., 1962, "Scattering and extinction coefficients for small absorbing and non-absorbing aerosols". J. Opt. Soc. Am. *52*, 896-905.

Peters, V. G. et al., 1990, "Optical properties of normal and diseased human breast tissues in the visible and near infrared". Phys. Med. Biol. *35*, 1317-1334.

Piantadosi, C. C. et al., 1986, "Near infrared spectrophotometric monitoring of oxygen distribution to intact brain and skeletal muscle tissue". Critical Care Med. *14*, 698-706.

Pogue, B. W., 1992, personal communication.

Prahl, S. A. et al., 1992, "Determination of optical properties of turbid media using pulsed photothermal radiometry". Phys. Med. Biol. *37*, 1203-1217.

Press, W. H. et al., 1992, Numerical Recipes in Fortran: the art of scientific computing. Cambridge University Press, New York.

Profio, A. E. and Sarnaik, J.,1984, "Fluorescence of HPD for tumor detection and and dosimetry in photoradiation therapy". In Porphyrin Photosensitization and Treatment

of Tumors. Doiron, D. R. and Gomer, C. J. (Eds.). Alan R. Liss Inc., New York, 163-175.

Rayleigh, L., 1871, "On the light from the sky, its polarization and colour". Phil. Mag. *41*, 107-120.

Reichman, J., 1973, "Determination of absorption and scattering coefficients for nonhomogeneous media. 1. Theory" Appl. Opt. *12*, 1811-1815.

Reynolds, L. et al., 1976, "Diffuse reflectance from a from a finite blood medium: applications to the modeling of fiber optic catheters". Appl. Opt. *15*, 2059-2067.

Schmitt, J. M. et al., 1990, "Multilayer model of photon diffusion in skin". J. Opt. Soc. Am. *A7*, 2141-2153.

Schweiger, M. et al., 1992, "Application of the Finite Element Method for the Forward Model in Infra-Red Absorption Imaging". In SPIE Proceedings Vol. 1767.

Senftleben, H. and Benedict, E., 1918, "Optical constants and radiation laws of carbon". Ann. Physik *54*, 65-78.

Sevick, E.M. et al., 1991, "Time-dependent photon migration imaging". In SPIE Proceedings Vol. 1599. Recent Advances in the Uses of Light in Physics, Chemistry, Engineering and Medicine. Akins, D. L. and Alfano, R. R. (Eds.). SPIE, Bellingham, Washington, 273-283.

Shimizu, K. et al., 1979, "Backscattering of a Picosecond Pulse from Densely Distributed Scatterers". Appl. Opt. *18*, 3484-3488.

Singer, J. et al., 1990, "Image reconstruction of the interior of bodies that diffuse radiation". Science *248*, 990-993.

Splinter, R. et al., 1989, "In vitro optical properties of human and canine brain and urinary bladder tissues at 633 nm," Lasers Surg. Med. *9*, 37-41.

Star, W. M. et al., 1987, "Light dosimetry status and prospects". J. Photochem. Photobiol. *B1*, 149.

Star, W. M. et al., 1988, "Light dosimetry in optical phantoms and in tissues I. Multiple flux and transport theory". Phys. Med. Biol. *33*, 437-454.

Steinke, J. M. and Shephard, A. P., 1986, "Diffuse reflectance of whole blood: Model for a diverging light beam". IEEE Trans. Biomed. Eng. *34*, 826-833.

Svaasand, L. O. and Ellingson, R., 1983, "Optical properties of human brain". Photochem. Photobiol. *38*, 293-299.

Takatani, S. and Graham, M. D., 1979, "Theoretical analysis of diffuse reflectance from a two-layer tissue model". IEEE Trans. Biomed. Eng. *26*, 656-664.

van de Hulst, H. C., 1980, Light Scattering by Small Particles. Dover, New York.

van Staveren et al., 1991, "Light scattering in Intralipid - 10% in the wavelength range of 400-1100 nm". Appl. Opt. *30*, 4507-4514.

Weinman, J. A. and Shipley, S. T., 1972, "Effects of Multiple Scattering on Laser Pulses Transmitted Through Clouds". J. Geophys. Res. *77*, 7123-7128.

Weiss, G. H. et al., 1989, "Statistics of penetration depth of photons re-emitted from irradiated tissue". J. Mod. Opt. *36*, 349-359.

Wilson, B. C., 1991, "Modelling and Measurements of Light Propagation in Tissue for Diagnostic and Therapeutic Applications". In Laser Systems for Photobiology and Photomedicine. Chester, A. N. et al. (Eds.). Plenum Press, New York, 13-27.

Wilson, B. C. and Adam, G., 1983, "A Monte Carlo model for the absorption and flux distributions of light in tissue". Med. Phys. *10*, 824-830.

Wilson, B. C. and Jacques, S. L., 1990, "Optical Reflectance and Transmittance of Tissues: Principles and Applications". IEEE J. Quant. Elect. *26*, 2186-2199.

Wilson, B. C. and Patterson, M. S.,1986, "The Physics of Photodynamic Therapy". Phys. Med. Biol. *31*, 327-360.

Wilson, B. C. et al., 1985, "In vivo and post mortem measurements of the attenuation spectra of light in mammalian tissues". Photochem. and Photobiol. *42*, 153- .

Wilson, B. C. et al., 1986, "Effect of photosensitizer concentration in tissue on the penetration depth of photoactivating light". Lasers Med. Sci. *1*, 235-244.

Wilson, B. C. et al., 1987, "Indirect versus direct techniques for the measurement of the optical properties of tissues". Photochem. Photobiol. *46*, 601-608.

Wilson, B. C. et al., 1989, "The potential of time-resolved reflectance measurements for the noninvasive determination of tissue optical properties". In SPIE Proceedings Vol. 1064. Thermal and Optical Interactions with Biologic and Related Composite Materials. Berry, M. J. and Harpole, G. M. (Eds.). SPIE, Bellingham, Washington,

97-106.

Wilson, B. C. et al., 1990, "An optical fiber-based diffuse reflectance spectrometer for non-invasive investigation of photodynamic sensitizers in vivo". In SPIE Institute Series Vol. IS6. Future Directions and Applications in Photodynamic Therapy. SPIE, Bellingham, Washington, 219-232.

Wilson, B. C. et al., 1992, "Time-Dependent Optical Spectroscopy and Imaging for Biomedical Applications". Proc. IEEE *80*, 918-930.

Yoo, K. M. and Alfano, R. R., 1990, "Determination of the scattering and absorption lengths from the temporal profile of a backscattered pulse". Opt. Lett. *15*, 276-278.

Yoo, K. M. and Alfano, R. R., 1990, "Coherent backscattering of light from biological tissues". Appl. Opt. *29*, 3237-3239.

Yoo, K. M. et al., 1990, "When does the diffusion approximation fail to describe photon transport in random media?". Phys. Rev. Lett. *64*, 2647-2650.